Carrier Distributions in Long Wavelength Quantum Dot Laser Diodes

Adrian A. George

PhD Thesis

School of Physics and Astronomy
Cardiff University

2007

UMI Number: U585570

All rights reserved

INFORMATION TO ALL USERS
The quality of this reproduction is dependent upon the quality of the copy submitted.

In the unlikely event that the author did not send a complete manuscript
and there are missing pages, these will be noted. Also, if material had to be removed,
a note will indicate the deletion.

UMI U585570
Published by ProQuest LLC 2013. Copyright in the Dissertation held by the Author.
Microform Edition © ProQuest LLC.
All rights reserved. This work is protected against
unauthorized copying under Title 17, United States Code.

ProQuest LLC
789 East Eisenhower Parkway
P.O. Box 1346
Ann Arbor, MI 48106-1346

Abstract

In this thesis I have produced results to show how carriers populate electronic states of InAs quantum dot (QD) laser diodes which operate near 1.3μm, especially those which incorporate tunnel injection. I used the segmented contact method to produce modal absorption, modal gain, spontaneous emission and population inversion spectra as a function of photon energy.

The spontaneous emission spectra for a high performance QD structure showed an increased population of the higher energy QD states than the tunnel injection structure. Analysis of the carrier distribution within the high performance QD structure revealed that the population of the QD states can be described by Fermi-Dirac statistics (thermally distributed) at 300K. As the temperature is lowered the electron distribution becomes clearly non-thermal, with clear regions of high inversion seen in the lower energy QD states. The higher inversion can be attributed to a reduced population of wetting layer states and as the temperature is lowered it becomes less likely for carriers to excite out of the dot states and thermally redistribute throughout the ensemble.

The tunnelling injection structure was shown to exhibit unique features in its carrier distribution as compared to the high performance structure. At 300K the carrier distribution function is populated to thermal levels over energy ranges corresponding to a subset of the QD ground and first excited states. Between these energy ranges there is a region of under populated states shown by a region of low inversion. This suggests dots of a particular size within the ensemble are preferentially populated by the resonant tunnelling process. This results in a reduced spectral broadening of the emission from the QD ensemble. At higher temperature the selective population can still be observed, however it is less pronounced, presumably due to more efficient thermal distribution of electrons at higher temperature.

Acknowledgements

I would like to thank my PhD supervisors Prof. P. Blood and Dr P. Smowton for their advice and guidance throughout the variety of challenges I have faced during my studies. I would like to thank the members of the Photons and Matter Optoelectronics group for our many insightful discussions.

My experimental research would not have been possible without the continuous support of the Physics and Astronomy technical staff particularly; Mr Steven Baker, Mr R. Tucker, Mr H. Lang, Mr I. Robinson, Mr J. Trivett and Mr G. Summers. Thanks to Dr J. Thomson and Mrs K. Barnett for the processing of the various structures I have tested during my time at Cardiff.

The equipment used for these measurements was mainly constructed by Dr D. Palmer and without his improvements in the signal to noise ratio of this setup, results of this quality would not have been possible. The quantum dot laser diode structures detailed in this thesis were grown at the by Prof. P. Bhattacharya and Dr Z. Mi at the University of Michigan and Dr. H Liu at the EPSRC Central Facility for III-V Semiconductors in Sheffield.

Finally I would like to thank my partner Miss D. Waitt and my family for their endless support throughout my studies.

CONTENTS

1. INTRODUCTION 8

1.1 AIMS AND MOTIVATION 9

1.2 THESIS STRUCTURE 11

2. BACKGROUND THEORY 12

2.1 BRIEF HISTORY OF THE QUANTUM DOT LASER 13

2.2 QUANTUM DOT FORMATION 14

2.21 Stranski-Kranstanow Growth of QDs 14

2.22 Molecular Beam Epitaxy 14

2.23 Broadening in Self-Assembled QD lasers 15

2.3 OPTICAL ABSORPTION AND RADIATIVE RECOMBINATION 19

2.31 Optical Transition in Semiconductor Lasers 19

2.32 Transition Rate in a Two level System 20

2.33 Fermi-Dirac Statistics and Population Inversion 21

2.34 Relationship Between the Einstein Coefficients 22

2.4 MODAL GAIN, MODAL ABSORPTION, SPONTANEOUS EMISSION AND P_F 24

2.41 Modal Absorption 24

2.42 Modal Gain 25

2.43 Spontaneous Emission 26

2.44 Population Inversion Factor 27

2.5 CARRIER DISTRIBUTIONS – THERMAL AND NON-THERMAL 28

2.5 GAIN- CURRENT RELATIONSHIP IN QUANTUM DOT LASERS 30

2.6 SUMMARY 31

3. MEASUREMENT TECHNIQUES AND EXPERIMENTAL DETAILS 32

3.1 INTRODUCTION 32

3.2 DEVICE PREPARATION AND TESTING 34

3.21 Device Fabrication 34

3.22 IVL Measurements 35

3.23 NearField Emission 38

3.3 EXTRACTION OF THE THRESHOLD CURRENT DENSITY FROM THE LI CURVE 40

3.4 SEGMENTED CONTACT METHOD - EXPERIMENTAL SETUP 42

3.5 THE SEGMENTED CONTACT METHOD – EXPERIMENTAL TECHNIQUE 44

3.51 Modal Absorption and Modal Gain 46

3.52 Modifications to the measurement technique 48

3.53 Spontaneous emission 49

3.54 Calibration of the Spontaneous Emission and the P_f function 50

3.6 ERROR ANALYSIS OF DATA EXTRACTED USING THE MULTI-SECTION TECHNIQUE 53

3.7 SUMMARY 54

4. CHARACTERISATION OF A HIGH PERFORMANCE QD LASER DIODE 55

4.1 INTRODUCTION 55

4.2 SAMPLE GROWTH AND STRUCTURAL DETAILS 57

4.3 MEASURED DATA 58

4.31 Modal Absorption Measurements 58

4.32 Spontaneous Emission Measurements 62

4.33 Modal Gain Measurements 65

4.4 INTERPRETATION AND DISCUSSION OF RESULTS 68

4.41 Modal Absorption 68

4.42 Spontaneous Emission 70

4.43 Modal Gain 72

4.5 CONCLUSION 74

5. CHARACTERISATION OF A QD LASER DIODE INCORPORATING TUNNEL INJECTION 75

5.1 INTRODUCTION 75

5.2 SAMPLE GROWTH AND STRUCTURAL DETAILS 78

5.3 MEASURED DATA 81

5.31 Edge Photo-Voltage Spectroscopy Measurements 81

5.32 Laser Threshold and Temperature Stability 82

5.33 Modal Absorption Measurements 85

5.34 Spontaneous Emission Measurements 91

5.35 Modal Gain Measurements 95

5.4 INTERPRETATION AND DISCUSSION OF RESULTS 98

5.41 Edge Photo-Voltage Spectroscopy Measurements 98

5.42 Laser Threshold and Temperature Stability 98

5.43 Modal Absorption Measurements 101

5.44 Spontaneous Emission Measurements 103

5.45 Modal Gain Measurements 105

5.5 CONCLUSION 109

6. CARRIER DISTRIBUTIONS IN QUANTUM DOT LASER DIODES 110

6.1 INTRODUCTION 110

6.2 INTERPRETATION OF P_F SPECTRA 112

6.3 CARRIER DISTRIBUTION IN THE HP STRUCTURE – MEASURED DATA 115

6.4 INTERPRETATION AND DISCUSSION OF RESULTS FOR THE HP STRUCTURE 119

6.5 CARRIER DISTRIBUTION WITHIN THE TI STRUCTURE 122

6.6 CARRIER DISTRIBUTION WITHIN THE TI STRUCTURE – MEASURED DATA 123

6.7 INTERPRETATION AND DISCUSSION OF RESULTS 129

6.8 SUMMARY 132

7. SUMMARY CONCLUSIONS AND FURTHER WORK 133

7.1 SUMMARY AND CONCLUSIONS 133

7.2 FURTHER WORK 136

7.3 REFERENCES 137

1. Introduction

The focus of this thesis is to increase the understanding of how carriers populate electronic states of InAs quantum dot (QD) laser diodes which operate near 1.3μm, especially those which incorporate tunnel injection. In this section of the thesis I will explain the motivation behind the work I have undertaken. I will discuss how this work provides both confirmation of previously untested hypotheses and original results which increase the understanding of the physical processes underlying the operation of QD lasers.

1.1 Aims and Motivation

Self-assembled QD lasers have shown superior characteristics when compared to commercially used InP based quantum well (QW) lasers [1]. These include a temperature insensitive threshold current density [2-4] and a less complicated manufacturing process for GaAs based vertical cavity surface emitting lasers (VCSELS) emitting at 1.3μm [5,6]. Despite these and other superior characteristics, QD lasers have not reached their theoretically predicted "ideal" characteristics [7, 8]. This is due to inhomogeneous broadening of spectra [9, 10] caused by the size distribution of dots within an ensemble and the presence of a wetting layer [11].

A major factor in understanding the performance of these devices is the distribution of electrons in energy, under operating conditions. By understanding how electrons populate these systems, QD laser structures can be designed to maximise their performance. It has been shown that in many cases, at room temperature and above, the carrier distribution of a QD laser can be described by Fermi-Dirac statistics [12-14]. Their performance at lower temperature is not well understood and in this work I will highlight how the population of a QD laser changes at lower temperatures.

I used the newly found understanding of QD behaviour, as well as previously understood characteristics, to explore the properties of a tunnel injection QD laser. This type structure was proposed by Asryan and Luryi [15] to remove the influence of the wetting layer and higher energy QD states on the performance of the QD laser. The electrons bypass these higher energy states altogether though resonant tunnelling of "cold" electrons from an adjacent injector well, into the QD lasing state.

It was also predicted that the resonant tunnelling process might inherently select QDs of the "right" size leading to an effective narrowing of the inhomogeneous line width [15]. For such an approach to be beneficial the carriers must recombine before they are able to re-equilibrate throughout the dot ensemble and it was unclear, prior to the work shown in this thesis, to what extent this is true.

The electron relaxation rate into the QD lasing state is proposed to be limited by slow relaxation from the wetting layer [11] and by slow relaxation between the QD states themselves [16].

The tunnel injection structure examined in this thesis provides a unique opportunity to analyse which of these performance limiting factors is dominant due to the injection taking place into the QD first excited state. Provided the thermalisation of carriers out of the QD is negligible, comparison between the differential gain of a typical QD laser and a QD laser which incorporates tunnel injection would help to clarify this issue.

1.2 Thesis Structure

In Chapter two I review the historical development of QDs lasers. I discuss the most widely used growth method for QDs, including the benefits and consequences of using this technique. I describe and produce rate equations for the radiative transitions which take place in a two level system and how the electron distribution in energy can be analysed. I finally discuss the analysis of modal gain for electrically driven QD lasers as this is used extensively in later chapters.

In Chapter three I describe the measurement techniques used in this thesis and briefly those used by other researchers to analyse the radiative recombination processes in QD lasers. This includes sample preparation details, the measurement apparatus used and introduces the segmented contact method (SCM) [17].

I show the properties of a high performance QD laser, obtained using the SCM in Chapter four and use these results to compare with and understand the results obtained in the following chapters.

In Chapter five I use similar techniques to that in Chapter four to fully characterise a tunnel injection QD laser. I also include laser threshold vs temperature measurements to show the performance of this structure under operating conditions.

In chapter six I analyse the carrier distribution in both the high performance QD laser and the tunnel injection laser. I will use the results from the previous chapters to provide an explanation for the features observed and from an understanding of the performance of these devices, under various operating conditions.

2. Background Theory

In this chapter I provide the background theory relevant to understanding the work discussed in the remainder of this thesis. I start by reviewing the historical development of quantum dot (QD) lasers, followed by a discussion of the main growth method currently employed, including the benefits and drawbacks of using this technique.

I will describe and produce rate equations for the radiative recombination processes which take place in a general two level system. These equations are then manipulated to show how measured data can be used to analyse the carrier distribution within QD lasers.

I finally discuss the energy states present in a typical QD ensemble and what conditions are necessary for a thermal or non-thermal carrier distribution to be present.

2.1 Brief History of the Quantum Dot Laser

The idea of a QD laser was first proposed by Dingle and Henry in 1976 [18]. Their patent described quantum effects in diode lasers, which become apparent when the dimensions of the active layer are reduced in one, two or three dimensions. A more detailed description of a QD laser and its potential temperature insensitive characteristics was given by Arakawa and Sakaki in 1982 [8]. The authors proposed the application of magnetic fields to a quantum well (QW) laser to provide confinement in all three dimensions. This approach was unsuitable for commercially used devices.

Most applications of diode lasers require mass production and so a major breakthrough came from Goldstein et al (1985) [19], who grew QDs by self-assembly (growth discussed in section 2.22). Following this the idea of using QDs as the active media in diode lasers became realistic [20]. The formation of islands with approximately 10nm dimensions leads to the localisation of electrons in all three dimensions. In an individual dot, the conventional band structure seen in semiconductors is reduced to a series of discrete energy levels [21].

Since the early 1990s the development of QD lasers has advanced rapidly to include many material systems such as; InAs/GaAs [22,23], InP/GaP [24,25], GaInNAs/GaAs [26,27] and exhibit properties superior to strained QW systems in some respects [28].

2.2 Quantum Dot Formation

2.21 Stranski-Kranstanow Growth of QDs

The most commonly used method to form QDs in the active region of a semiconductor diode laser is by self-assembly using the Stranski-Krastanow growth mode. This growth mode occurs when a semiconductor material is deposited epitaxially onto another semiconductor, of significantly different lattice constant [31].

For the InAs/GaAs material system, a lattice parameter mismatch of approximately 7% is required for this growth mode to occur. The initial few mono-layers deposited form a planar layer known as the wetting layer. As further atomic layers are deposited, three dimensional islands form on top of the planar layer. This minimises the elastic strain caused by the mismatch in the lattice constants between the semiconductor materials.

The QDs and wetting layer are usually grown on top of, and capped with, materials to minimise strain between these layers and subsequent optical confinement layers. The optical confinement layers form a planar waveguide, so that the light within the optical cavity is confined in the same spatial location as the localised charge carriers. An illustration of a quantum dot waveguide is shown in Figure 2.1.

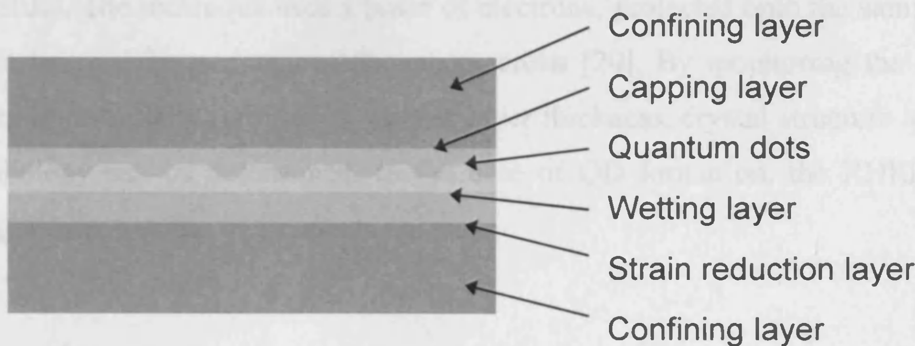

Figure 2.1 – Illustration of a self-assembled QD laser waveguide

The self-assembly process leads to typical dot densities of 10^{10}-$10^{11}cm^{-2}$, with dimensions 5nm high and base dimensions 20nm x 20nm [31]. The size and composition of the dots can be controlled by adjusting the growth temperature and the amount of material deposited. This leads to control of the emission wavelength as larger dots emit at longer wavelengths.

These structures are usually grown by Molecular Beam Epitaxy (MBE) or Metal-Organic Chemical Vapour Deposition (MOCVD). As the structures described in this thesis were grown by MBE I shall briefly review this process.

2.22 Molecular Beam Epitaxy

MBE has been used for epitaxial growth of periodic structures with uniform chemical composition since the work by Cho in 1971 [32]. It can produce high quality layers with abrupt interfaces at the atomic level, as required to form complex structures such as QD lasers.

The growth introduces elements from heated effusion cells onto heated semiconductor substrates. The elemental sources are highly pure and the growth takes place under high vacuum to maximise growth quality. The layer composition and thickness is controlled by the abrupt opening and closing of shutters on the effusion cells [32].

The growth is monitored by reflection high-energy electron diffraction (RHEED). The technique uses a beam of electrons, projected onto the sample surface before being diffracted onto a phosphor screen [20]. By monitoring the diffraction pattern and intensity, properties such as layer thickness, crystal structure and surface morphology can be determined. In the case of QD formation, the RHEED pattern changes from a series of streaks to spots.

2.23 Broadening in Self-Assembled QD Lasers

Although self-assembled growth has led to the realisation of QD lasers as commercially applicable devices, this formation method does lead to certain undesirable characteristics. During the self-assembly process the dots form with a distribution of sizes and compositions. These could arise from fluctuations in surface roughness, surface temperature or the ion concentrations within the chamber [20]. As a result the quantised energy levels within the individual dots vary in energy throughout the ensemble. This leads to an inhomogeneous broadening of the spectral line width typically ≥ 20meV [31].

In addition to the inhomogeneous broadening, the spectral line width will also incorporate homogeneous broadening. The main contributions to homogeneous broadening in diode lasers are: uncertainty in the energy of the confined electron and interaction of the confined state with the high frequency lattice vibrations [33]. The uncertainty in the electron energy is a result of the relatively short time an electron have a particular energy due to collisions and recombination processes. From the Heisenberg uncertainty principle, the relatively short time leads to an uncertainty in its exact energy. These broadening processes broaden the spectral emission from all the dots within the ensemble in equal amounts and the magnitude of this in InGaAs QDs has been estimated to be 6meV at 300K by Borri et al. [34].

The combined effect of the two broadening mechanisms on the ground state spectral line width is illustrated in Figure 2.2. The homogeneous line width has broadened the individual transitions and the inhomogeneous line width has shifted the peak energy of the transitions from the different dots within the ensemble.

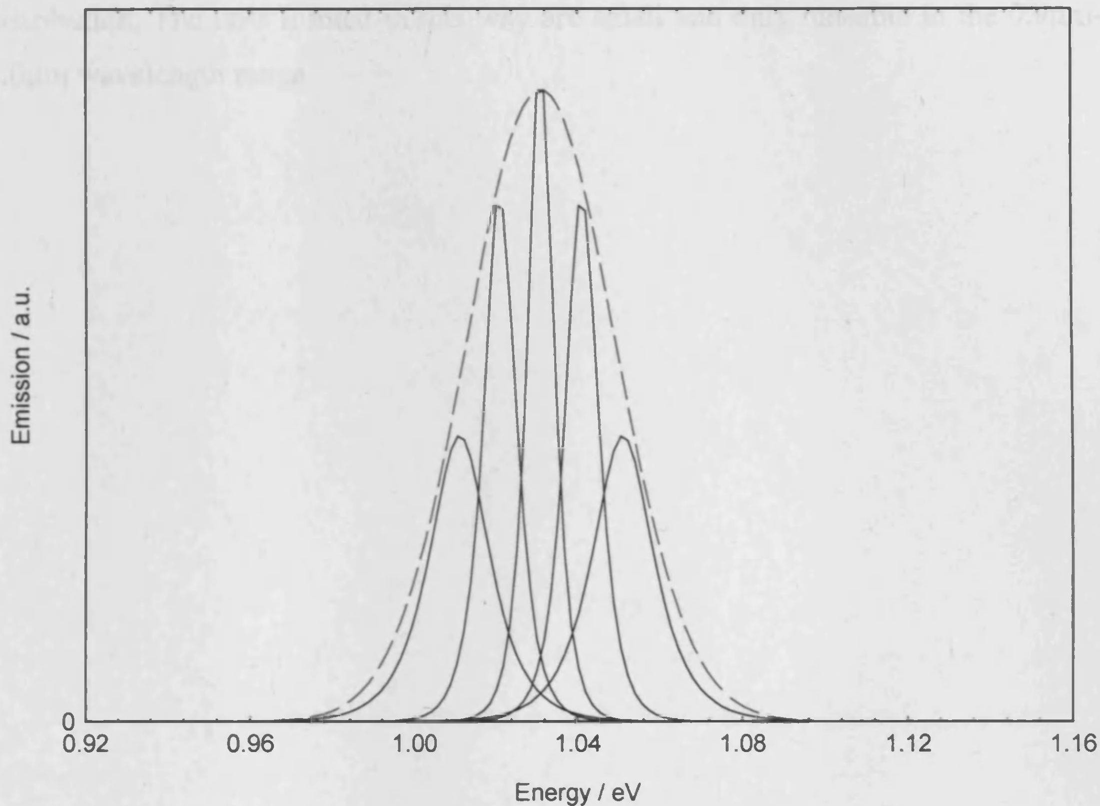

Figure 2.2 – Illustration the spectral broadening caused by inhomogeneous and homogeneous broadening. The black lines represent the transitions from the different dots and the blue dashed line the overall emission.

The size distribution of a quantum dot ensemble can be minimised using techniques such as seeding [35] or using sub-monolayer QDs [36]. The seeding technique, (designed to increase dot density) uses a multi-layer design, where the initial layer is formed with a high density of small dots. In the formation of subsequent layers, more material is deposited creating larger dots with an emission wavelength more applicable to the telecommunications industry. These dots vertically align to the smaller dots in the initial layer due to strain through the thin spacer layer.

This leads to a high density of dots formed with a narrow distribution of dot sizes. A drawback of this technique is that the initial dot layer will not produce useful radiative emission at the lasing wavelength of the other dot layers.

Sub-monolayer dots also use a multi-layer design. In this design however, alternate layers of InAs and GaAs are deposited, with the InAs coverage being less than one monolayer. The GaAs spacer layers are thin leading to vertical alignment of the dots and the small amount of InAs deposited leads to a highly uniform distribution. The dots formed in this way are small and only tuneable in the 0.9μm-1.0μm wavelength range.

2.3 Optical Absorption and Radiative Recombination

In this section I consider the optical transitions that take place in a general two level system, following the approach taken by Fox (2001) [29].

2.31 Optical Transitions in Semiconductor Lasers

An electron occupying an energy state (E_1) can undergo a transition to a higher energy state (E_2) by the absorption of a photon of energy $\hbar\omega$, where:

$$E_2 - E_1 = \hbar\omega \qquad \text{Equation 2.2}$$

Similarly an electron in an excited state (E_2) can undergo a transition to a lower energy state (E_1) by the emission of a photon of energy $\hbar\omega$. From statistical physics an electron in an excited state will eventually relax to a lower energy state in a spontaneous process. The relaxation process can also be stimulated by an incoming photon. In this case the emitted photon will be coherent with the stimulating photon i.e. it is of equal energy, equal phase and travelling in the same direction. The three processes described above are illustrated in Figure 2.3.

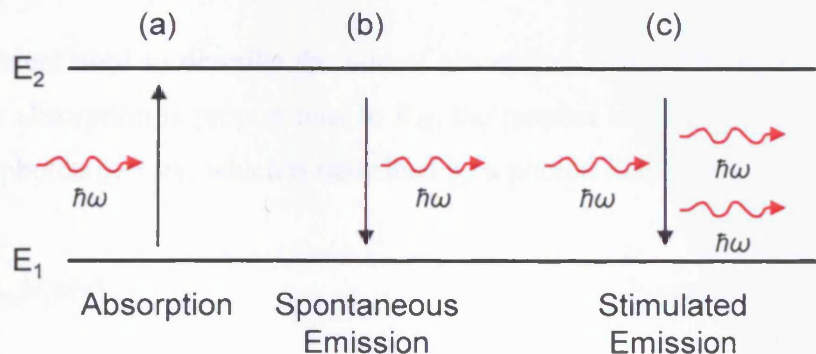

Figure 2.3 – Optical transitions which take place in a semiconductor laser diode.

It should be noted that an electron in an excited state can also relax to a lower energy state via non-radiative processes such as Auger recombination or recombination via a defect state, located between the two energy states. As the work presented in this thesis does not directly analyse these non-radiative processes they will not be considered further, however further information can be found in work by Sandall 2006 [37].

2.32 Transition Rate in a Two Level System

Rate equations for the transitions in a two level system can be formed using quantum mechanics and from the work of Einstein (1917) [38]. By writing expressions which describe the rate of absorption and radiative recombination we are able to form an expression comparing the overall transition rate.

Einstein introduced three coefficients to describe the probability per unit time that a particular transition occurs. The A_{21} coefficient expresses the rate of spontaneous emission. The downward transition rate due to spontaneous emission is proportional to both A_{21} and the number of electrons in this state N_2.

$$R^{spon}_{\downarrow} = -A_{21}N_2 \qquad \text{Equation 2.3}$$

The coefficient used to describe the rate of absorption is B_{12}. The upward transition rate due to absorption is proportional to B_{12}, the number of electrons in this state N_1 and to the photon density, which is described by a photon field $\varepsilon(v)$.

$$R^{abs}_{\uparrow} = -B_{12}N_1\varepsilon(v) \qquad \text{Equation 2.4}$$

A similar expression is used to describe the downward transition rate due to stimulated emission, this time the Einstein coefficient is B_{21}.

$$R^{stim}_{\downarrow} = -B_{21}N_2\varepsilon(\nu)$$ Equation 2.5

We can now form an overall expression for the rate of upward and downward transitions due to absorption, spontaneous emission and stimulated emission by adding Equations 2.3-2.5.

$$R^{abs}_{\uparrow} = R^{spon}_{\downarrow} + R^{stim}_{\downarrow}$$ Equation 2.6

$$B_{12}N_1\varepsilon(\nu) = A_{21}N_2 + B_{21}N_2\varepsilon(\nu)$$ Equation 2.7

Equation 2.7 is in the steady state where the system has had enough time to equilibrate. It will be used in Section 2.34 to show a relationship between the Einstein coefficients. In order to show this I first introduce Fermi-Dirac statistics.

2.33 Fermi-Dirac Statistics and Population Inversion

We can relate the behaviour of a system as a whole to the properties of the particles within the system using statistical physics. This can be used to obtain the most likely distribution in energy, of particles within a system, which are in thermal equilibrium at a temperature T [41].

In thermal equilibrium the rate of excitation exactly equals the rate of relaxation between two states. For light emission to take place from a laser cavity, additional charge carriers must be introduced into the higher energy state so that its population exceeds that of the lower level. A system populated in this way it said to be inverted.

The charge carriers in semiconductor lasers are electrons, which obey the Pauli exclusion principle. The probability an electron occupies a state of energy E can be described by a Fermi-Dirac distribution [39]:

$$f = \frac{1}{e^{\frac{E-E_F}{KT}} + 1}$$ Equation 2.8

f is the probability a state at energy E is occupied and E_f is the Fermi level. In a system where an inverse population has been introduced, equilibrium statistics no longer apply and so to describe the occupation of energy states E_1 and E_2 quasi-Fermi levels are introduced. This assumes electrons are able to thermally redistribute throughout the system at a rate faster than the recombination rate.

$$f_i = \frac{1}{e^{\frac{E_i-E_{fi}}{kT}} + 1}$$ Equation 2.9

where E_{fi} is quasi-Fermi level describing the population of state i. For an inverted population to exist between energy states 1 and 2, $f_2 > f_1$. Comparing the occupation probabilities for an electron in state E_1 and E_2 we arrive at the condition for population inversion.

$$e^{\frac{E_2-E_{f2}}{kT}} > e^{\frac{E_1-E_{f1}}{kT}}$$ Equation 2.10

which reduces to:

$$\Delta E_f > E_2 - E_1$$ Equation 2.11

where ΔE_f is the quasi-Fermi level separation.

2.34 Relationship between the Einstein Coefficients

The number of electrons which occupy an energy level E_i in a two level system can be described by the occupation probability functions introduced in Section 2.33. To form a relationship between the Einstein coefficients we must first form an expression relating the population of the states E_1 and E_2 using Equation 2.9.

$$\frac{N_2}{N_1} = \frac{f_2(1-f_1)}{f_1(1-f_2)} = e^{-\frac{(E_2-E_1)}{kT}} = e^{-\frac{(h\nu_{21})}{kT}} \qquad \text{Equation 2.12}$$

We can now introduce Plank's law for black body radiation to describe the photon field [39]:

$$\varepsilon(h\nu) = \frac{n^3(h\nu)^2}{\pi^2\hbar^3c^3}.\frac{1}{e^{\frac{h\nu}{kT}}-1} \qquad \text{Equation 2.13}$$

Assuming $B_{12} = B_{21}$, an expression can be formed relating the Einstein coefficients by comparing Equations 2.7, 2.12 and 2.13 [40].

$$A_{21} = \frac{n^3(h\nu)^2}{\pi^2\hbar^3c^3}B_{21} \qquad \text{Equation 2.14}$$

This means that when one of the Einstein coefficients is known we are able to work out the other two. Equations 2.13 and 2.14 are used in Section 2.4 to produce expressions for modal gain, modal absorption and spontaneous emission.

2.4 Modal Gain, Modal Absorption, Spontaneous Emission

In this section I use the rate equations from Section 2.3 to produce expressions for the modal gain, modal absorption and spontaneous emission. I also show that the relationship between these expressions can be used to analyse the degree of inversion, at a particular energy, through the population inversion factor. To do this I use the approach of Thomson (2000) [41].

2.41 Modal Absorption

From comparison between the upward and downward stimulated transitions when $f_1 > f_2$, an expression can be formed for the net stimulated transition rate R_{12}^{Stim}. This rate is proportional to the Einstein coefficient B_{12}, the density of states functions $\rho_{1,2}$, the occupation probability of these states $f_{1,2}$ and the photon density $\varepsilon(h\nu_{21})$.

$$R_{12}^{Stim} = B_{12}\rho_1\rho_2(f_1 - f_2)\frac{1}{w_{mod}}\varepsilon(h\nu_{21}) \qquad \text{Equation 2.15}$$

w_{mod} is the effective mode width. This is defined as the width of a rectangle, equal in area to the optical mode and equal in intensity to the optical mode at the active region [43]. This is illustrated in Figure 2.4.

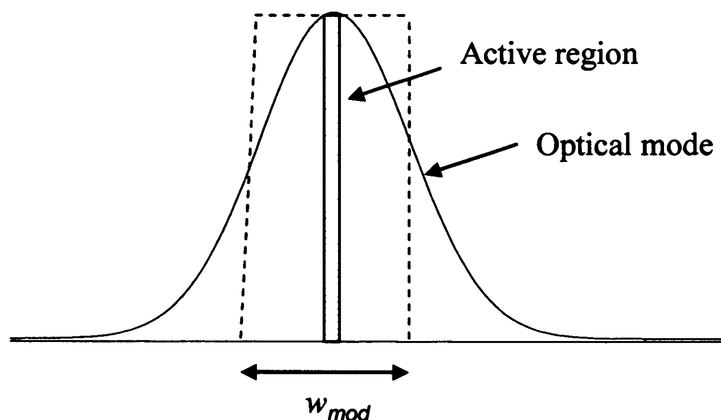

Figure 2.4 – Illustration of the effective mode width (w_{mod}).

The net stimulated absorption rate is proportional to the modal absorption $\alpha(hv_{21})$ and the photon flux. The photon flux is the product of the photon density and the group velocity V_g.

$$R_{12}^{abs} = \alpha(hv_{21})\varepsilon(hv_{21})V_g \qquad \text{Equation 2.16}$$

From comparison between Equations 2.15 and 2.16 an expression is obtained for the modal absorption:

$$\alpha(hv_{21}) = \frac{n}{c} B_{12}\rho_1\rho_2(f_1 - f_2)\frac{1}{w_{\text{mod}}} \qquad \text{Equation 2.17}$$

Here the group velocity has been replaced by n / c, where n is the refractive index and c the speed of light.

2.42 Modal Gain

A similar procedure can be used in the case where $f_2 > f_1$. From this an expression for the net stimulated emission rate is obtained:

$$R_{21}(st) = B_{21}\rho_1\rho_2(f_2 - f_1)\frac{1}{w_{\text{mod}}}\varepsilon(hv_{21}) \qquad \text{Equation 2.18}$$

The average energy in an optical mode $\langle E \rangle$ is given by [39]:

$$\langle E \rangle = \frac{hv_{21}}{e^{\frac{hv_{21}}{kT}} - 1} \qquad \text{Equation 2.19}$$

We can use this to express the stimulated emission rate as a function of photon energy:

$$R_{21}^{Stim}(hv_{21}) = B_{21}\frac{n^3(hv_{21})^2}{\pi^2\hbar^3c^3}\rho_1\rho_2(f_2 - f_1)\frac{1}{w_{\mathrm{mod}}}$$ Equation 2.20

Assuming $B_{12} = B_{21}$, Equations 2.17 and 2.20 can be compared to reveal the relationship between the modal absorption and the stimulated emission rate:

$$\alpha(hv_{21}) = -\frac{\pi^2\hbar^3c^2}{n^2(hv_{21})^2}R_{21}^{Stim}(hv_{21})$$ Equation 2.21

The modal absorption and modal gain are related by $\alpha(hv_{21}) = -G(hv_{21})$. When $f_2 > f_1$ modal absorption becomes modal gain [40].

2.43 Spontaneous Emission

The spontaneous emission rate is proportional the Einstein A_{21} coefficient, the density of states functions $\rho_{1,2}$ and the occupation probability of these states $f_{1,2}$.

$$R_{21}^{Spon}(hv_{21}) = A_{21}\rho_1\rho_2 f_2(1 - f_1)$$ Equation 2.22

Comparing Equation 2.22 with Equation 2.14 we can form an equation in terms of the Einstein B_{21} coefficient.

$$R_{21}^{Spon}(hv_{21}) = B_{21}\frac{n^2(hv_{21})^2}{\pi^2\hbar^3c^2}\rho_1\rho_2 f_2(1 - f_1)$$ Equation 2.23

This allows an expression for modal gain to be formed in terms of the spontaneous emission rate from comparison between Equations 2.20, 2.21 and 2.23.

$$\frac{G(h\nu_{21})}{R_{21}^{Spon}(h\nu_{21})} = \frac{\pi^2\hbar^3c^2}{n^2(h\nu_{21})^2}\frac{1}{w_{\text{mod}}}\frac{(f_2 - f_1)}{f_2(1-f_1)}$$ Equation 2.24

2.44 Population Inversion Factor

In Equation 2.24 the ratio of the modal gain and spontaneous emission is proportional to the degree of inversion of the system, as described by the occupation probabilities $f_{1,2}$. The occupation probabilities $f_{1,2}$ are energy dependent functions which vary between 0 and 1 reflecting unoccupied or fully occupied states respectively. These probabilities are general and do not require any equilibrium to be present. Blood et al. (2003) [17] define a population inversion factor $P_f(h\nu_{21})$.

$$P_f(h\nu_{21}) = \frac{(f_2 - f_1)}{f_2(1-f_1)} = \frac{G(h\nu_{21})}{R_{21}^{Spon}(h\nu_{21})}\frac{n^2(h\nu_{21})^2}{\pi^2\hbar^3c^2}w_{\text{mod}}$$ Equation 2.25

If the electrons are distributed according to Fermi-Dirac statistics $P_f(h\nu_{21})$ can be described by [12]:

$$P_f = 1 - \exp\left[\frac{E_{21} - \Delta E_f}{kT}\right]$$ Equation 2.26

Equations 2.25 and 2.26 are used extensively in Chapter six of this thesis to analyse the carrier distribution within long wavelength quantum dot laser diodes.

2.5 Carrier Distributions – Thermal and Non-Thermal

In this section I introduce the concept of carrier distributions within a QD laser. Rate equation models are often used to model carrier distributions within semiconductor lasers, particularly those in quantum wells (QWs) [44]. This approach works well for QW lasers where electrons in a particular band can move throughout that band, when they have enough thermal energy. Self-assembled QDs are however spatially isolated from one another, so an electron occupying an energy state in one dot may not be able to occupy the same, or a more favourable state within another dot.

Dots throughout the ensemble form with a distribution of sizes and compositions, leading to an inhomogeneous broadening of the spectral emission. This broadening does not necessarily reflect the electrons' ability to redistribute thermally throughout the ensemble, but can be a result of random capture of electrons as described by Grundmann et al (1997) [45].

To illustrate the effect of spatial isolation I have formed a diagram which illustrates two dots, each with one confined state (Figure 2.5). In this diagram the two dots illustrated are spatially separated (x axis). They have different sizes and compositions associated with them, hence their energy levels and conduction band offsets differ.

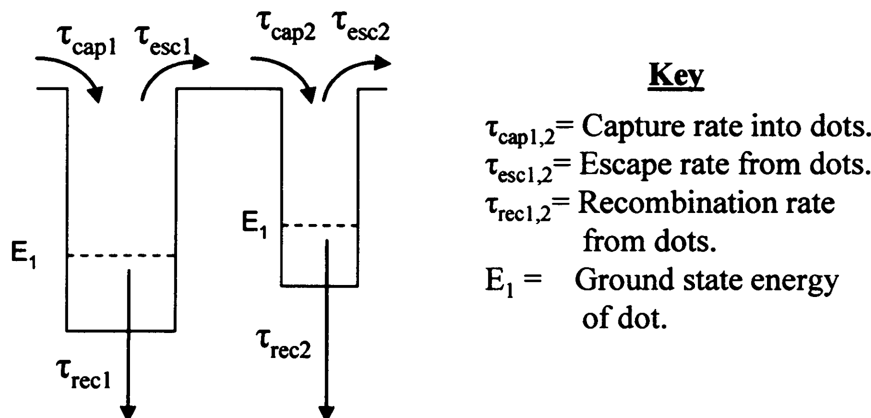

Figure 2.5 – Illustration of the escape and capture process for spatially isolated QDs.

To establish a thermal distribution, where the electrons are distributed according to Fermi-Dirac statistics, electrons must be able to thermally excite out of each dot into the wetting layer. They must then spatially relocate across the wetting layer before scattering into a more favourable state within a different dot. Another proposed way in which electrons can thermally distribute throughout the QD ensemble is by photon mediation [46]. An electron could conceivably radiatively recombine from one dot and the photon emitted could be reabsorbed by another dot elsewhere in the ensemble.

The redistribution process must be faster than the QD recombination rate in order to achieve a thermal distribution. Most self-assembled QD contain multiple confined states, however many models of QD lasers fail to account for the contribution of higher energy dot states [47]. In addition to the relaxation rate from the wetting layer, the intradot relaxation rate is also fundamentally important.

A thermal distribution is a statistical description allowing us to predict the average energy of electrons within a particular system and the probability of occupancy of a state of energy E. For the reasons discussed above this need not apply in QD structures while being electrically pumped, particularly at low temperature. A major part of this thesis is devoted to understanding the distribution within quantum dot laser structures and in Chapter six I illustrate how dot systems deviate from thermal distributions at low temperature.

2.6 Gain- Current Relationship in Quantum Dot Lasers

An important characteristic of a semiconductor diode laser is its gain-current characteristic. From this the laser threshold current density, gain saturation effects and the differential gain can be observed. When analysing this data for QW lasers it is commonly accepted that the gain-current characteristic can be approximated by [39]:

$$G = G_0 \ln\left[\frac{J}{J_t}\right] \qquad \text{Equation 2.27}$$

G is the modal gain, G_0 is a fitting parameter, J is the current density and J_t is the transparency current density. This expression is however applicable only for a single sub band. In QD lasers we must account for the existence of higher energy states and inhomogeneous broadening when considering the gain-current characteristic [20]. To this end it has been shown that measured modal gain-current characteristic can be approximated by [48]:

$$G = G_{sat}\left[1 - e^{-\gamma\frac{J-J_t}{J_t}}\right] \qquad \text{Equation 2.28}$$

G_{sat} represents the saturated modal gain for a particular QD state and γ is a dimensionless fitting parameter which accounts for the interaction between the QD states and the inhomogeneous broadening. This equation will be used in fitting the gain-current curves in Chapters four and five to aid in their comparison.

2.7 Summary

In this chapter I have shown and discussed the background theory relevant to understanding the work discussed in the remainder of this thesis. I reviewed the historical development of QDs lasers and discussed the main growth method currently employed.

I produced rate equations for the radiative recombination processes which take place in a two level system. These equations were manipulated to show how measured data can be used to analyse the carrier distribution within QD lasers.

I also discussed the energy states present in a typical QD ensemble and what conditions are necessary for a thermal or non-thermal carrier distribution to be present.

3. Measurement Techniques and Experimental Details

3.1 Introduction

In this chapter I review the techniques used to characterise Quantum Dot (QD) laser diodes in this thesis and briefly those used by other research groups. I discuss the sample preparation, the measurement techniques used and the equipment used to make the measurements.

The main experimental technique used in this thesis to characterise the QD structures and to explore the distribution of carriers in these systems, is the segmented contact method (SCM) [17]. The SCM is used to analyse the edge emitted amplified spontaneous emission (ASE) from a laser diode, as a function of electrically pumped device length.

The data acquired from using this technique is used to produce modal absorption, modal gain and spontaneous emission spectra as a function of photon energy. The modal gain and spontaneous emission data can also be used to produce a population inversion function. This describes the carrier population within the conduction and valence bands as a function of photon energy.

The SCM has been used for the work described in this thesis due to the many advantages it has over other characterisation methods [49]. Other techniques used for measuring modal gain require the resolution of longitudinal modes [50], or maintaining constant collection efficiency while sampling light from multiple devices [51]. The SCM does not require resolution of the longitudinal modes or the collection geometry to be changed during a measurement as all the measurements are performed on the same device.

Photoluminescence (PL) measurements are often used to probe the radiative recombination from a structure [52]. They reveal the energy position of various states within the structure and their spectral line width. The intensity of the recombination observed is however in arbitrary units as the excitation power coupled into the waveguide and the fraction of the emitted light collected must be known [53].

PL also utilises optical pumping, which is not used in commercial devices, and can suffer from low signal to noise ratios. Pump probe spectroscopy is also widely used to reveal information about carrier dynamics [34, 54]. The work described in this thesis does not investigate this property directly. However this is discussed further in Section 7.2.

3.2 Device Preparation and Testing

Device fabrication begins by growth at either the University of Michigan or the EPSRC National Centre for III-V Technologies in Sheffield. The wafer material is then processed by Mrs K. Barnett and Dr J. Thomson in the clean room located within the Cardiff University School of Physics and Astronomy.

The devices are processed into lasers and multi-section devices. The multi-section devices are used to perform the SCM, which analyses the edge emitted ASE from a laser diode, as a function of electrically pumped device length. This requires light collection from the facet of the device, whilst selectively electrically pumping different lengths of the device. The ASE collected is then compared so careful control of the light collection geometry and the electrical pumping is paramount for accurate results. This single pass technique is performed using a series of equal length sections, formed during the fabrication process.

3.21 Device Fabrication

The material is fabricated into 50μm wide oxide stripe geometry lasers. For devices used with the SCM, the top electrical contact is divided into 300μm long, electrically isolated sections. A device processed for use with the SCM is illustrated in Figure 3.1.

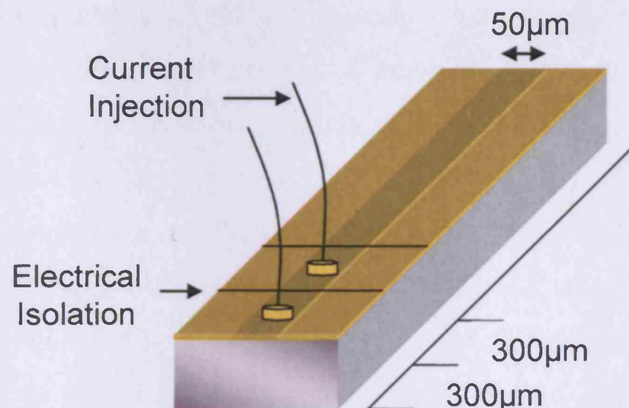

Figure 3.1 – Illustration of a laser diode processed for use with the SCM.

The first two of these sections are used for selective electrical pumping during the measurement. The material is cleaved into devices, of the desired length by trained technical staff. The devices are mounted onto a copper heat sink and a T0-39 transistor header, using a conductive epoxy. Gold wires are attached to the top contact for electrical current injection.

To establish which of the processed devices are suitable for analysis, there are a series of requirements for an acceptable device. A device processed for laser measurements must have; a "mirror like" facet with no visible imperfections so that scattering losses at the facet are minimised, a current-voltage (IV) characteristic which does not indicate any electrical contact problems or leakage paths and a near field profile which shows no evidence of filamentation. These properties will be discussed further in the following sections.

In addition to these requirements, devices suitable for the use with the SCM must have identical IV characteristics, for both the electrically isolated sections. Differences between these characteristics could indicate electrical contact problems of current leakage paths. The level of electrical isolation must also be high enough that only a small fraction of the injected current can leak into another section of the device. Although the percentage of current leakage is current dependent, a difference of less that 4% is found to be acceptable. No effect was observed in the measured results when the injection currents were misbalanced by this amount.

3.22 IVL Measurements

The IV and light-current (LI) characteristics are both measured using the same apparatus, illustrated in Figure 3.2.

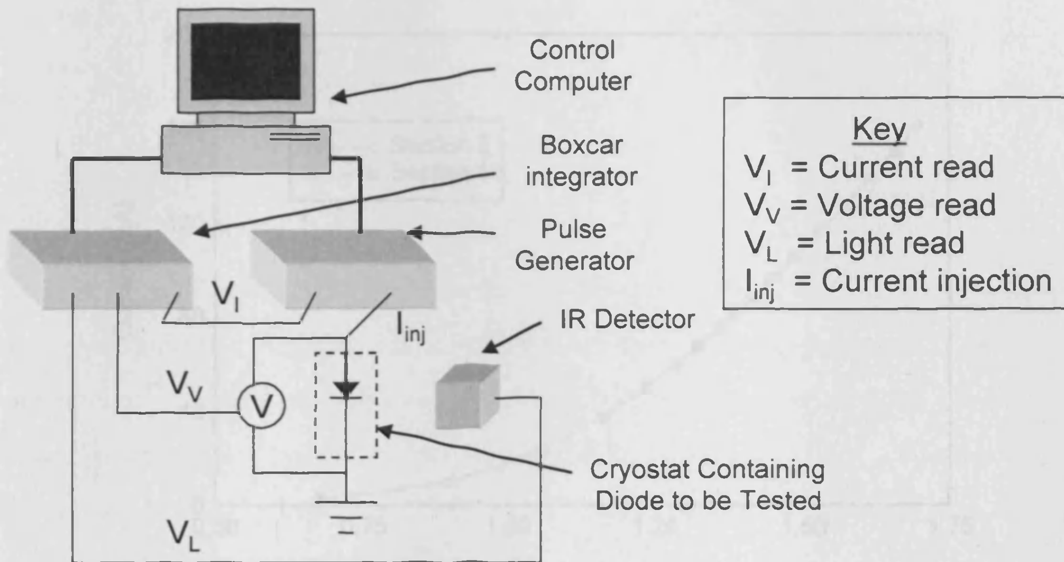

Figure 3.2 – Illustration of IVL measurement apparatus

This computer controlled set of apparatus is used to measure the voltage and light intensity, as electrical current is injected into a device. A pulsed current is used to avoid heating effects; the pulses are typically 500ns in duration and occur at a rate of 5kHz. This leads to a duty cycle of 0.25% which did not cause any observable changes in lasing wavelength, or peak gain as compared to lower duty cycles.

The current, voltage and light intensity levels are sampled using a boxcar integrator. This integrates the signal over a fixed time window using triggered gates. The gates sample the signal when the current pulse is on, increasing the signal to noise ratio. The sample is held in a cryostat for temperature control and the light is detected using a Thorlabs DET410 InGaAs detector.

The IV characteristic is particularly important for the SCM, where specific amounts of current are injected into each section at the appropriate time. It is critical to have identical IV characteristics for each equal length section. At fixed voltage a difference of up to 4% is deemed acceptable, from comparison with measured results with and without a 4% difference. An example of the IV characteristic of a device suitable for multi-section measurements is shown in Figure 3.3.

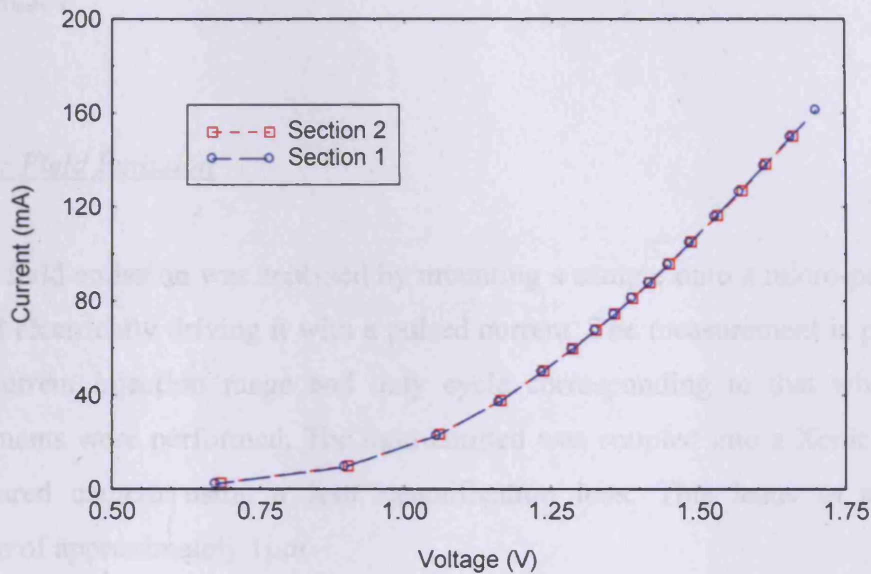

Figure 3.3 – Current-Voltage characteristic of a typical multi-section device.

The device structure used for this technique is illustrated in Figure 3.4. This consists of a series of equal length electrically isolated sections, followed by a long passive absorption section. The absorption section helps to prevent round trip amplification as the SCM requires a single pass ASE measurement.

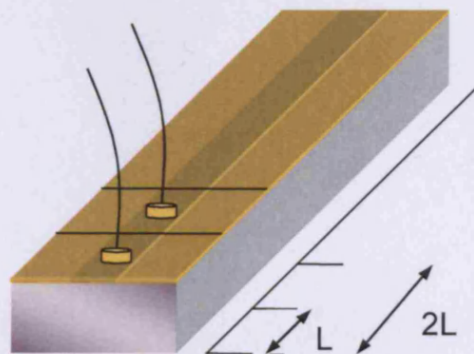

Figure 3.4 – Illustration of a laser diode processed for use with the SCM.

The resistance between the electrically isolated sections is also a vital parameter in multi-section devices. Comparison between the magnitude of this resistance and the diode resistance (gradient of IV characteristic) at a particular voltage allows the leakage current between the sections to be estimated. Typical values of inter-contact resistance lie between 100Ω and 500Ω and estimated leakage currents of up to 4% are deemed acceptable as discussed when measuring the IV characteristics.

3.23 Near Field Emission

The near field emission was analysed by mounting a sample onto a micro-positioning stage and electrically driving it with a pulsed current. The measurement is performed over a current injection range and duty cycle corresponding to that which SCM measurements were performed. The light emitted was coupled into a Xenics XEVA-163 infrared camera using a X10 magnification lens. This leads to a spectral resolution of approximately 1μm.

The emission profile is examined to ensure that light emitted while driving each section, or combination of the two sections, is in a uniform pattern and the same profile exists regardless of which combination of sections is driven. This ensures the emission can be compared while driving the various sections. The data is also examined to ensure no filamentation is present. Figure 3.5 illustrates both a uniform and a non-uniform near field emission profile.

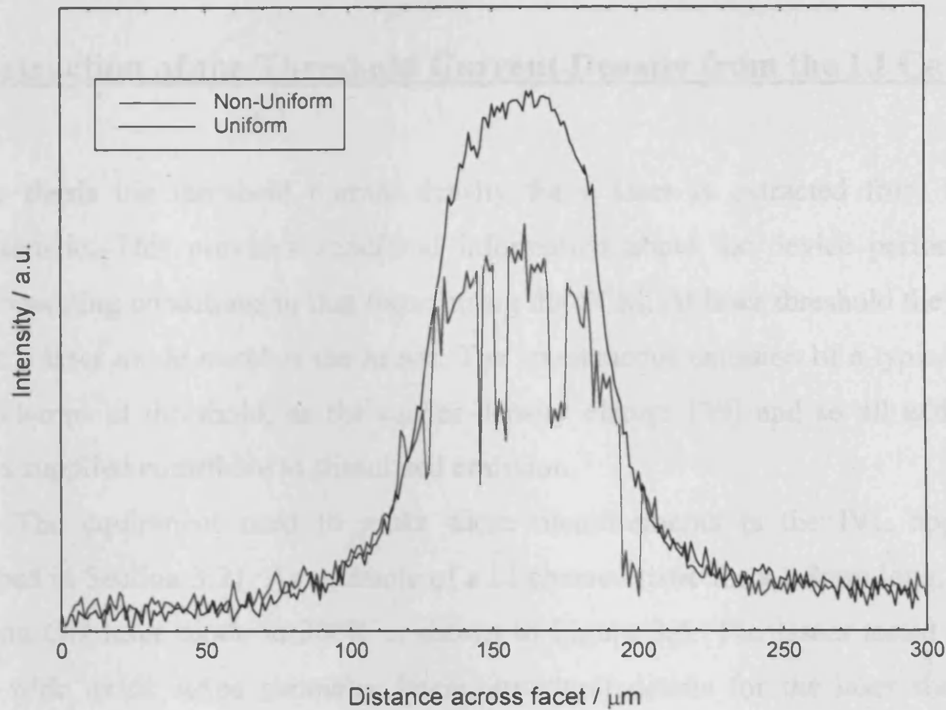

Figure 3.5 – Near field emission from typical QD laser diode illustrating a uniform (black) and non-uniform (blue) near field shape.

The near field measurement also allows the current spreading between the oxide stripe and active region to be estimated, by measuring the full width half maximum (FWHM). For the device with a uniform near field emission in Figure 3.5 the FWHM is 60μm. This corresponds to a current spreading of 5μm either side of the oxide stripe and can be attributed to lateral current spreading in the highly conductive P++ cap material. A structural illustration for this device can be found in Chapter four, Section 4.2.

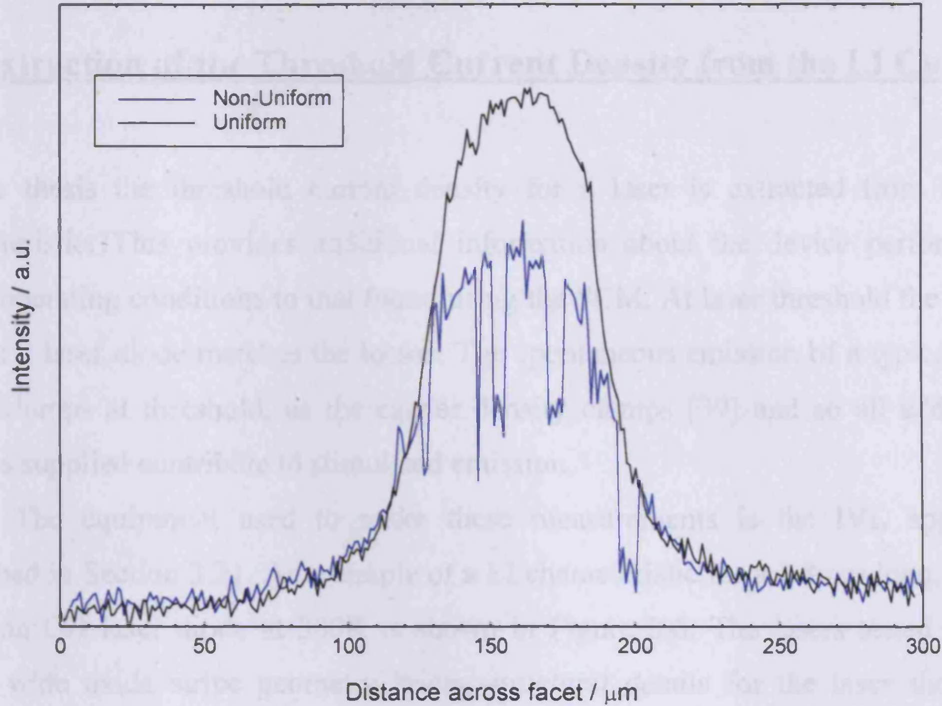

Figure 3.5 – Near field emission from typical QD laser diode illustrating a uniform (black) and non-uniform (blue) near field shape.

The near field measurement also allows the current spreading between the oxide stripe and active region to be estimated, by measuring the full width half maximum (FWHM). For the device with a uniform near field emission in Figure 3.5 the FWHM is 60μm. This corresponds to a current spreading of 5μm either side of the oxide stripe and can be attributed to lateral current spreading in the highly conductive P++ cap material. A structural illustration for this device can be found in Chapter four, Section 4.2.

3.3 Extraction of the Threshold Current Density from the LI Curve

In this thesis the threshold current density for a laser is extracted from the LI characteristic. This provides additional information about the device performance under operating conditions to that found using the SCM. At laser threshold the modal gain of a laser diode matches the losses. The spontaneous emission of a typical laser diode clamps at threshold, as the carrier density clamps [39] and so all additional carriers supplied contribute to stimulated emission.

The equipment used to make these measurements is the IVL apparatus described in Section 3.21. An example of a LI characteristic for a 1.8mm long, tunnel injection QD laser diode at 300K is shown in Figure 3.6. The lasers tested are all 50μm wide oxide stripe geometry lasers, structural details for the laser shown in Figure 3.6 can be found in Chapter five, Section 5.2.

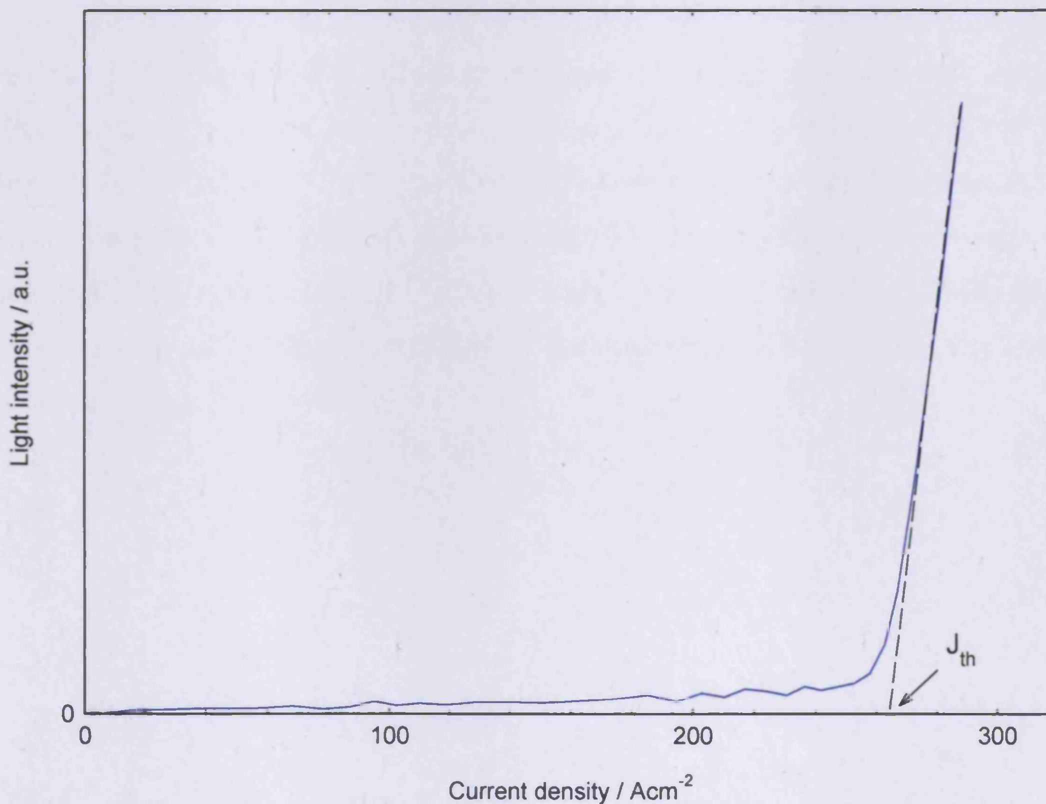

Figure 3.6 – Light-current characteristic for a 1.8mm long tunnel injection quantum dot laser at 300K. The device is driven with a pulsed current with a pulse width of 500ns and a repetition rate of 5kHz.

To extract the threshold current density I identify a region of the curve where the light intensity increases linearly above threshold and extrapolate back to the point where the light intensity = 0. In Figure 3.6 $J_{th} = 265 \pm 10Acm^{-2}$. The error is estimated from the accuracy to which the slope of the LI characteristic above threshold can be determined and from the accuracy of which the length of the device can be determined.

If the gradient of the LI characteristic above threshold abruptly changes, it could be a sign of mode hopping or a switch in the lasing state i.e. ground to first excited state. This can be identified by analysing the wavelength of the lasing emission.

The lasing wavelength for all the lasers described in this thesis was also measured. This was done by coupling the emitted light, via a multimode optical fibre, to an ANDO AQ6317 optical spectrum analyser. For these measurements the devices are driven using the same range of pulsed currents used for the LI measurements.

3.4 Segmented Contact Method - Experimental Setup

The vast majority of the measurements presented in this thesis were taken on a long wavelength spectral analysis experimental setup. This equipment was initially assembled by Mr C Dunscombe and Dr S Osborne and since then it has undergone major improvements through automation and improved signal to noise ratio by Dr D Palmer. The experimental setup can be considered as a combination of four parts: temperature control, automated current injection, light collection, and automated light sampling.

The SCM (outlined in Section 3.2) requires a pulsed current to be supplied to the front two sections of the device either separately or simultaneously while the edge emitted ASE from the device is sampled. This setup consists of; two pulse generators for current supply to section 1 and section 2, a photomultiplier tube for light detection and boxcar integrators to sample the pulsed signals.

The multi-section device is housed within an Oxford Instruments Heliostat cryostat, which keeps the sample at a set temperature within the range 80K to 400K. The cryostat is mounted on a micro-positioning stage capable of aligning over five degrees of freedom. The light emitted is coupled into a Bentham H300E monochromator via a X8.5 magnification lens and infrared polariser. The light is then detected by a Hamamatsu liquid nitrogen cooled photo-multiplier tube (PMT) and its intensity sampled by the boxcar integrator. An illustration of the experimental setup is shown in Figure 3.7.

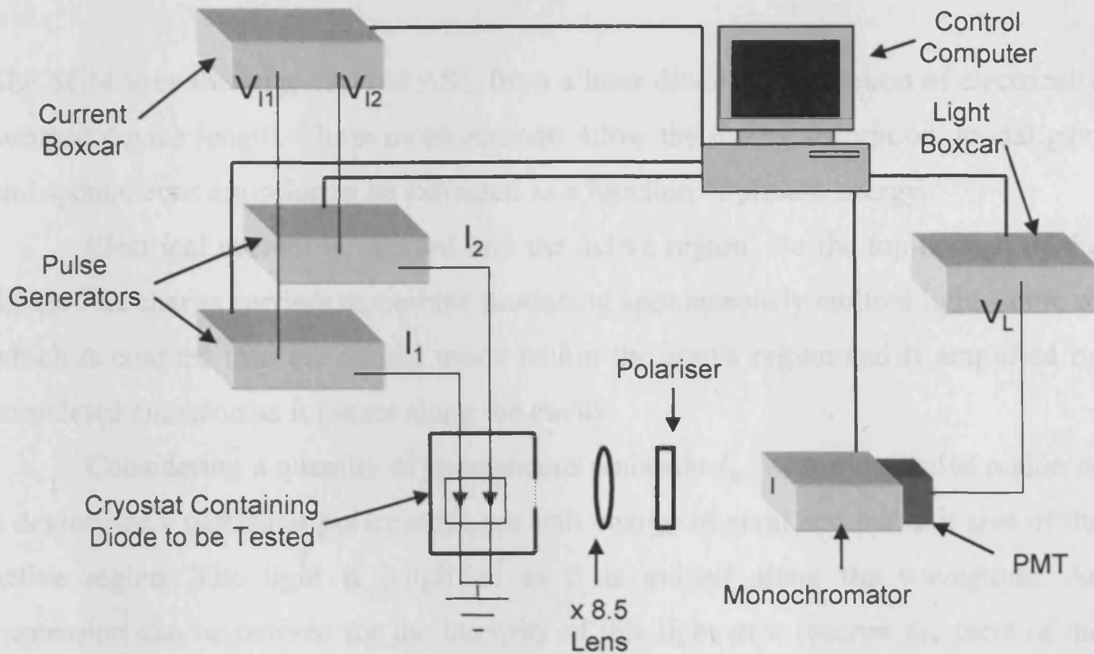

Figure 3.7 – Illustration of the spectral analysis equipment designated N312 where $V_{I1,2}$ are the measured injection currents, V_L is the measured light and $I_{1,2}$ is the current injection into the device.

All the pulse generators and Boxcar integrators were built within the physics department from the design of Mr R Tucker. The boxcar integrators sample the injection current from the pulse generators and the measured light from the PMT. They average the signal for many pulses over a fixed time window using triggered gates, this increases the signal to noise ratio. An illustration of the boxcar integrator gates sampling the light and current pulses during a measurement is shown in Figure 3.8.

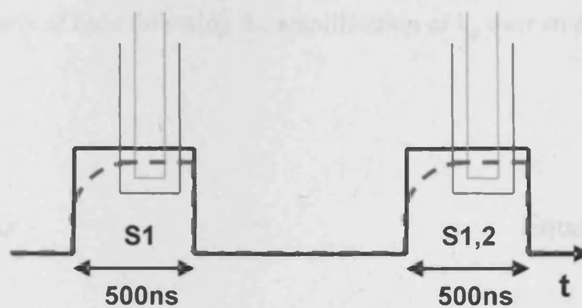

Figure 3.8 – Illustration of current pulses (black), light pulses (red, dashed), current gate (green) and light gate (orange) used for multi-section measurements.

3.5 The Segmented Contact Method – Experimental Technique

The SCM uses the edge emitted ASE from a laser diode, as a function of electrically pumped device length. These measurements allow the modal absorption, modal gain and spontaneous emission to be extracted as a function of photon energy.

Electrical current is injected into the active region, via the top contact of the diode. The charge carriers recombine producing spontaneously emitted light, some of which is coupled into the optical mode within the active region and is amplified by stimulated emission as it passes along the cavity.

Considering a quantity of spontaneous emission I_{sp}, within the active region of a device, for a particular polarisation, per unit energy interval and per unit area of the active region. The light is amplified as it is guided along the waveguide. An expression can be derived for the intensity of this light as it reaches the facet of the device. Considering the amplification of I_{sp} over an element of length Δx an expression can be formed for the intensity of the light at a distance x from the facet of the device.

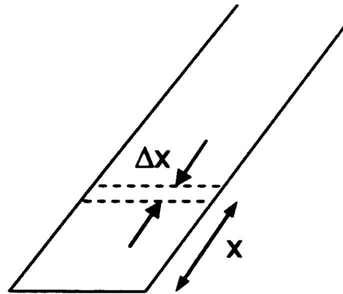

Figure 3.9 – Intensity of light following the amplification of I_{sp} over an element of length Δx.

$$I(x) = \beta I_{sp} e^{(G-\alpha_i)x} \Delta x \qquad \text{Equation 3.2}$$

β is the fraction of the spontaneous emission coupled into the waveguide, G is the modal gain and α_i is the internal waveguide loss. Assuming the intensity of the unamplified spontaneous emission is constant along the region of current injection, the total intensity of amplified spontaneous emission from the end of the device is given by:

$$I_{ASE}(L)=\int_0^L \beta I_{sp}e^{(G-\alpha_i)x}\Delta x=\beta I_{sp}\frac{\left(e^{(G-\alpha_i)L}-1\right)}{(G-\alpha_i)} \qquad \text{Equation 3.2}$$

The ASE collected while electrically driving either the first (front) section of a device or the second section is designated I_{ASE1} and I_{ASE2} respectively, where each section is of length L. The ASE collected while driving both sections 1 and 2 simultaneously is designated $I_{ASE1,2}$. Each section is driven with an equal drive current density.

Expressions can then be formed for the intensity of the ASE using Equation 3.2, as shown in Equations 3.3-3.5.

$$I_{ASE1}=I_{sp}^{meas}\frac{\left(e^{(G-\alpha_i)L}-1\right)}{(G-\alpha_i)} \qquad \text{Equation 3.3}$$

$$I_{ASE2}=I_{sp}^{meas}\frac{\left(e^{(G-\alpha_i)L}-1\right)}{(G-\alpha_i)}e^{(A-\alpha_i)L} \qquad \text{Equation 3.4}$$

A is the modal absorption of the unpumped cavity.

$$I_{ASE12}=I_{sp}^{meas}\frac{\left(e^{(G-\alpha_i)2L}-1\right)}{(G-\alpha_i)} \qquad \text{Equation 3.5}$$

Figure 3.10 illustrates typical ASE spectra as a function of photon energy, taken while testing a multi-section device.

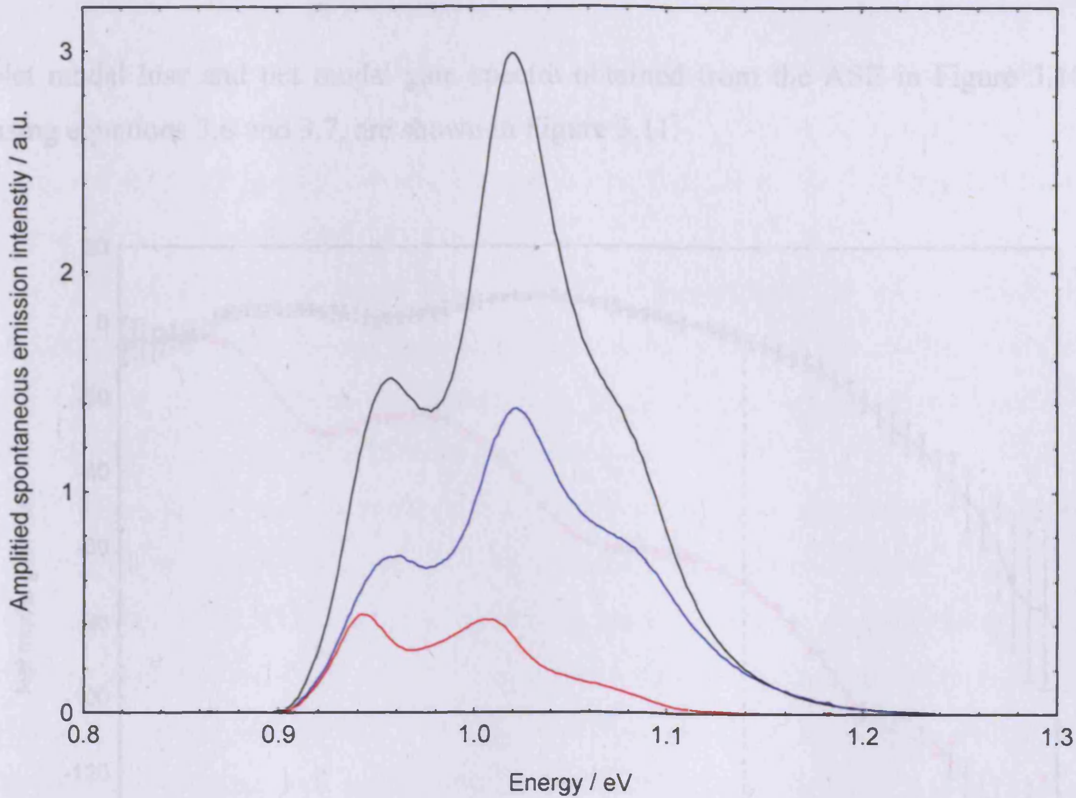

Figure 3.10 – Amplified spontaneous emission collected from the edge of a quantum dot laser diode while driving section 1 (blue), section 2 (red) and sections 1 and 2 (black) at 1111Acm^{-2}.

3.51 <u>Modal Absorption and Modal Gain</u>

We can treat Equations 3.3 and 3.4 as simultaneous equations and solve to obtain an expression for net modal loss $-(A+\alpha_i)$, which is independent of I_{sp}^{meas}, as a function of photon energy.

$$-(A+\alpha_i)=\frac{1}{L}\ln\left[\frac{I_{ASE1}}{I_{ASE2}}\right] \quad \text{Equation 3.6}$$

In a similar way we can treat Equations 3.3 and 3.5 as simultaneous equations and solve to obtain an expression for net modal gain $(G-\alpha_i)$, which is independent of I_{sp}^{meas}, as a function of photon energy

$$G - \alpha_i = \frac{1}{L}\ln\left[\frac{I_{ASE12}}{I_{ASE1}} - 1\right] \qquad \text{Equation 3.7}$$

Net modal loss and net modal gain spectra obtained from the ASE in Figure 3.10, using equations 3.6 and 3.7, are shown in Figure 3.11.

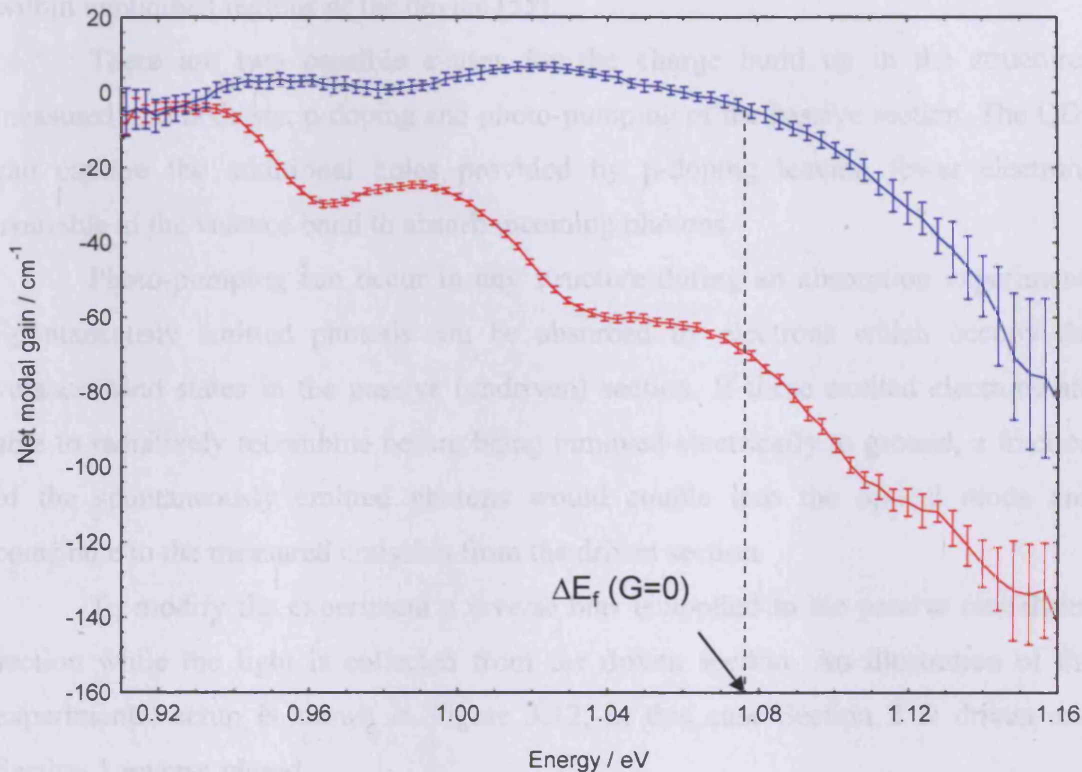

Figure 3.11 – Net modal gain (blue) and net modal absorption (red) plotted as a function of photon energy from a QD laser diode. The error bars are produced using the technique outlined in Section 3.6.

We can extract the internal optical mode loss α_i from the low energy region of either spectrum in Figure 3.11, where the absorption and gain are negligible. At these photon energies there is no resonant absorption or amplification by the cavity so the only loss of intensity can be attributed to scattering losses. The value of α_i for this sample is 4±2 cm^{-1}. This value can be used to convert the spectra into modal absorption *A(hv)* and modal gain *G(hv)* spectra.

Several figures in chapters four and five will use the quasi-Fermi level separation (ΔE_f). This is assumed equal to the transparency energy, where the net modal gain = the internal losses as illustrated in Figure 3.11

3.52 Modifications to the Measurement Technique

For the structures examined in this thesis it is necessary to modify the net modal loss measurement to obtain the true modal absorption. The magnitude of the modal loss measured is decreased by carriers present in the dots, even though they are found within unpumped regions of the device [55].

There are two possible causes for the charge build up in the structures measured in this thesis; p-doping and photo-pumping of the passive section. The QDs can capture the additional holes provided by p-doping leaving fewer electrons available in the valence band to absorb incoming photons.

Photo-pumping can occur in any structure during an absorption experiment. Spontaneously emitted photons can be absorbed by electrons which occupy the valance band states in the passive (undriven) section. If these excited electrons are able to radiatively recombine before being removed electrically to ground, a fraction of the spontaneously emitted photons would couple into the optical mode and contribute to the measured emission from the driven section.

To modify the experiment a reverse bias is applied to the passive (undriven) section while the light is collected from the driven section. An illustration of the experimental setup is shown in Figure 3.12, in this case Section 2 is driven and Section 1 reverse biased.

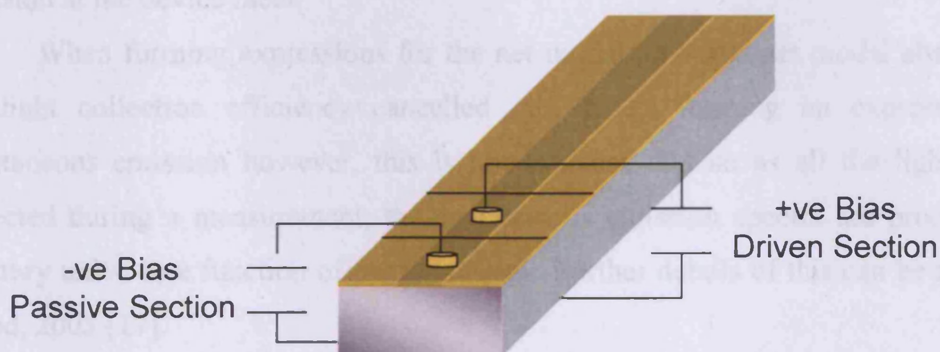

Figure 3.12 – Illustration of reverse bias applied to a multi-section device during a net modal loss measurement.

The reverse bias removes any build up of charge within the unpumped section leaving all the dot states available to take part in photon absorption. The magnitude of the reverse bias applied is increased until the magnitude of the modal absorption is maximised. It is important to ensure the magnitude of the reverse bias used is not causing band bending affects or the quantum confined stark effect, which might affect the results of the experiment. This is done by ensuring the absorption edge does not shift in energy which is usually a sign of these effects.

3.53 <u>Spontaneous Emission</u>

The SCM can be used to produce un-amplified spontaneous emission spectra. This is done by treating Equations 3.3 and 3.5 as simultaneous equations and solving for I_{sp}^{meas}.

$$I_{sp}^{meas} = \left[\frac{I_{ASE1}^{2}}{I_{ASE1,2} - 2I_{ASE1}}\right]\frac{1}{L}\ln\left[\frac{I_{ASE12}}{I_{ASE1}} - 1\right] \qquad \text{Equation 3.8}$$

Comparison between Equations 3.7 and 3.8 shows that the modal gain is used to compensate for the amplification experienced by the spontaneous emission, before emission at the device facet.

When forming expressions for the net modal gain and net modal absorption, the light collection efficiency cancelled out. When forming an expression for spontaneous emission however, this is not the case and so as all the light is not collected during a measurement, the spontaneous emission spectra are produced in arbitrary units, as a function of photon energy. Further details of this can be found in Blood, 2003 [17].

An example of a measured spontaneous emission spectrum formed from the ASE presented in Figure 3.10 is shown in Figure 3.13.

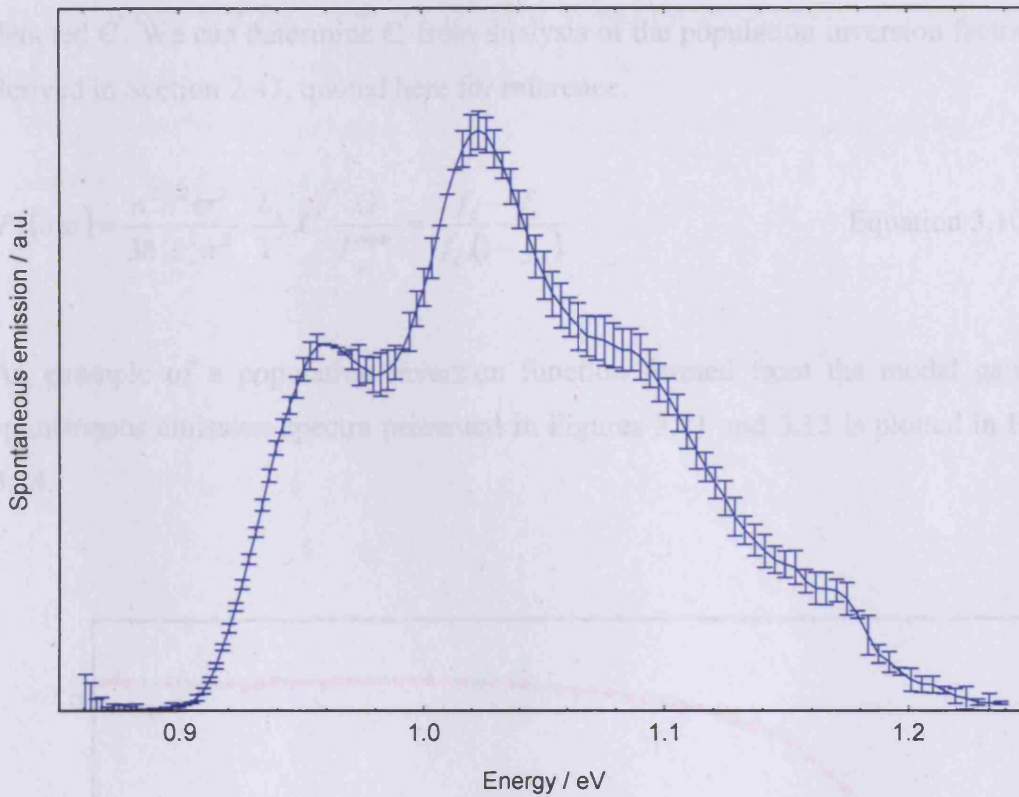

Figure 3.13 – Uncalibrated spontaneous emission plotted as a function of photon energy for a typical diode laser driven at 1111Acm^{-2}. The error bars are produced using the technique outlined in Section 3.6.

3.54 Calibration of the Spontaneous Emission and the P_f Function

Using the SCM it is possible to convert the measured spontaneous emission (I_{sp}^{meas}) into real units. I_{sp}^{meas} *is* related to the true spontaneous emission (I_{sp}) by Equation 3.09.

$$I_{sp}^{meas} = \beta C(1-R)I_{sp} \qquad \text{Equation 3.09}$$

β is the coupling coefficient of the spontaneous emission to the guided optical mode and *R* is the facet reflectivity factor. *C* is a calibration factor which takes account of the collection geometry of the measurement system.

This shows that $\beta C(1-R)$ is a linear scaling factor relating I_{sp}^{meas} and I_{sp} which is denoted C'. We can determine C' from analysis of the population inversion factor (P_f), derived in Section 2.43, quoted here for reference.

$$P_f(\hbar\varpi) = \frac{n^2\hbar^2\varpi^2}{3\hbar^3c^2\pi^2}\cdot\frac{L_z}{\Gamma}.C'\frac{G}{I_{sp}^{meas}} = \frac{f_c - f_v}{f_c.(1-f_v)}$$ Equation 3.10

An example of a population inversion function formed from the modal gain and spontaneous emission spectra presented in Figures 3.11 and 3.13 is plotted in Figure 3.14.

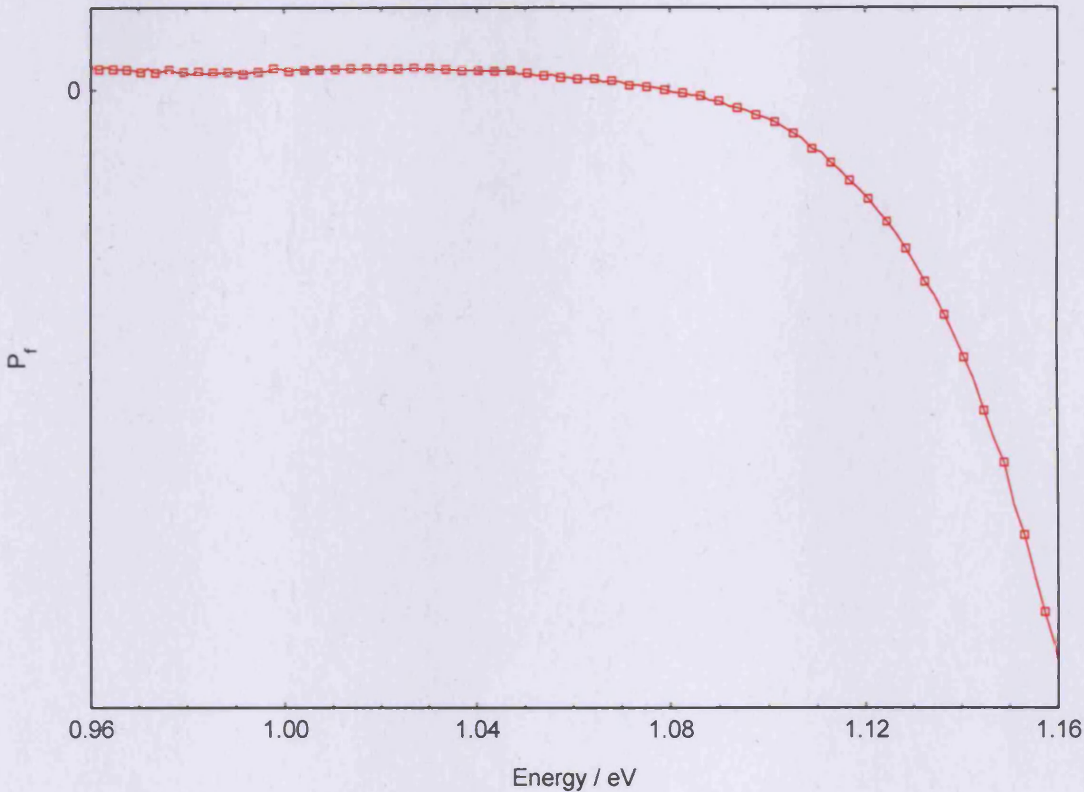

Figure 3.14 – Population inversion factor P_f plotted as a function of photon energy from a diode laser driven at 889Acm^{-2}.

From Equation 3.10, we note that when either $f_v = 0$ or $f_c = 1$, $P_f \rightarrow 1$. We identify a region on a plot of the experimentally measured P_f where saturation occurs, noting that in this region the true $P_f = 1$.

From comparison with Equation 3.10 we can extract a value for C' since all other parameters in Equation 3.10 are known. We can then use this to convert the measured spontaneous emission into real units by multiplying the intensity of the measured data by this factor.

3.6 Error Analysis of Data Extracted Using the Multi-Section Technique

To estimate the errors in the spectra of modal gain, modal absorption and spontaneous emission, the computer code running the long wavelength kit was modified by Dr D Palmer. For every wavelength step the computer samples and averages 40 data points. The modifications made to the code outputs the standard deviation of these 40 points along with the average at each wavelength step.

Using this data I have algebraically transformed the standard deviation for each wavelength step in the ASE into the standard deviation for each wavelength step in the various spectra produced. These values are plotted as error bars on certain spectra within this thesis.

3.7 Summary

In this chapter I have described the measurement techniques used for the work in Chapters four-six in this thesis. The majority of the work has been done using the segmented contact method which is used to produce modal absorption, modal gain, spontaneous emission and P_f spectra. I have also described how laser threshold and lasing wavelength measurements were performed.

4. Characterisation of a High Performance QD Laser Diode

4.1 Introduction

Quantum dot (QD) lasers have shown superior performance compared to quantum well (QW) lasers in many areas such as temperature independent threshold current and high differential gain [56]. They do however suffer from low modal gain as a result of low QD density, incomplete inversion of the dot lasing state [11] and inhomogeneous broadening.

Carrier occupation of the QD lasing state is affected by the close proximity of higher energy dot states and the large density of states (DOS) associated with the wetting layer [15]. This leads to temperature dependent gain saturation and the need for multiple layer structures. Structures which utilise a multilayer design can however suffer from defect formation and poor overlap between the QD layers and the optical mode. These problems have been largely overcome by the use of the high growth temperature spacer layer (HGTSL) design [57], and the use of thin spacer layers [58]. The highest reported modal gain per QD layer is 6.2cm^{-1} for a five layer structure, making the overall modal gain of 31cm^{-1} [59]. This value is comparable with that achieved in QW devices at this wavelength, such as the modal gain of 42cm^{-1} achieved at 1.2μm using the GaInNAs material system [60].

The energetic broadening of a quantum dot ensemble can be described by a Gaussian distribution when the inhomogeneous broadening is large compared to the homogeneous broadening The peak modal gain of the QD ensemble is reduced by the inhomogeneous energetic broadening *B(hv)*, caused by the stochastic size distribution [21].

$$B(E) = \frac{1}{\sqrt{2\pi}\sigma}\exp\left[-\frac{\left(E-\Delta E_f\right)^2}{2\sigma^2}\right]$$ Equation 5.1

ΔE_f is the quasi-Fermi level separation and σ is a broadening coefficient, which is related to the full width half maximum (FWHM) of the broadened transition by FWHM $= 2\sqrt{2\ln 2}\sigma$. The modal gain as a function of photon energy is directly proportional to this function. This shows that as the magnitude of the inhomogeneous broadening increases the peak modal gain decreases.

In this chapter I establish the properties of a high performance (HP) QD laser diode structure. These properties will be used for comparison with those of the tunnel injection structure described in Chapter five and to provide an understanding of the features observed in the population inversion spectra for this structure in Chapter six. I begin by discussing the growth and structural properties before showing the modal absorption, modal gain and spontaneous emission spectra, which I measured using the segmented contact method (SCM) [17].

4.2 Sample Growth and Structural Details

This structure was grown by solid source molecular beam epitaxy (MBE) on a 3″ n+ (001) GaAs substrate at the EPSRC National Centre for III-V Technologies in Sheffield. The active region consists of five dot in a well (DWELL) layers separated by a 50nm layer of GaAs. The DWELL consists of three monolayers of InAs dots grown on top of 2nm of $In_{0.15}Ga_{0.85}As$ and capped with 6nm of $In_{0.15}Ga_{0.85}As$, as illustrated in Figure 4.1. This structure is an example of the HGTSL design, referred to in Section 4.1. The 50nm GaAs spacer layer was grown in two stages; the first 15nm at 500°C and the final 35nm at 585°C.

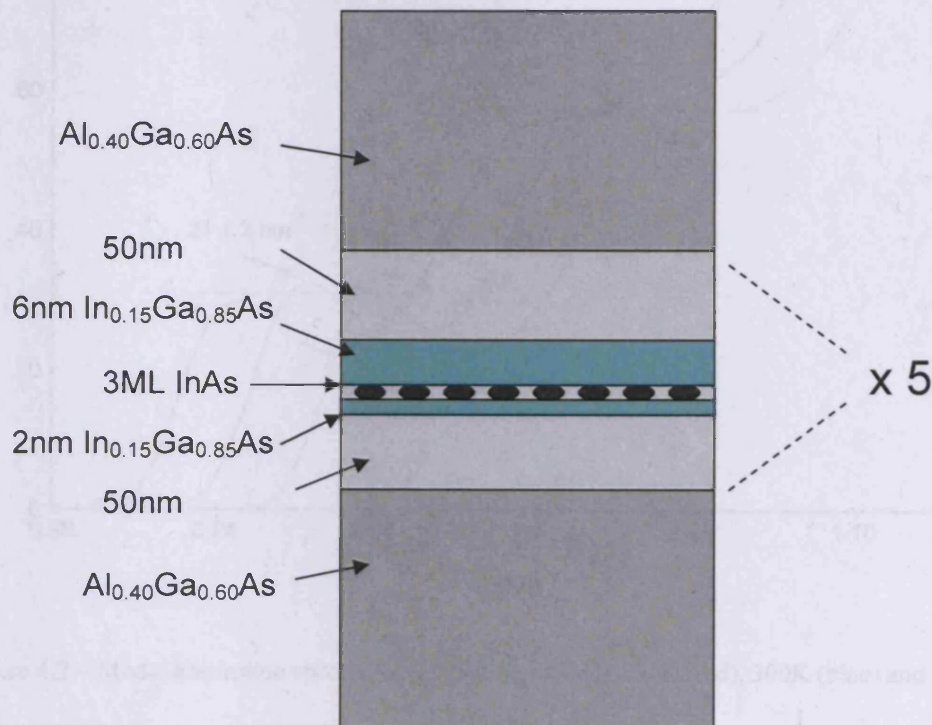

Figure 4.1 – Structural illustration of high performance QD sample

4.3 Measured Data

4.31 *Modal Absorption Measurements*

The net modal loss for the QD structure was measured from 250K to 350K using the SCM, outlined in Section 3.51. From these measurements the internal waveguide loss (α_i) was found to be 4±2cm^{-1}. This data was converted to the modal absorption data presented in Figure 4.2 by the addition of α_i and multiplying by -1.

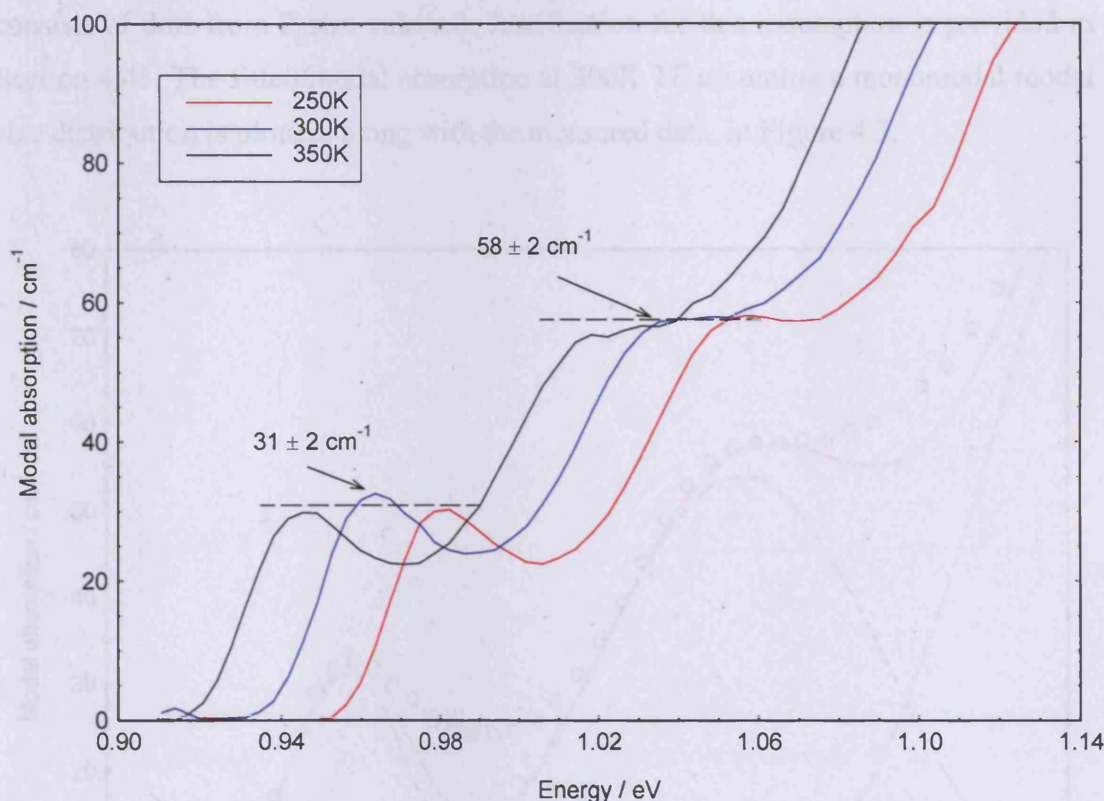

Figure 4.2 – Modal absorption spectra for a QD laser diode at 250K (red), 300K (blue) and 350K (black)

At all temperatures we can clearly resolve peaks from the inhomogeneously broadened QD ground and first excited state transitions. The peak modal absorption for the QD ground state is 31±2cm^{-1} and the peak modal absorption for the first excited state is 58±2cm^{-1}. The magnitude of α_i is independent of temperature over this range.

To further analyse the measured absorption data, the spectrum at 300K has been fitted with Gaussian curves. Each Gaussian represents a particular state within a dot ensemble and assumes a Gaussian distribution in the transition energy of the QD states. To achieve the fit, the spacing between the peak energies for the various QD states is assumed to be constant. The inhomogeneous broadening and Gaussian amplitudes are varied until a good agreement is achieved between the measured data and the fit are achieved.

A good agreement between the measured data and the fitted data could not be found assuming a monomodal dot size distribution within the ensemble, but an accurate fit was made assuming a bimodal dot size distribution (the dot ensemble consists of dots from 2 size subsets). Justification for this assumption is provided in Section 4.41. The fitted modal absorption at 300K TE assuming a monomodal modal size distribution is plotted, along with the measured data, in Figure 4.3,

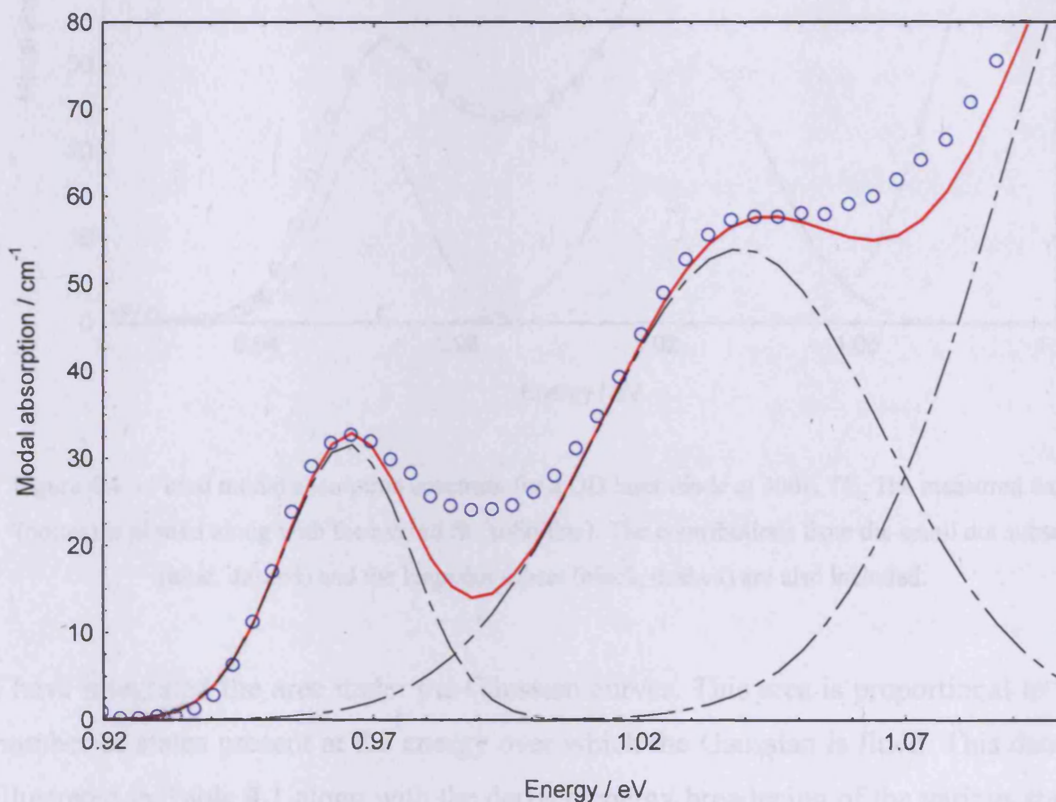

Figure 4.3 – Fitted modal absorption spectrum for a QD laser diode at 300K TE assuming a monomodal size distribution. The measured data (points) is plotted along with the overall fit (solid line) and the contributions of the various dot states (black).

The fitted modal absorption assuming a bimodal size distribution is plotted, along with the measured data, in Figure 4.4, where the peak energy separation of the fitted dot states is 67meV for both dot size subsets. The equality of the peak separation for both subsets is surprising, however it could be a result of the peak energies of the subsets being similar.

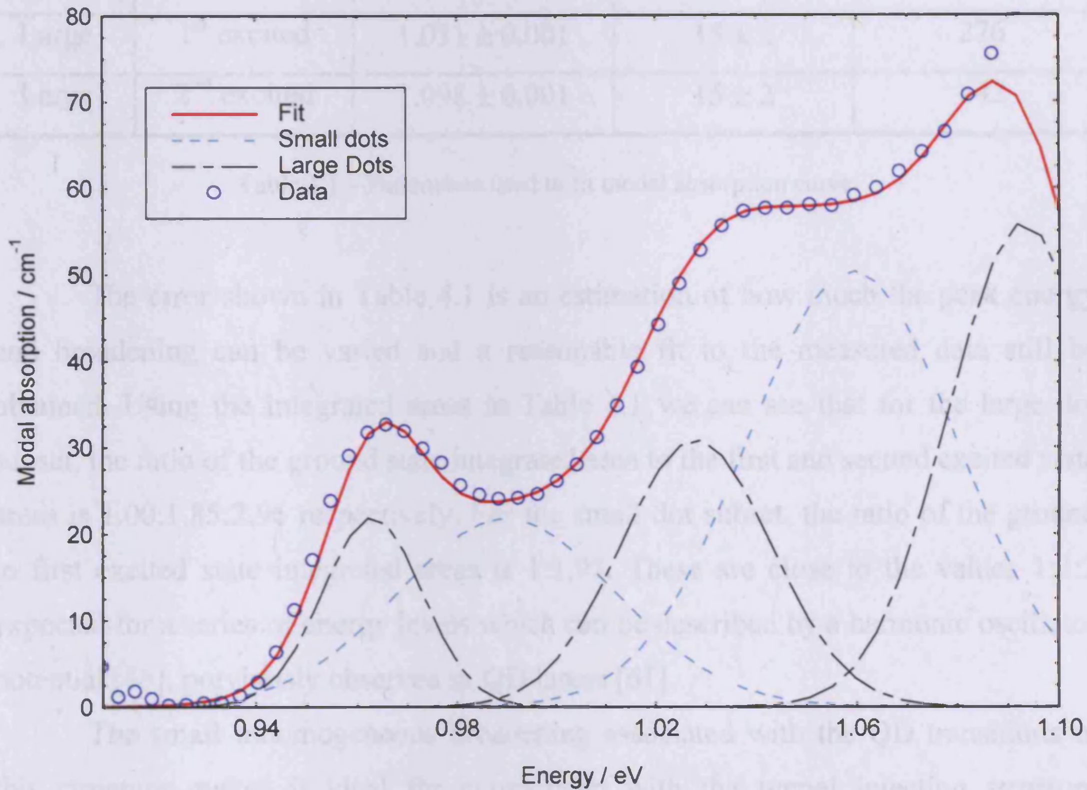

Figure 4.4 – Fitted modal absorption spectrum for a QD laser diode at 300K TE. The measured data (points) is plotted along with the overall fit (solid line). The contributions from the small dot subset (blue, dashed) and the large dot subset (black, dashed) are also included.

I have integrated the area under the Gaussian curves. This area is proportional to the number of states present at the energy over which the Gaussian is fitted. This data is illustrated in Table 4.1 along with the derived energy broadening of the various states and their peak energies.

Dot Size	State	Peak energy (eV)	Broadening (meV)	Area ($eVcm^{-1}$)
Small	Ground	0.995 ± 0.001	22 ± 2	308
Small	1st excited	1.062 ± 0.001	21 ± 2	594
Large	Ground	0.964 ± 0.001	12 ± 2	149
Large	1st excited	1.031 ± 0.001	15 ± 2	276
Large	2nd excited	1.098 ± 0.001	15 ± 2	442

Table 4.1 – Parameters used to fit modal absorption curve

The error shown in Table 4.1 is an estimation of how much the peak energy and broadening can be varied and a reasonable fit to the measured data still be obtained. Using the integrated areas in Table 4.1 we can see that for the large dot subset, the ratio of the ground state integrated area to the first and second excited state areas is 1.00:1.85:2.96 respectively. For the small dot subset, the ratio of the ground to first excited state integrated areas is 1:1.93. These are close to the values 1:2:3 expected for a series of energy levels which can be described by a harmonic oscillator potential [45], previously observed in QD lasers [61].

The small inhomogeneous broadening associated with the QD transitions in this structure makes it ideal for comparison with the tunnel injection structure characterised in Chapter five, with a similar amount of broadening.

Now that the QD states present in the structure have been revealed I will show further results produced using the SCM, where this time it was used to produce spontaneous emission spectra. From this data I analysed the radiative recombination properties of the structure under forward bias conditions.

4.32 Spontaneous Emission Measurements

Using the SCM I have produced spontaneous emission spectra, for a range of current densities, for the transverse electric (TE) polarisation, at 300K. This data shows the radiative recombination from the QD states under forward bias conditions as a function of photon energy, as shown in Figure 4.5

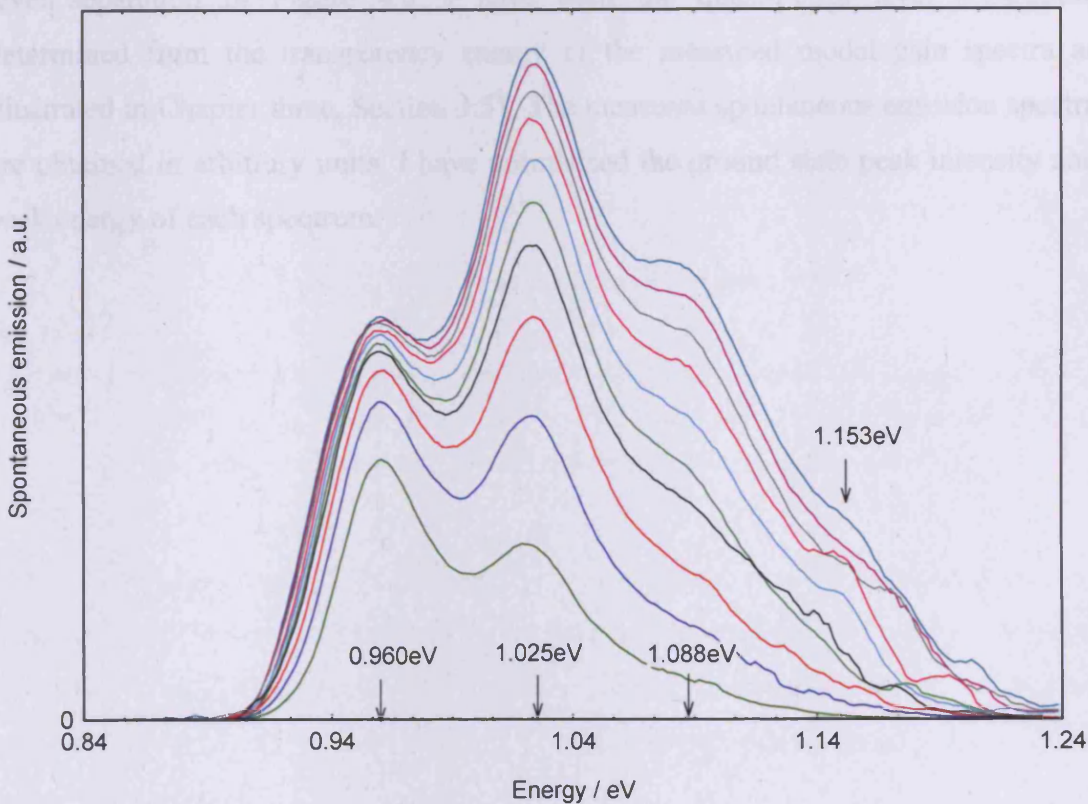

Figure 4.5 – Spontaneous emission spectra for a QD laser diode at 300K TE. The spectra correspond to drive current densities between $111Acm^{-2}$ and $1111Acm^{-2}$. The arrows represent the peak transition energies.

We can clearly observe emission from the inhomogeneously broadened QD ground (0.960eV), first excited (1.025eV) and second excited (1.088) states. The spacing of the dot states is approximately 65±2meV which agrees well with the data used to fit the modal absorption curve in Figure 4.4. This separation is typical of that seen in most dot systems, where the lasing wavelength is approximately 1.3μm [34,62,63].

The peak energy of the spontaneous emission does not change with increasing carrier density for the various dot states.

The spontaneous emission spectra have also been measured at temperatures between 200K at 350K. They all display similar characteristics to those seen in the 300K data; the peak energy of the spontaneous emission remains constant with increasing injection levels and recombination is observed from at least three QD states.

To highlight the change in occupation of the various dot states as a function of temperature, I have plotted the spontaneous emission spectra at fixed quasi-Fermi level separation in Figure 4.6. I have used the quasi-Fermi level separation, determined from the transparency energy of the measured modal gain spectra as illustrated in Chapter three, Section 3.51. The measured spontaneous emission spectra are obtained in arbitrary units, I have normalised the ground state peak intensity and peak energy of each spectrum.

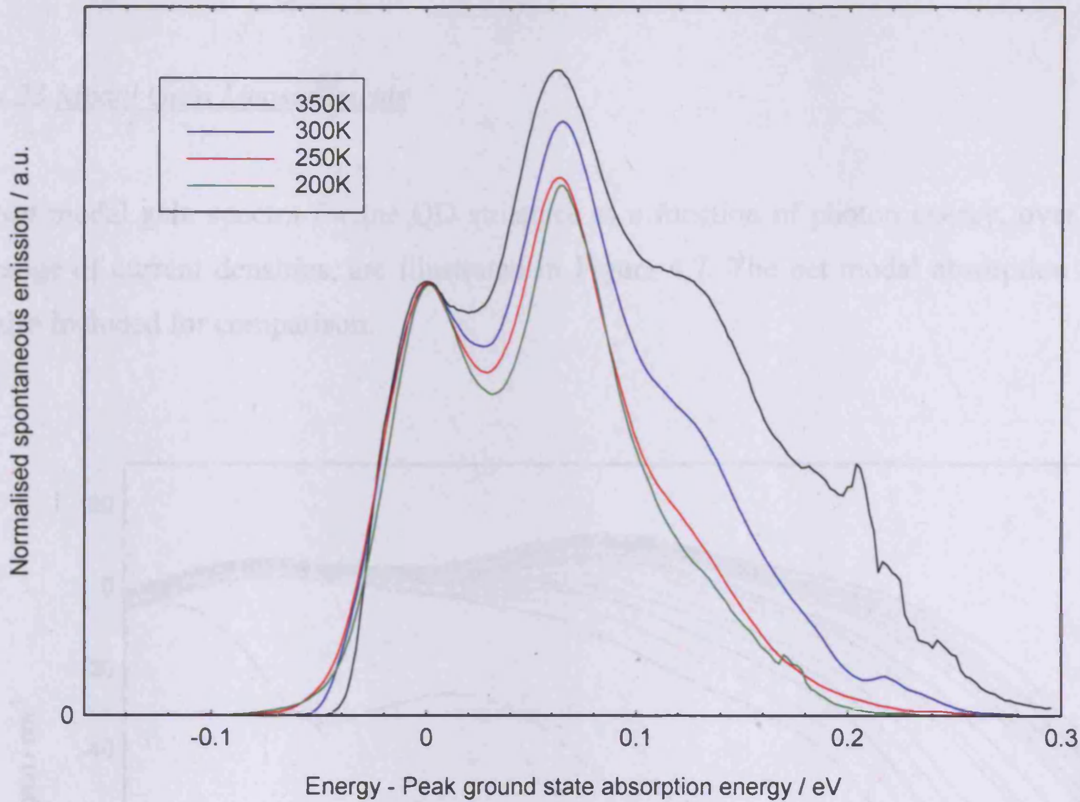

Figure 4.6 – Spontaneous emission at constant quasi-Fermi level separation for a Quantum dot laser diode at 350K TE at drive current densities between 111Acm^{-2} and 1111Acm^{-2}. The intensity and wavelength of each spectrum is normalised at the ground state transition.

The spectra show that as the temperature is increased, the population of carriers spreads out further in energy making recombination from higher energy dot states more prominent. The higher energy states such as the wetting layer cannot be resolved but this is probably due to very low light levels over this energy range decreasing the signal to noise ratio.

In the next section of this chapter I will show modal gain measurements taken on this QD structure using the SCM.

4.33 Modal Gain Measurements

Net modal gain spectra for the QD structure as a function of photon energy, over a range of current densities, are illustrated in Figure 4.7. The net modal absorption is also included for comparison.

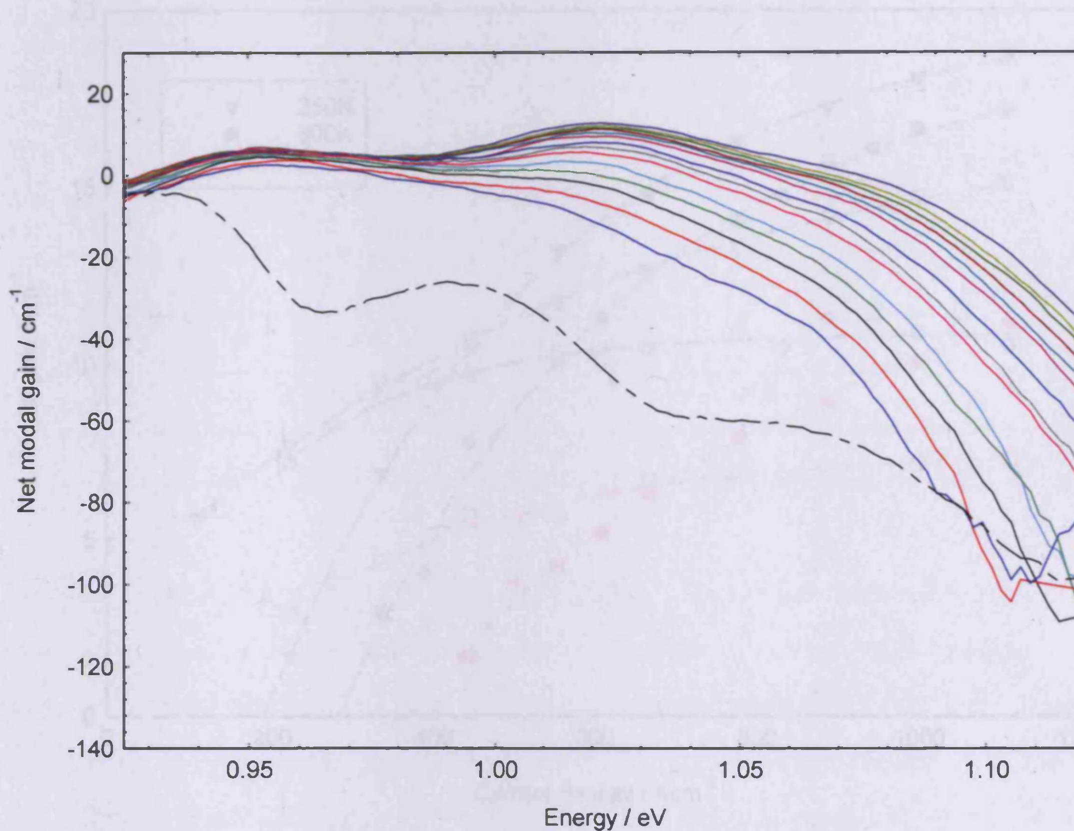

Figure 4.7 – Net modal gain spectra (solid lines) for a Quantum dot laser diode at 300K TE for drive current densities between 111Acm^{-2} and 1111Acm^{-2}. The net modal absorption is at 300K TE is also shown (Dashed line)

This shows that the ground state net modal gain saturates at approximately 7±2cm^{-1} which corresponds to a modal gain of 11 ± 2 cm^{-1}, when the internal waveguide loss (α_i = 4±2cm^{-1}) determined in Section 4.31, is taken into account. The errors are estimated from the uncertainty in the peak saturation and the internal waveguide loss. They all have equal value as these errors are related quantities.

We can further analyse the modal gain by plotting the peak modal gain of the QD ground (open symbols) and first excited (closed symbols) states, as a function of injection current density. This is shown in Figure 4.8 along with the data at 250K and 350K for comparison.

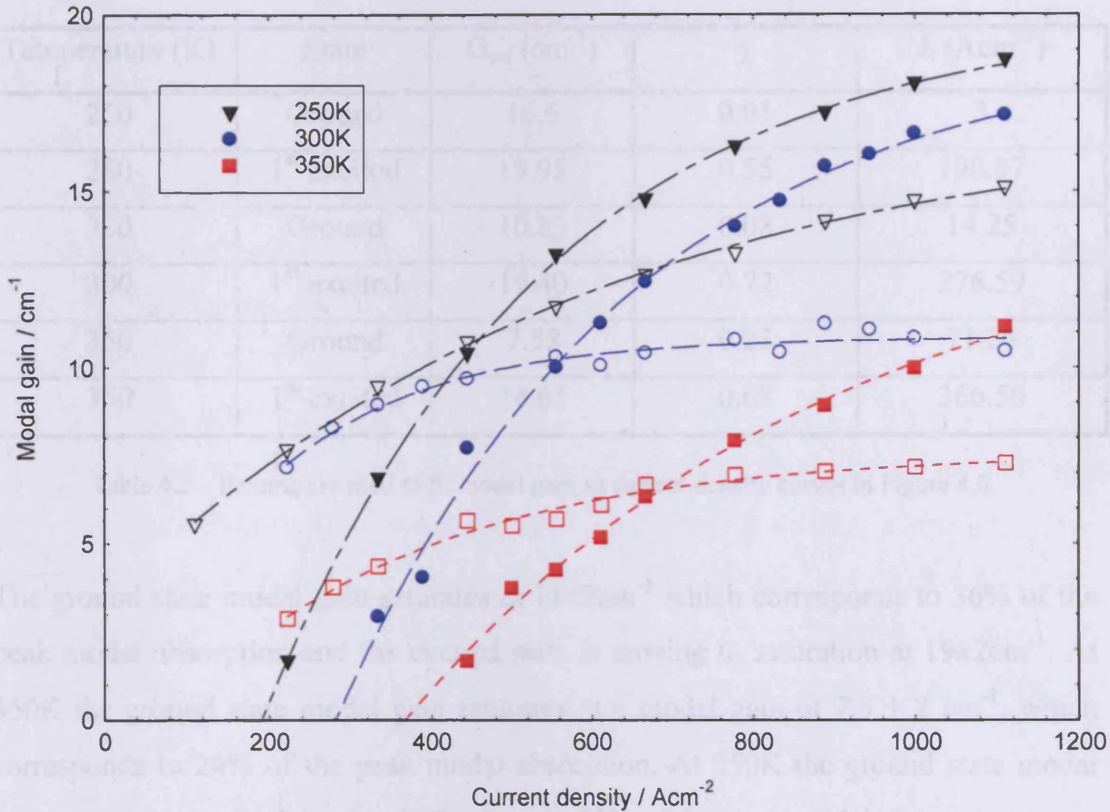

Figure 4.8 – Modal gain spectra vs injection current density for a QD laser diode at 250K (black) 300K (Blue) and 350K (red). Open symbols refer to the modal gain at the ground state lasing wavelength and closed symbols correspond to the modal gain at the first excited state lasing wavelength.

The dashed lines are fitted using the expression introduced in Section 2.6, repeated here for clarity:

$$G = G_{sat}\left(1 - \exp^{-\gamma\frac{(J - J_t)}{J_t}}\right) \qquad \text{Equation 3.1}$$

G_{sat} is the saturated modal gain, J_t is the transparency current density (G=0) and γ is a dimensionless, non-ideality factor [20]. This equation has been shown [48] to fit experimentally determined QD gain-current curves when they are affected by higher energy dot states and inhomogeneous broadening. The parameters used to fit the modal gain vs current curves in Figure 4.8 are shown in Table 4.2.

Temperature (K)	State	G_{sat} (cm^{-1})	γ	J_t (Acm^{-2})
250	Ground	16.6	0.01	3
250	1st excited	19.95	0.55	190.87
300	Ground	10.83	0.08	14.25
300	1st excited	19.40	0.72	276.59
350	Ground	7.55	0.23	71.25
350	1st excited	14.61	0.68	366.50

Table 4.2 – Parameters used to fit modal gain vs current density curves in Figure 4.8.

The ground state modal gain saturates at 11±2cm^{-1} which corresponds to 36% of the peak modal absorption and the excited state is moving to saturation at 19±2cm^{-1}. At 350K the ground state modal gain saturates at a modal gain of 7.5 ± 2 cm^{-1}, which corresponds to 24% of the peak modal absorption. At 250K the ground state modal gain saturates at a modal gain of 17 ± 2 cm^{-1}, 55% of the peak modal absorption so we can clearly see that the gain saturation effects increase with increasing temperature.

4.4 Interpretation and Discussion of Results

In this Section I discuss the measured data shown in Section 4.3 and provide explanations for the observed characteristics.

4.41 *Modal Absorption*

The measured modal absorption spectra between 250K and 350K (Figure 4.2) showed two distinct peaks which are attributed to the QD ground and first excited transitions. The peak ground state absorption shows small ($< 2cm^{-1}$) variations with temperature. Both the number of states present in the structure and the inhomogeneous broadening do not change with temperature, which suggests the small variations in the peak ground state modal absorption must be due to a measurement inaccuracy. This assumes the variation in homogenous broadening is not significant over this temperature range.

At temperatures lower than this I observed the magnitude of the ground state peak absorption measured is dependent on the drive current density. This effect could be caused by photo-pumping effects during the measurement. Photo-pumping is more likely as there is no P-doping incorporated into the active region of this structure. This is caused by spontaneously emitted carriers from the pumped section, being absorbed by the passive absorption section before being reemitted into optical mode and collected as ASE. This effect can usually be removed by applying a reverse bias to the passive section, however as this effect appears negligible over the temperature range shown in Figure 4.2 it is not considered further.

The peak modal absorption for the ground and first excited transitions is measured to be 31 ± 2 cm^{-1} and 58 ± 2 cm^{-1} respectively. This is close to the ratio 1:2 expected due to the double degeneracy of the first excited state. However it is strictly the area of the transition peaks and not the magnitude of the peak that reflects the degeneracy of 1:2. This degeneracy applies to a series of energy levels described by a harmonic oscillator potential [45].

The area of the various transitions, as well as the inhomogeneous broadening associated with them, was investigated by fitting the modal absorption curve at 300K with a series of Gaussians (Figure 4.4). Each Gaussian corresponds to a particular transition and the fitting assumes that a Gaussian distribution in energy is present for the various dot states.

Pask (2006) [64] theoretically formed an absorption curve from an ensemble which contained a Gaussian distribution of dot sizes. It was shown that in this case a fit assuming a Gaussian distribution in transition energy could not be applied to the theoretically generated data.

In the measured absorption spectrum fitted in this work, a Gaussian distribution in energy approximates well to the measured data. This suggests that in this case the assumption of a Gaussian distribution in energy is appropriate.

Another assumption which had to be made to achieve a fit was that a bimodal population in dot sizes is present in the ensemble. This assumption is supported by previous AFM studies performed on this material by Liu et al. (2004) [65]. This work showed two dot subsets, where both dot populations had a density of approximately 2×10^{10} cm^{-2}. Evidence for the existence of bimodal size distributions in self-assembled QD lasers has also been found in many other structures [13, 66-68].

The ratio of the ground state integrated area to the first excited and second excited states for the large dot subset was found to be 1.00:1.85:2.96. For the small dot subset the ratio of the ground state integrated area to the first excited state area was 1:1.93, as expected due the degeneracy of the dot states. A difference in the number of states for each dot subset was observed which could indicate a difference in dot density between these subsets. However this was not revealed during the AFM studies described earlier. It should be noted the AFM studies may not reflect the true dot densities, as they are taken on uncapped dots and so the dots measured using the SCM may differ in size and composition.

The inhomogeneous broadening was found to be 12±2 meV for the large dot subset and 22±2 meV for the small dot subset. This work has also revealed the peak position of the various dot states which will be used to interpret the carrier distribution data shown in Chapter six.

4.42 *Spontaneous Emission*

The spontaneous emission spectra at 300K TE for a range of drive current densities was shown in Figure 4.5. We observed significant recombination from the inhomogeneously broadened QD ground, first excited and second excited states and a small amount of recombination from the QD third excited state.

The peak energy of the spontaneous emission does not change with increasing carrier density for the various dot states. The shift usually observed in peak energy with increasing current density, is caused by state filling effects. The lack of such a shift is indicative of a system where the carriers are not distributed according to Fermi-Dirac statistics (thermally distributed). This effect has previously been observed in other dot systems where it was attributed to carrier capture in to the various dot states with no subsequent redistribution between these states [11].

Another possible explanation is that we may have to measure the spontaneous emission spectra at very low current densities to observe a shift, even where a Fermi-Dirac distribution is present. This is illustrated Figure 4.9, where the spontaneous emission spectra for a GaInNAs quantum well sample I have previously tested using the SCM is plotted. Structural details for this can be found in the publication by Wang et al. 2004 [69].

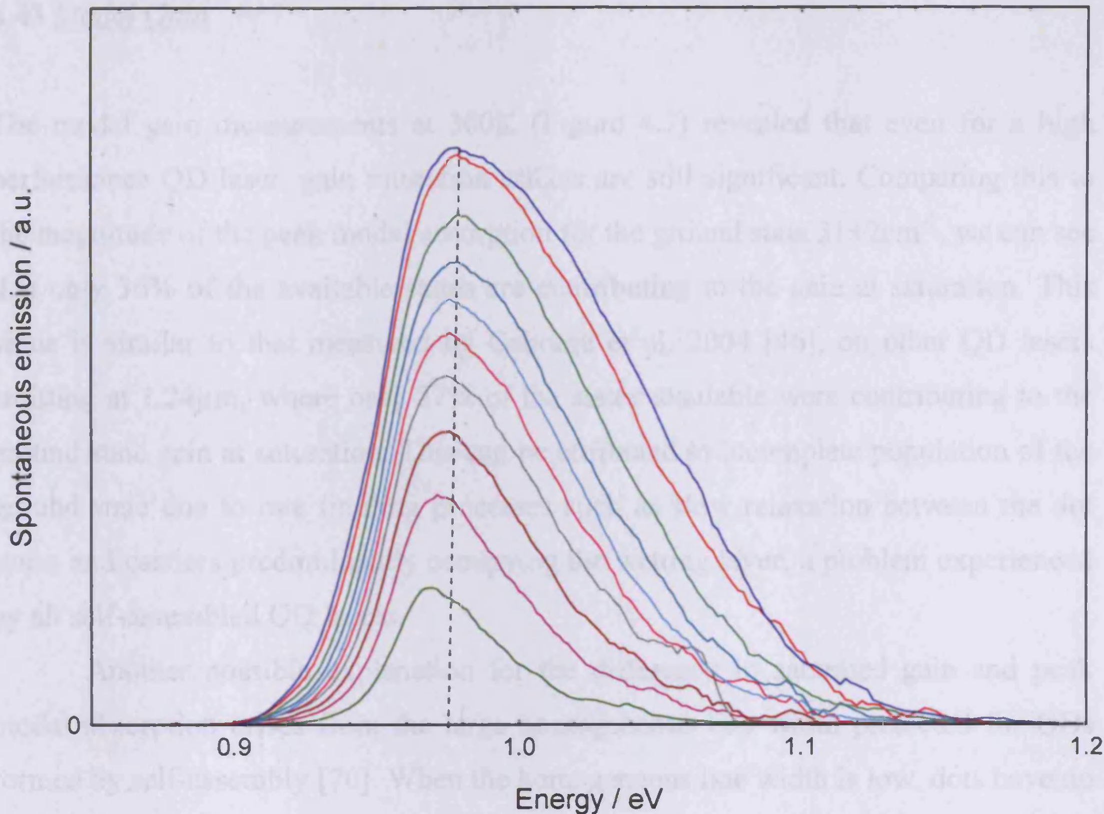

Figure 4.9 – Spontaneous emission spectra for a GaInNAs quantum well sample measured at 300K TE at drive current densities between 111 and 1111Acm^{-2}.

At low current densities there is a significant shift in peak energy but this shift soon becomes negligible at the current injection level is raised.

The spontaneous emission was also analysed between 200K and 350K and compared in Figure 4.6. This showed that for an equivalent quasi-Fermi level separation, as the temperature is increased, the population of carriers spreads out further in energy making recombination from higher energy dot states more prominent.

4.43 *Modal Gain*

The modal gain measurements at 300K (Figure 4.7) revealed that even for a high performance QD laser, gain saturation effects are still significant. Comparing this to the magnitude of the peak modal absorption for the ground state $31\pm2cm^{-1}$, we can see that only 36% of the available states are contributing to the gain at saturation. This value is similar to that measured by Osborne et al. 2004 [46], on other QD lasers emitting at 1.24μm, where only 27% of the states available were contributing to the ground state gain at saturation. This can be attributed to incomplete population of the ground state due to rate limiting processes such as slow relaxation between the dot states and carriers predominantly occupying the wetting layer, a problem experienced by all self-assembled QD lasers.

Another possible explanation for the difference in saturated gain and peak modal absorption arises from the large homogeneous line width predicted for QDs formed by self-assembly [70]. When the homogeneous line width is low, dots have no correlation to each other as they are spatially isolated. When the homogeneous line width becomes comparable with the inhomogeneous line width, lasing-mode photons receive gain not only from energetically resonant dots but also from other non-resonant dots that lie within the amount of homogeneous broadening leading to gain saturation without full inversion. This is however not the cause of the gain saturation observed in this structures as the broadening observed in the spontaneous emission spectra and absorption spectra are comparable, which is not consistent with the homogeneous broadening model.

In Figure 4.8 I plotted the peak modal gain vs injection current density for the QD ground and first excited states at 250K, 300K and 350K. This clearly showed that gain saturation effects increase with increasing temperature.

This agrees well with the results found by Smowton et al. 2004 [71], who attribute this behaviour to the carrier occupation of the wetting layer increasing with increasing temperature. This leaves fewer available carriers to occupy the QD ground state and so complete inversion cannot be attained. They also found that at 100K complete inversion was obtained due to the decoupling of the wetting layer and dot states. In Figure 4.10 I have re-plotted the Modal gain vs current density data, for the ground state transition, with the addition of data at 100K and 200K.

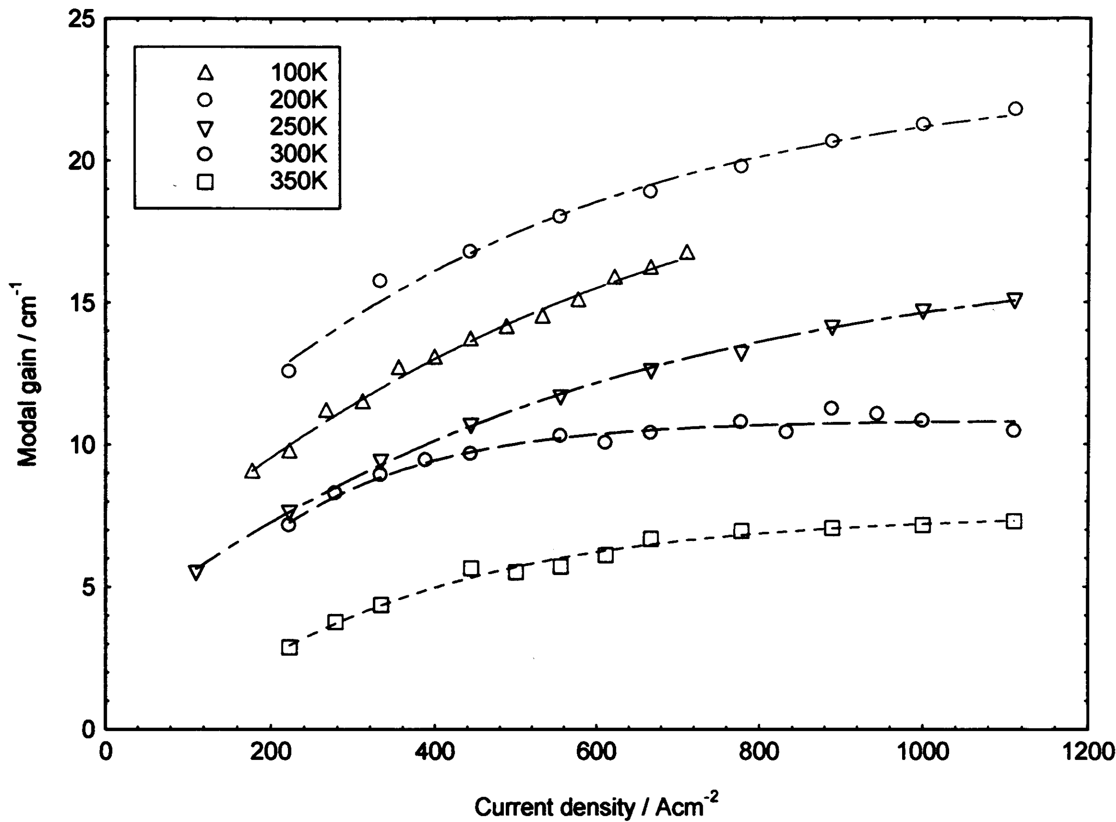

Figure 4.10 – Modal gain spectra Vs injection current density for the ground state of a QD laser diode at 100K(pink), 200K(green), 250K (black) 300K (Blue) and 350K (red).

In contrast to what was found by Smowton et al [71], we see in Figure 4.10 that the 100K ground state modal gain saturates at a lower value than that attained at 200K. This can be explained if we consider that, within this QD structure, we have a bimodal dot size distribution. When the wetting layer and dot states are decoupled at 100K, carriers captured by the dots can no longer redistribute themselves to more favourable states via the wetting layer. In this situation, only dots which contain both an electron and a hole will contribute to the modal gain leading to an overall reduction in the saturated value.

4.5 Conclusion

In this chapter I have established the properties of a high performance QD laser diode for comparison with those of the tunnel injection structure described in Chapter five and to provide an understanding of the carrier distribution observed in Chapter six. I have shown that a bimodal population in dot sizes existed in this structure and revealed the temperature dependence of its characteristics, particularly gain saturation.

5. Characterisation of a QD Laser Diode Incorporating Tunnel Injection.

5.1 Introduction

Lasers containing self-assembled quantum dots (QDs) have been developed rapidly to display lower threshold current densities, reduced temperature sensitivity and other improved characteristics compared to quantum well (QW) devices. They have not however, reached their theoretically predicted "ideal" characteristics [7,8], which were described in Chapter two of this thesis.

There are several proposed reasons for their performance limitation, which include: variations in dot properties throughout the ensemble and reduced carrier population of the lasing state. The variation of dot properties is an inherent problem caused by the self-assembly process itself, and can only be addressed through new growth techniques. The reduced population of the dot lasing state has previously been attributed to carrier occupation of the wetting layer [11] and slow relaxation between intra dot states [16].

The wetting layer has a large, two dimensional density states density of states (DOS), through which electrically injected carriers travel before relaxing into the lower energy dot states. With the exception of very low temperatures, the wetting layer states form a thermally coupled system with the dot states [11,15,16]. This is achieved by the thermalisation, and subsequent relaxation, of carriers between the dot states and the wetting layer and hence, the thermal coupling provides a means by which the thermal redistribution of carriers throughout the ensemble can be achieved.

Matthews et al. (2002) [11], showed the density of two-dimensional states in the wetting layer can be up to two orders of magnitude greater than the density of states of the QDs. The large DOS associated with the wetting layer leads to carriers predominantly occupying the wetting layer states and can cause gain saturation. This means that there are insufficient carriers supplied to fill the dot states and the peak modal gain achieved is lower than would be achieved if the states were fully inverted.

Fiore et al. 2007 [16] , describes a model of a quantum dot ensemble in which the relaxation rates between the wetting layer and dots are examined, then compared with the relaxation rate between the dot first excited and ground state. This model attributes the main rate limiting process for carriers relaxing to the lasing state to slow relaxation between the lower energy dot states.

The performance limitations described above are caused by carriers passing through higher energy states before relaxing into the QD lasing state. A proposed solution to these problems is to use a tunnelling injection structure whereby the electrons are introduced into the lower energy dot states by tunnelling from an adjacent injector QW [15]. An illustration of the electron injection process is shown in Figure 5.1. In this case the tunnelling is not a direct transition and requires the emission of a longitudinal optical (LO) phonon for energy conservation. This is a consequence of the materials required to form the injector well and QD layers which are designed for telecommunications applications.

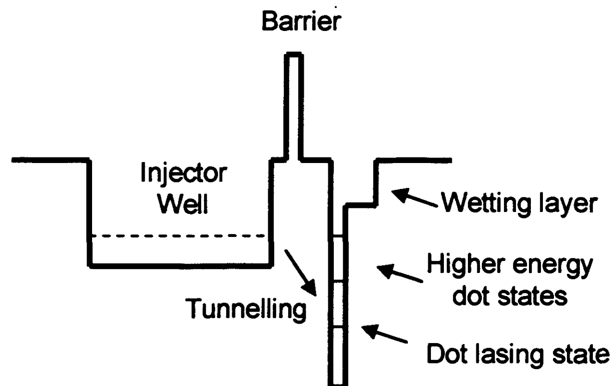

Figure 5.1 – Illustration of the phonon assisted tunnel injection process.

Under ideal operation, the injected carriers bypass the wetting layer and higher energy dot states. The tunnelling injection structure has previously been used to reduce "hot carrier" effects in QW structures [72] and QD structures with an operating wavelength of 1.1μm [73]. Unlike these previous structures, the tunnel injection structure investigated in this work has a lasing wavelength of 1.24μm. To ease the alloying requirements of the injector well, the phonon assisted tunnelling process injects the electrons into the QD first excited state.

Previous studies of carrier dynamics in these tunnel injection InGaAs/GaAs QD lasers have demonstrated significant improvements in performance, including increased small signal modulation bandwidth and reduced temperature dependence of threshold current [73].

In this chapter I use the segmented contact method (SCM) to produce modal absorption, modal gain and spontaneous emission spectra for the tunnel injection structure. From this I will determine which QD states are present in the structure, the state(s) the tunnelling process operates between, the modal gain characteristics of the structure and explore the efficiency of the tunnelling process as the operating temperature is varied. I will use edge photo-voltage absorption spectroscopy (EPVS) to reveal the energy separation of the transition states within the structure. I will also compare the characteristics of this structure with those of the high performance conventional QD structure described in Chapter four.

5.2 Sample Growth and Structural Details

The device heterostructure was grown at the University of Michigan by molecular beam epitaxy. It was grown on a (001) GaAs substrate and its structure is illustrated in Figure 5.2.

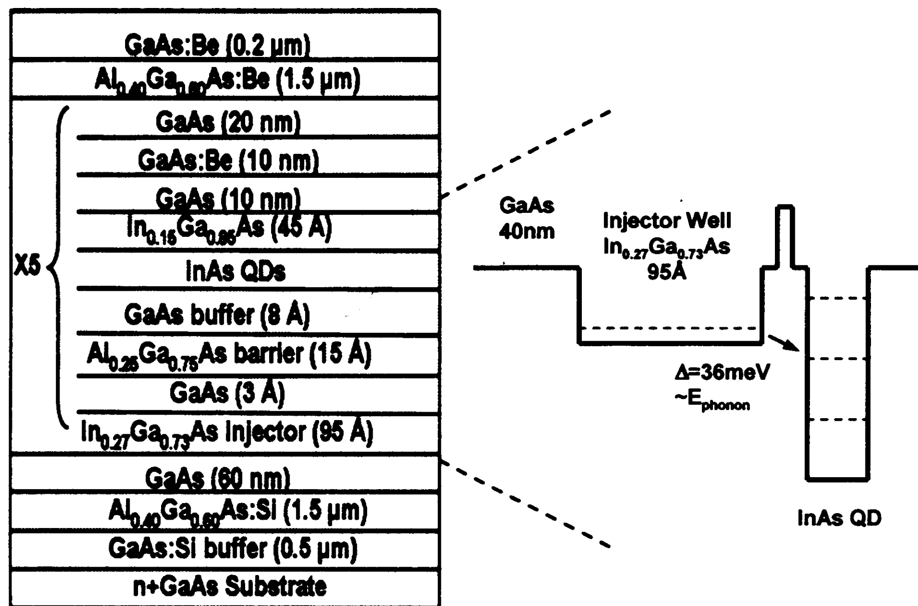

Figure 5.2 – Structural illustration of tunnel injection device.

The structure consists of five repeat InAs QD layers, each with a coupled $In_{0.27}Ga_{0.73}As$ injector well, separated by an $Al_{0.25}Ga_{0.75}As$ barrier. The injector well was grown at 450°C and the QD layers at 510°C .The structure was designed so that the ground state of the injector well is separated from the dot first excited state by the energy of a LO phonon, approximately 36meV. Carriers injected into this state then relax to the lasing state.

This structure incorporates P-doping where the GaAs waveguide, which was grown above the dot, was doped with Beryllium. The doping level was nominally 20 atoms per dot. The doping provides the holes for the injected electrons to recombine with hence hole tunnelling is not required. Further details of design and growth can be found in the publication by Mi et al, 2005 [74].

To help interpret the features observed in the EPVS absorption spectrum in Section 5.3 I have modelled the states present within the injector well using the approach of Blood (2005) [75]. The energy levels present within the QD ensemble cannot be modelled in this way because the size, shape and composition of the dots within the ensemble are not known.

In this simplistic model of the well I assume that the barriers of the well are thick and consist entirely of GaAs. I also assume that the effects of the closely spaced QD layer and the barriers do not significantly change the position of the energy levels found. The effective masses in the barrier (m_b^*) and well (m_w^*) along with the band offsets used can be found in Vurgaftman et al. (2001) [30] and the energy levels in the z direction (E_z) were found by solving Schrödinger's equation for a standing wave localised within the well of width L_z and depth V_0, with an evanescent decay in the barrier. The simultaneous equations formed are:

$$\frac{m_w^*}{m_b^*}\frac{L_z}{2}k_b = \left(\frac{L_z}{2}\sqrt{\frac{2m_w^*E_z}{\hbar^2}}\right)\tan\left(\frac{L_z}{2}\sqrt{\frac{2m_w^*E_z}{\hbar^2}}\right) \qquad \text{Equation 5.1}$$

$$\frac{m_w^*}{m_b^*}\frac{L_z}{2}k_b = \sqrt{\left[\left(\frac{m_w^*V_0L_z^2}{2\hbar^2}\right)-\left(\frac{L_z}{2}\sqrt{\frac{2m_w^*E_z}{\hbar^2}}\right)^2\right]\cdot\frac{m_w^*}{m_b^*}} \qquad \text{Equation 5.2}$$

Where k_b is the wave vector within the barrier. Solutions to these equations are found graphically and are shown in Figure 5.3.

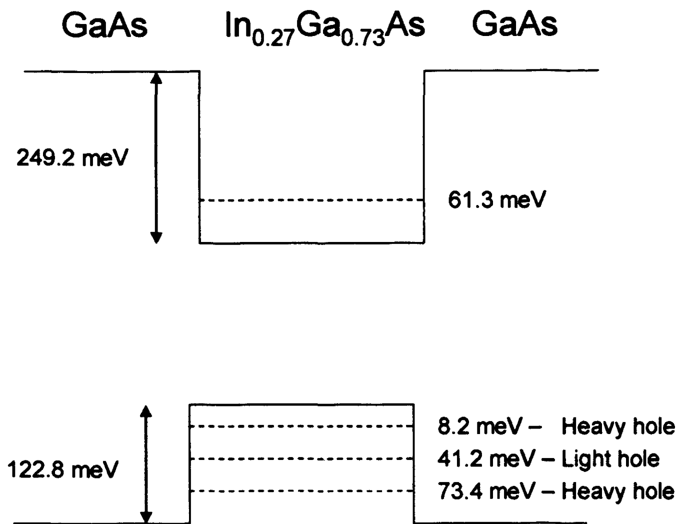

Figure 5.3 – Confined states present within the injector well

There is a single electron state (61.3meV) present. Due to selection rules we should only observe recombination between this state and the heavy hole state (8.2meV) and between the electron state with the light hole state (41.2meV).

5.3 Measured Data

In this section I show the measured data from the characterisation of the tunnel injection QD structure. Conclusions drawn from these measurements will be presented in Section 5.4.

5.31 Edge Photo-Voltage Spectroscopy Measurements

The various transitions which are present in the structure and their energy separation have been measured using polarisation sensitive, EPVS [76] at room temperature. The measured data are shown in Fig. 5.3.

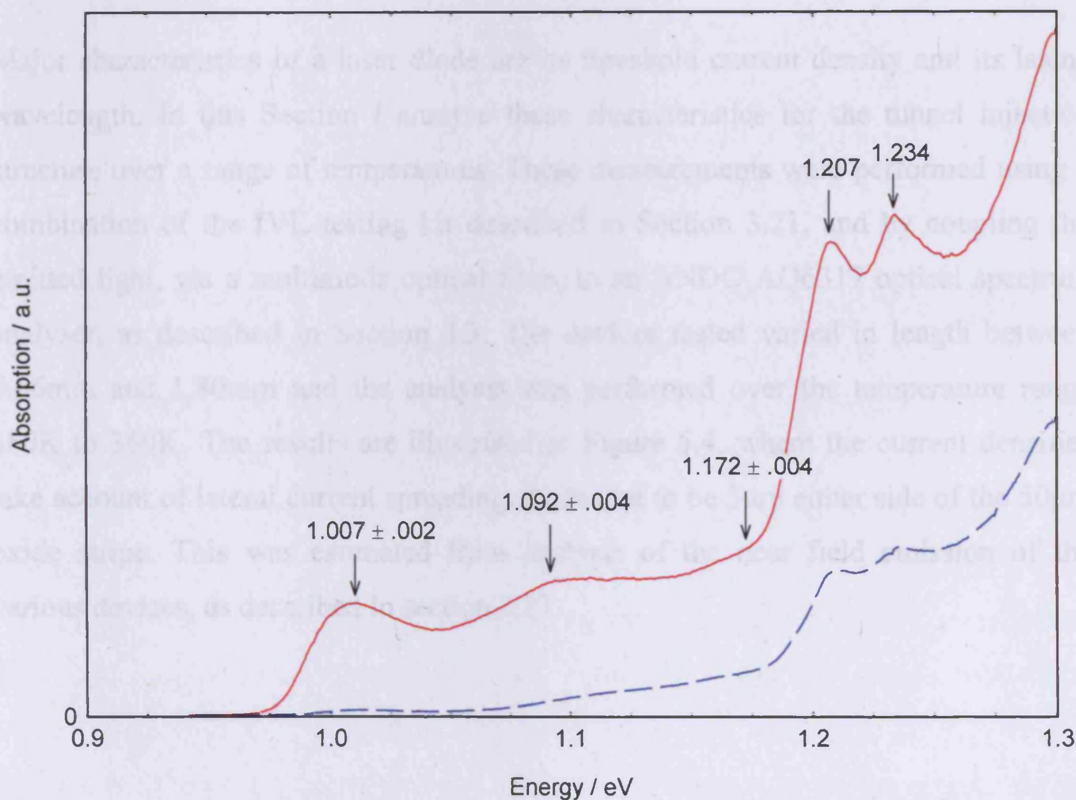

Figure 5.3 – Photo-voltage absorption spectra for the tunnel injection structure at room temperature in TE (red, solid line) and TM (blue, dashed line) polarisations.

The transverse electric (TE) polarisation spectrum (solid line) shows the inhomogeneously broadened dot ground (1.007eV) and first excited (1.092eV) state transition peaks, separated by approximately 85±4meV. A small feature is observed, only in the TE polarisation, which could be attributed to the QD second excited state transition (1.172), however the close proximity of the injector well makes the peak energy difficult to identify. We observe two sharp peaks at higher energy in both the TE and TM spectra. These are attributed to heavy hole (1.207eV) and light hole (1.233eV) transitions in the injector well from comparison with the model of the injector well states shown in Section 5.2.

For measurements taken with transverse magnetic (TM) polarisation (dashed line) there is no significant absorption from the dot states.

5.32 Laser Threshold and Temperature Stability

Major characteristics of a laser diode are its threshold current density and its lasing wavelength. In this Section I analyse these characteristics for the tunnel injection structure over a range of temperatures. These measurements were performed using a combination of the IVL testing kit described in Section 3.21, and by coupling the emitted light, via a multimode optical fibre, to an ANDO AQ6317 optical spectrum analyser, as described in Section 3.3. The devices tested varied in length between 0.66mm and 1.80mm and the analysis was performed over the temperature range 180K to 360K. The results are illustrated in Figure 5.4, where the current densities take account of lateral current spreading, estimated to be 5μm either side of the 50μm oxide stripe. This was estimated from analysis of the near field emission of the various devices, as described in section 3.23.

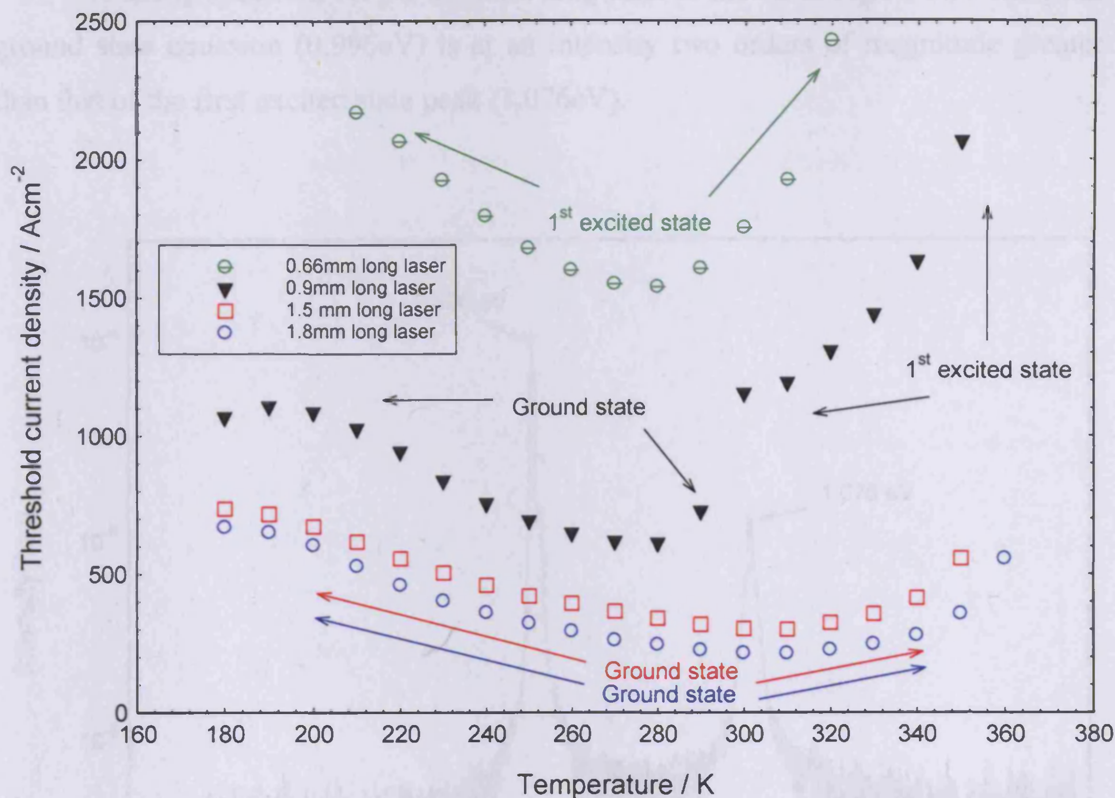

Figure 5.4 – Laser threshold current density as a function of temperature for lasers of length 0.66mm (green, circle), 0.90mm (black, triangle), 1.50mm (red, square) and 1.80mm (blue, circle).

The results show that for the 1.8mm long laser, over an operating temperature range of 290K to 350K, the threshold current density varies from 213Acm^{-2} to 356Acm^{-2}. Similar behaviour is observed for the 1.5mm long laser. It can also be seen the threshold current does not vary more that a factor of two over the entire temperature range tested and lasing always occurs on the ground state (0.996eV at 300K).

For the 0.66mm long laser, the threshold current is highly temperature dependent. Lasing is only observed between 210K and 320K and is always on the first excited state (1.076eV at 300K). The most interesting behaviour is seen in the 0.90mm long laser. At temperatures ≤ 290K lasing occurs at an energy corresponding to the ground state. At temperatures ≥ 310K lasing occurs at an energy corresponding to the first excited state and at 300K two-state lasing is observed, where both the ground and first excited states appear to lase simultaneously.

A lasing spectrum for the 0.90mm long laser is shown in Figure 5.5. The peak ground state emission (0.996eV) is at an intensity two orders of magnitude greater than that of the first excited state peak (1.076eV).

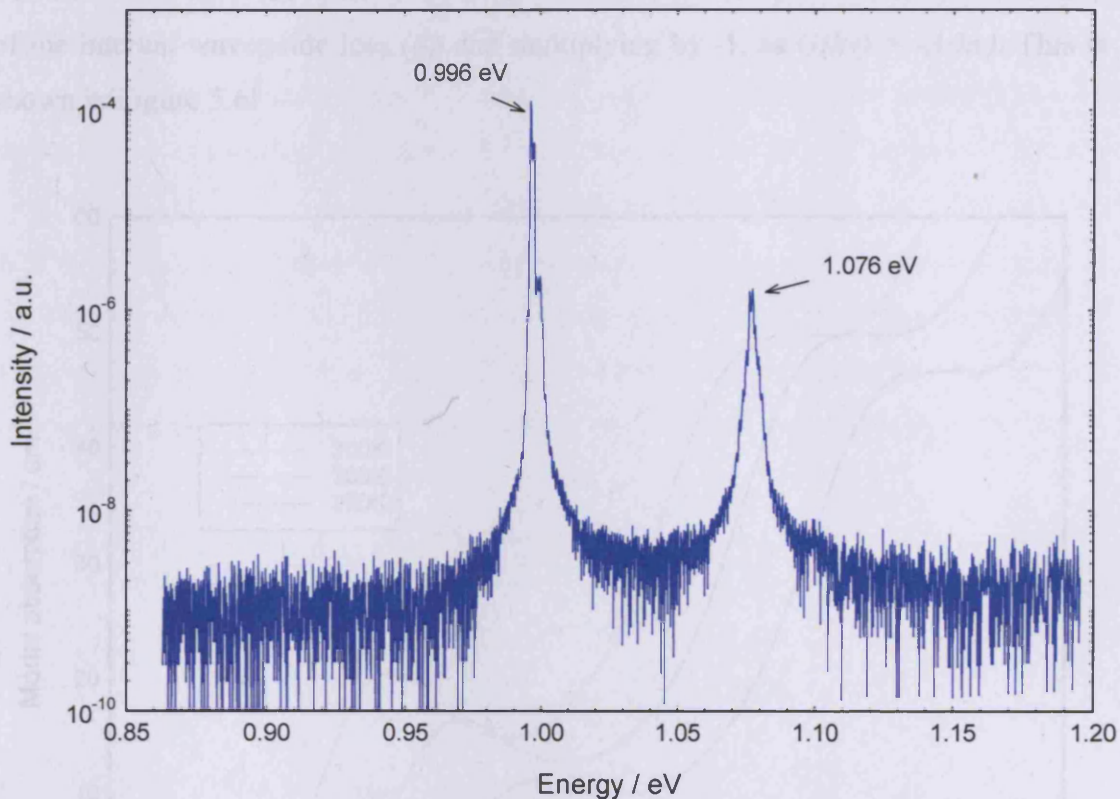

Figure 5.5 – Lasing spectrum for a 0.90mm long laser at 300K. The device was driven at 1250Acm^{-2} with 5kHz repetition rate using a 500ns pulse width.

I have so far analysed the various energy states present in the structure using EPVS measurements and looked at the lasing behaviour of the tunnel injection devices. In the next section I will begin the full characterisation of this structure using the SCM.

5.33 Modal Absorption Measurements

The net modal loss has been measured as a function of temperature using the SCM [17]. From this, the internal waveguide loss α_i was measured to be 4±2cm^{-1}. The net modal loss data was then converted to modal absorption data, by subtraction of the internal waveguide loss (α_i) and multiplying by -1, as $G(hv) = -A(hv)$. This is shown in Figure 5.6.

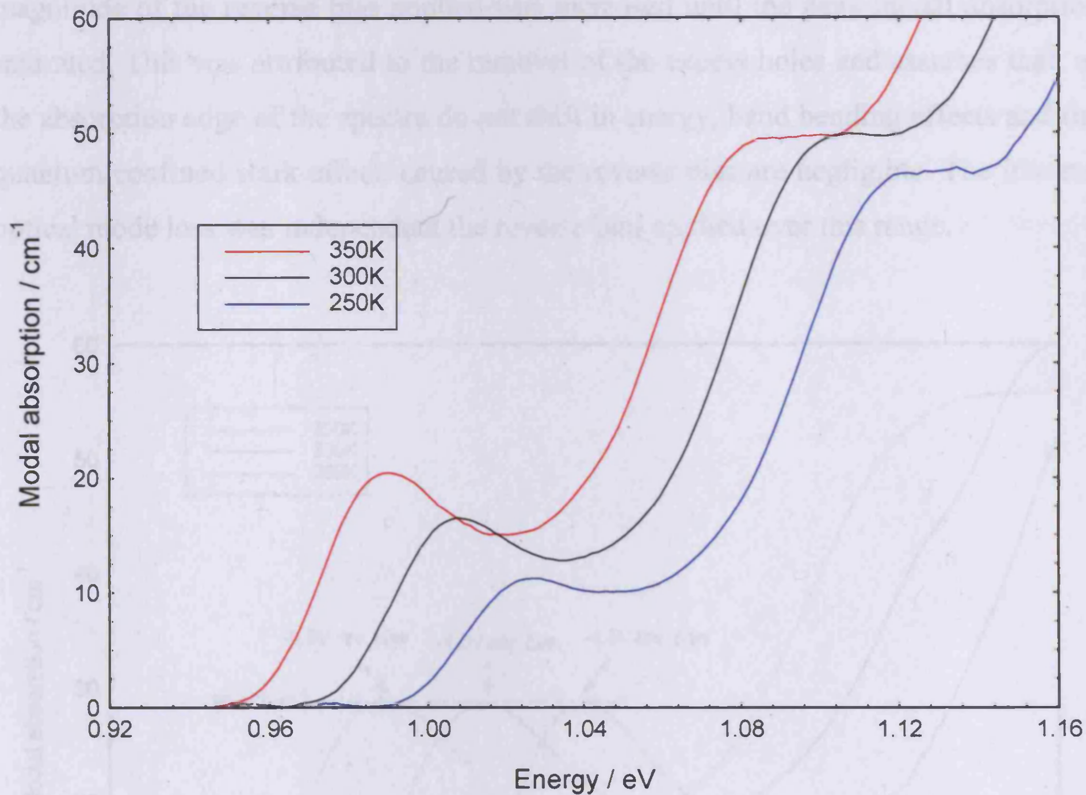

Figure 5.6 – Modal absorption spectra for the tunnel injection structure at 250K (blue), 300K (black) and 350K (red).

The data shows that the peak ground state modal absorption for this material varies from 20±2cm^{-1} to 11±2cm^{-1} between 350K and 250K. As the number of states present within the structure does not vary with temperature, the magnitude of the ground state absorption should remain constant with temperature, provided the magnitude of the broadening remains constant.

The effect seen in the data, where the magnitude of the absorption changes as a function of temperature, can be caused by the P-doping present within this structure.

The doping provides excess holes, some of which are captured into the dot ensemble, leading to a reduced modal absorption by Pauli state blocking [55]. The effect of the P–doping on the measured absorption in Figure 5.6 decreases with increasing temperature due to increased thermalisation of holes out of the QD states.

I have applied a reverse bias to the passive section while performing the net modal loss measurement using the technique described in Section 3.52. This removes the excess holes caused by the P-doping, allowing the true modal absorption to be measured as a function of temperature (Figure 5.7). It should be noted that the magnitude of the reverse bias applied was increased until the peak modal absorption saturated. This was attributed to the removal of the excess holes and assumes that, as the absorption edge of the spectra do not shift in energy, band bending effects and the quantum confined stark effect, caused by the reverse bias are negligible. The internal optical mode loss was independent the reverse bias applied over this range.

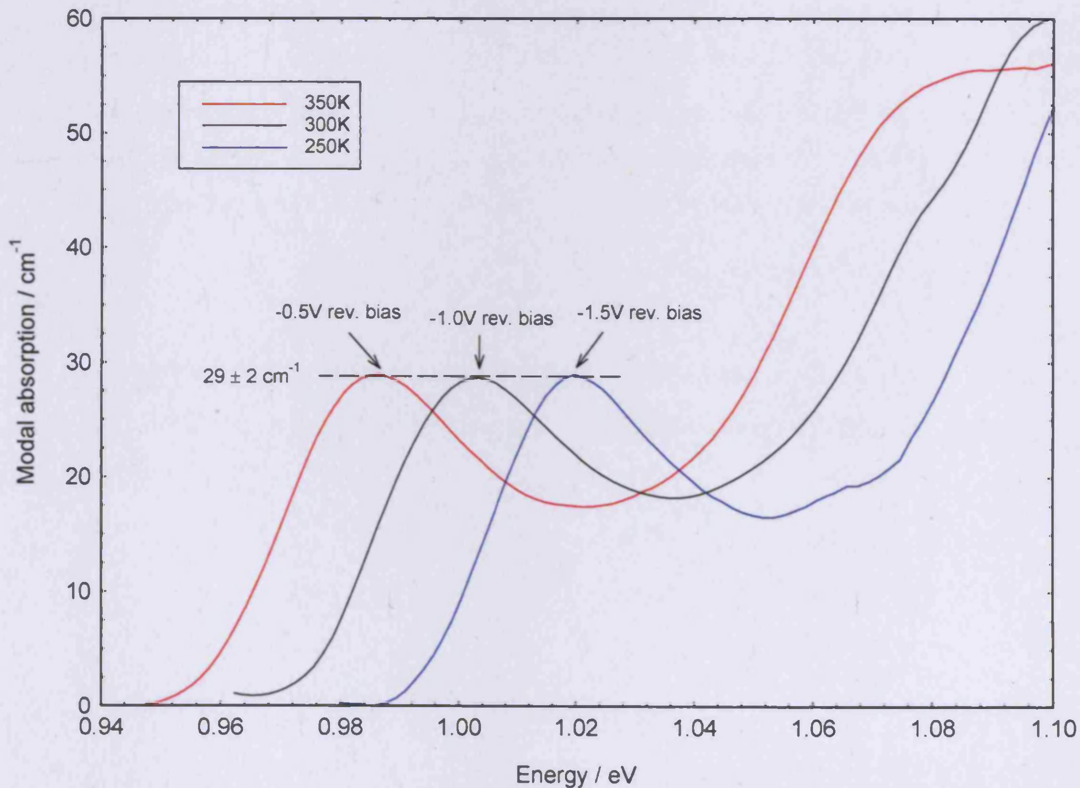

Figure 5.7 – Net modal loss spectra for the tunnel injection structure at 250K (blue), 300K (black) and 350K (red) all under an applied reverse bias.

The magnitude of the reverse bias required to remove the excess holes decreases with increasing temperature. The peak ground state modal absorption (taking account of the internal waveguide loss) is $29\pm2cm^{-1}$ and the first excited state modal absorption is $56\pm2cm^{-1}$. The errors are estimated from the uncertainty in the peak saturation and the internal waveguide loss. They all have equal value as these errors are related quantities.

The absorption curves have been fitted, assuming a Gaussian distribution of energies throughout the ensemble. This fitting has been performed on both the unbiased and the reverse biased absorption curves. To achieve this fit, a bimodal dot population had to be assumed. Without this assumption no agreement could be formed between the fitted and measured data over a large energy range. This was true while fitting both the reverse biased and unbiased absorption spectra. An example of a fitted modal absorption spectrum from the tunnel injection sample, at 300K reverse biased, assuming a monomodal size distribution is shown in Figure 5.8.

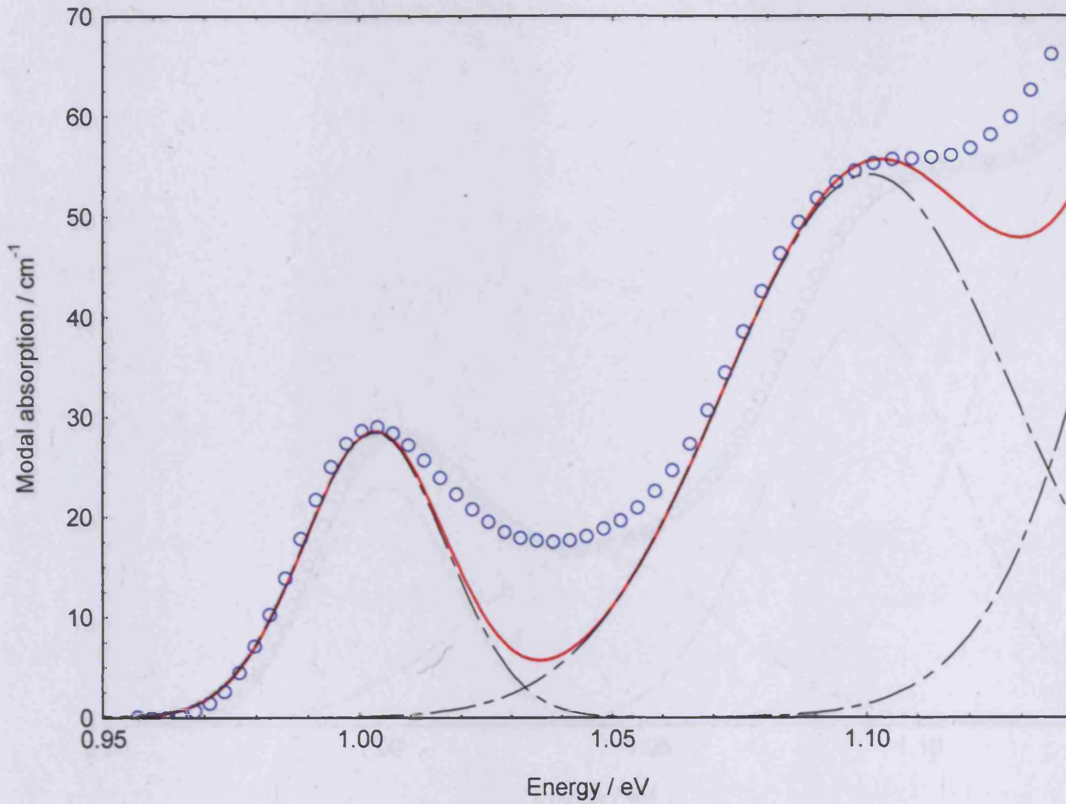

Figure 5.8 – Fitted modal absorption curve for the tunnel injection structure at 300K TE assuming a monomodal size distribution. The measured data with reverse bias applied, is presented (blue) along with the overall fit (red) and the contributions from the dots states (black).

An example of a fitted modal absorption spectrum from the tunnel injection sample at 300K reverse biased, where a bimodal dot population is assumed is illustrated in Figure 5.9.

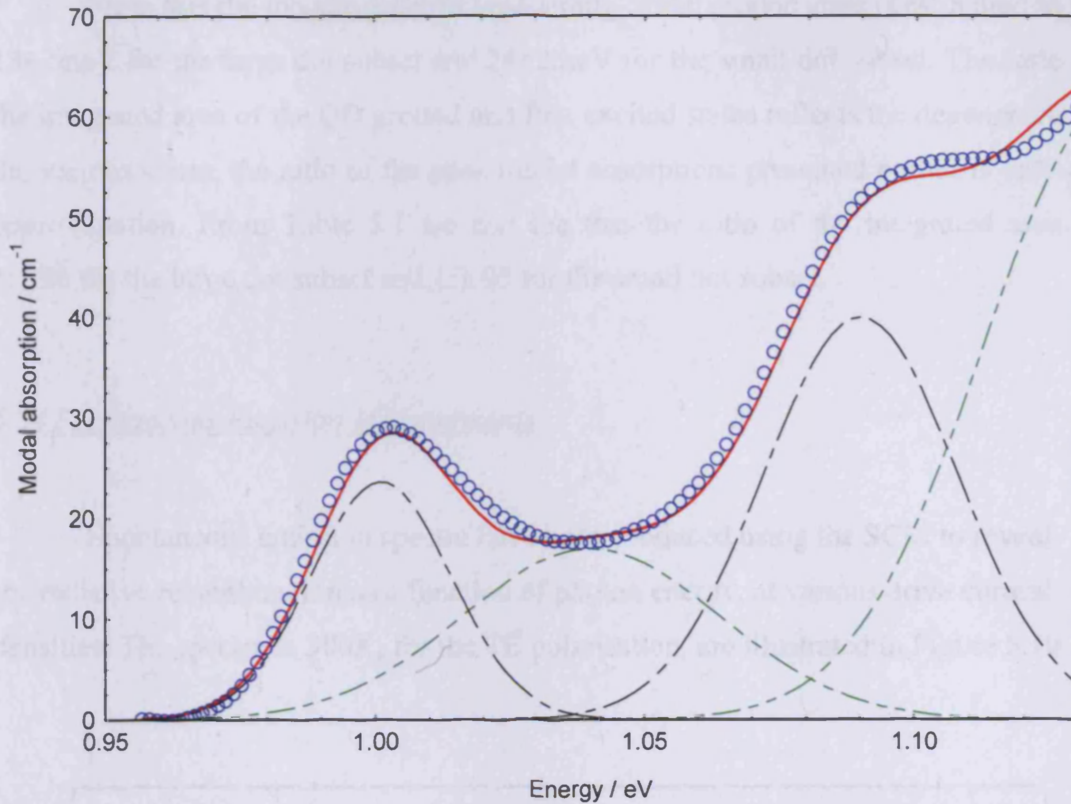

Figure 5.9 – Fitted modal absorption curve for the tunnel injection structure at 300K TE assuming a bimodal dot population. The measured data with reverse bias applied, is presented (blue) along with the overall fit (red). Fitting includes contributions from large dots (black) and small dots (green).

The parameters used to achieve the fitting in Figure 5.9 are listed in Table 5.1.

Dot Subset	State	Peak energy (eV)	Broadening (meV)	Integrated area ($eVcm^{-1}$)
Large	Ground	1.002 ± 0.002	13 ± 2	506
Large	1st excited	1.089 ± 0.002	28 ± 2	994
Small	Ground	1.040 ± 0.002	24 ± 2	621
Small	1st excited	1.137 ± 0.002	24 ± 2	1210

Table 5.1 – Parameters used to fit the modal absorption for the tunnel injection structure at 300K TE.

From this the inhomogeneous broadening of the ground state is estimated to be 13±2meV for the large dot subset and 24±2meV for the small dot subset. The ratio of the integrated area of the QD ground and first excited states reflects the degeneracy of the various states, the ratio of the peak modal absorptions presented earlier is only an approximation. From Table 5.1 we can see that the ratio of the integrated area is 1:1.96 for the large dot subset and 1:1.95 for the small dot subset.

5.34 Spontaneous Emission Measurements

Spontaneous emission spectra have been produced using the SCM to reveal the radiative recombination as a function of photon energy, at various drive current densities. The spectra at 300K, for the TE polarisation, are illustrated in Figure 5.10.

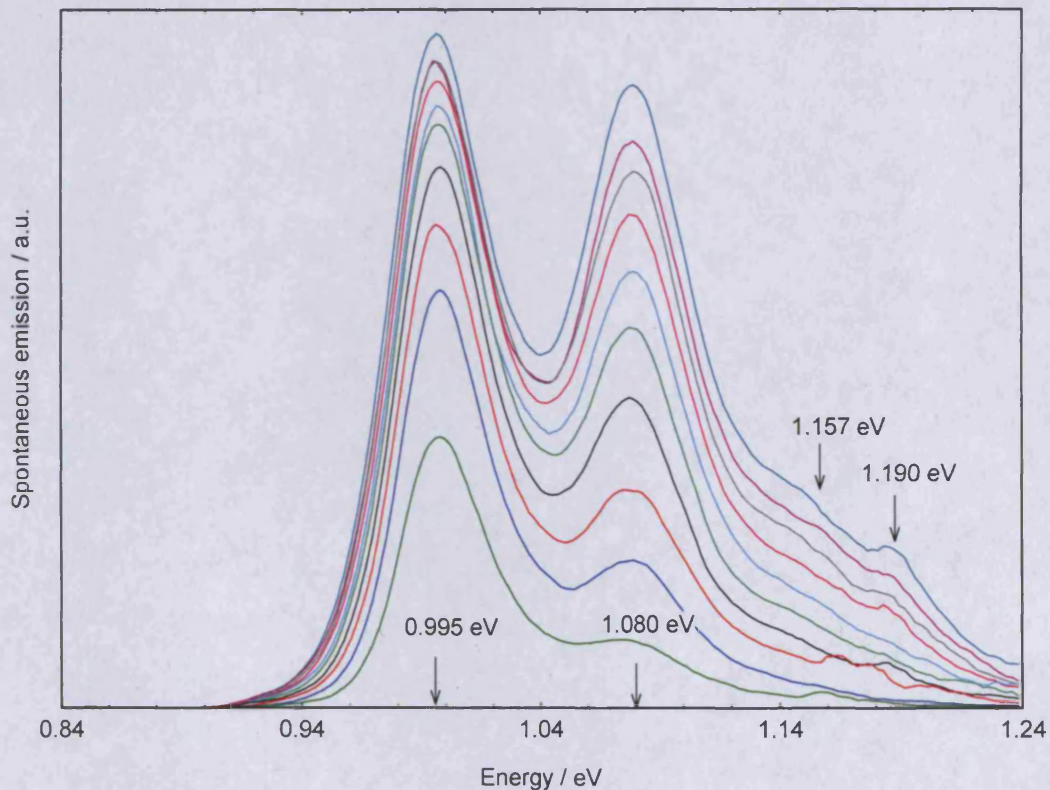

Figure 5.10 – Spontaneous emission spectra for the tunnel injection structure at 300K TE for current densities between 111Acm^{-2} and 1111Acm^{-2} at 5kHz repetition rate with a 500ns pulse width.

We observe significant radiative recombination from the inhomogeneously broadened QD ground (0.995eV) and first excited (1.080) states, where the energy spacing of the states agrees with that seen on the EPVS data (Figure 5.3).

The peak energy of the QD states in the EPVS measurements is 12meV higher that that observed in the spontaneous emission measurements. This can be attributed to Coulomb interaction between the confined carriers during the spontaneous emission measurement leading to a reduction in the transition energy.

In Figure 5.10 we are able to resolve recombination from the QD second excited state (1.157eV), where its peak position is affected by the close proximity of the injector well states. The emission from the QD second excited state is however weak compared to that of the QD ground and first excite states. We can also see that the peak energy of the spontaneous emission does not change with carrier density. We observe a small peak at 1.190eV which corresponds to the recombination energy predicted for the injector well. This peak is however, insignificant at this temperature.

We can now consider how the radiative recombination properties of the tunnel injection structure behave with variations in temperature. The spontaneous emission spectra from 250K to 350K TE for the tunnel injection structure are illustrated in Figure 5.11.

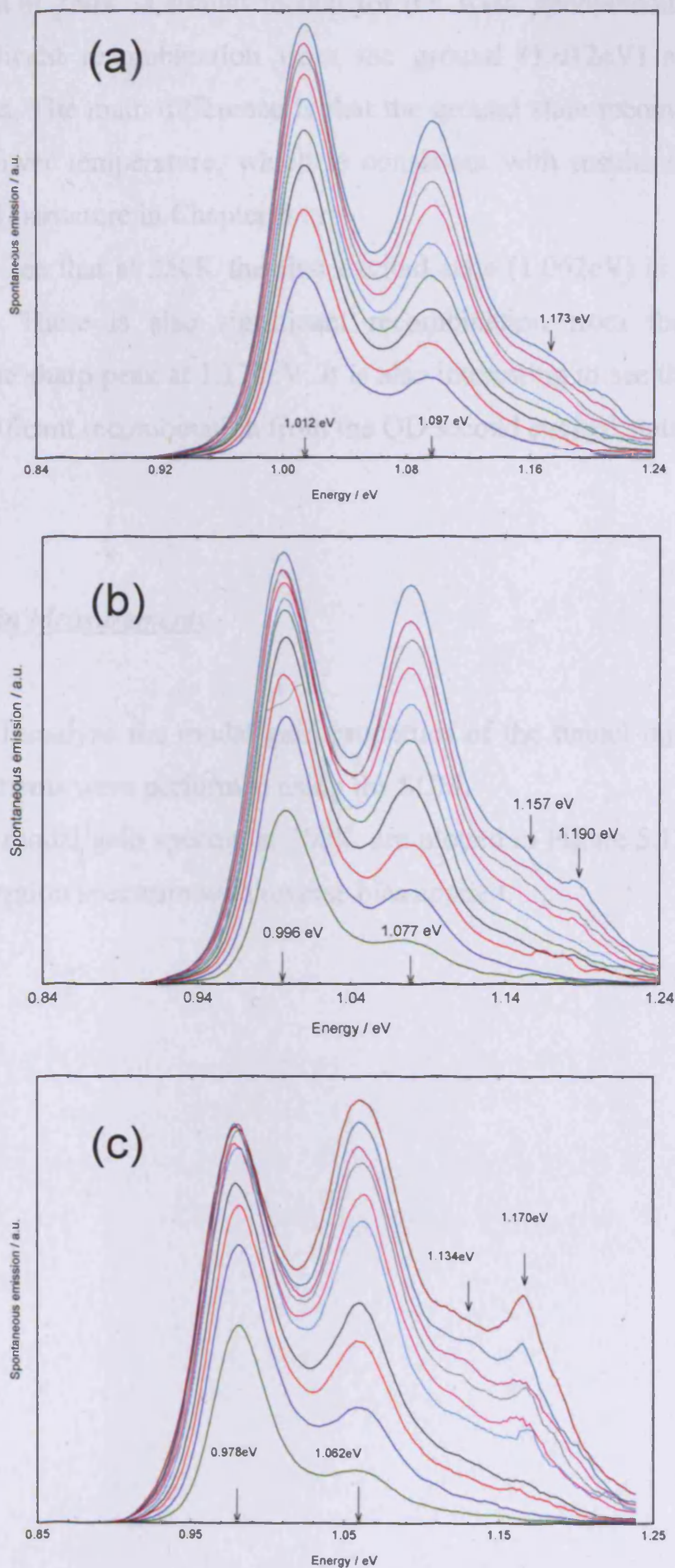

Figure 5.11 – Spontaneous emission spectra for the tunnel injection structure at (a) 250K, (b) 300K and (c) 350K TE for current densities between 111Acm^{-2} and 1333Acm^{-2} with a duty cycle of 0.25%.

The data at 250K is similar to that for the 300K spontaneous emission, with the only significant recombination from the ground (1.012eV) and first excited (1.097eV) states. The main difference is that the ground state recombination is more prominent at lower temperature, which is consistent with results seen in the high performance QD structure in Chapter four.

We can see that at 350K the first excited state (1.062eV) is more prominent than at 300K. There is also significant recombination from the injector well, illustrated by the sharp peak at 1.170eV. It is also interesting to see that even at 350K there is no significant recombination from the QD second excited state (1.134eV).

5.35 Modal Gain Measurements

In this section I analyse the modal gain properties of the tunnel injection structure. These measurements were performed using the SCM.

The net modal gain spectra, at 300K, are plotted in Figure 5.12 along with the net modal absorption spectrum with reverse bias applied.

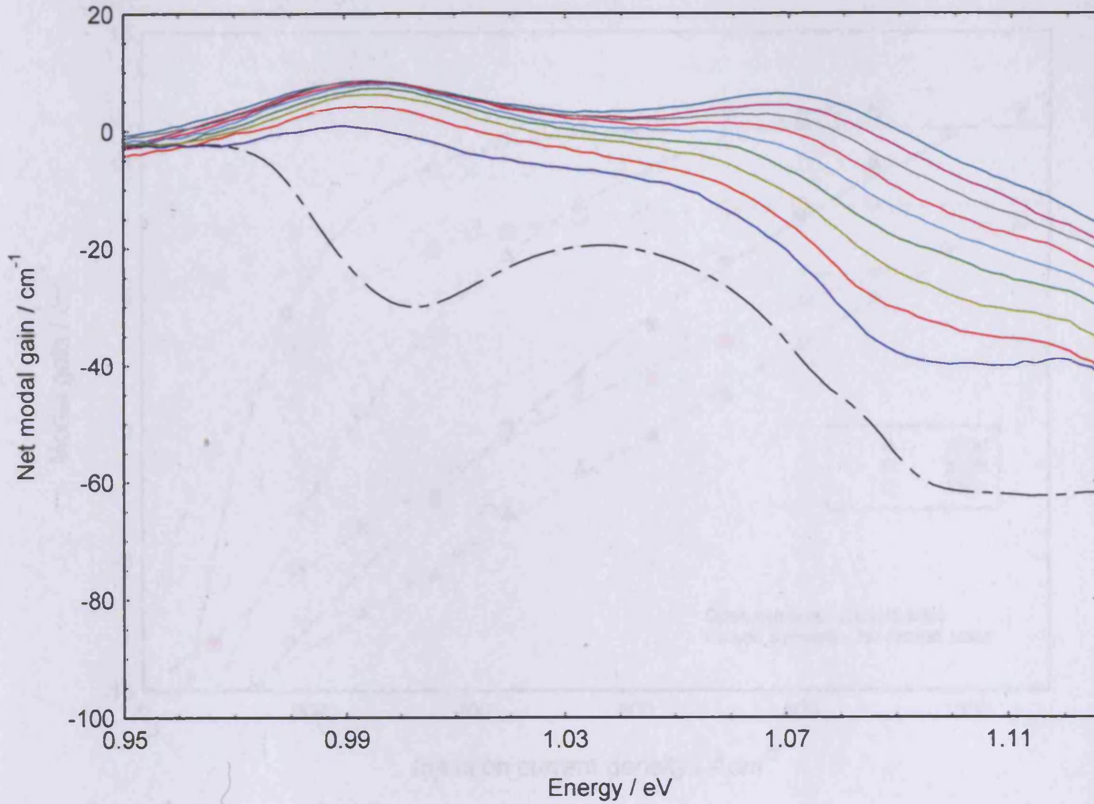

Figure 5.12 – Net modal gain spectra for the tunnel injection structure at 300K TE for current densities between 111Acm^{-2} and 1111Acm^{-2} with a duty cycle of 0.2%

We can clearly resolve two peaks from the dot ground and first excited state, but no clear gain is observed from the dot second excited state within the measured range. The ground state modal gain saturates at 11.5±1cm^{-1}.

The peak modal gain for both the ground (open symbols) and first excited (closed symbols) states is plotted against injection current density at 250K, 300K and 350K in Figure 5.13.

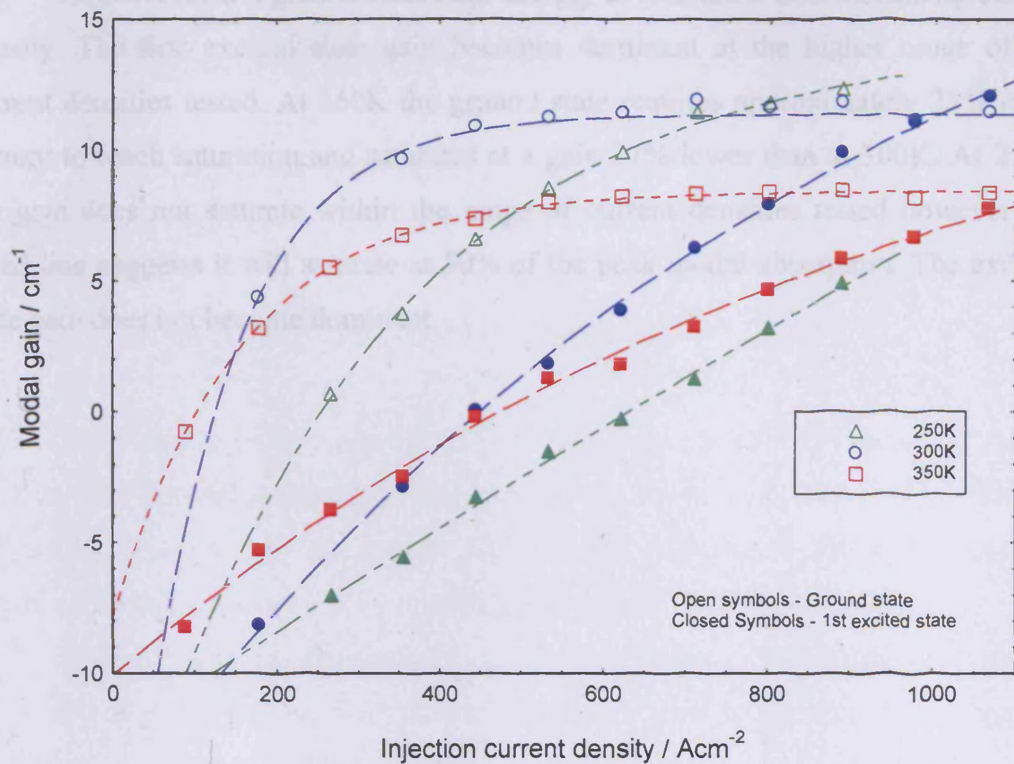

Figure 5.13 – Modal gain as function of injection current density at 250K (green), 300K (blue) and 350K (red) where open symbols refer to the QD ground state and closed symbols the QD first excited state.

The curves have been fitted in the same way as those shown in Chapter four, Section 4.33 and the fitting parameters are shown in Table 5.2

Temperature	State	G_{sat} (cm^{-1})	γ	J_t (Acm^{-2})
250	Ground	14.34	0.82	254.87
250	1st excited	24.03	0.50	615.00
300	Ground	11.63	0.94	118.99
300	1st excited	29.06	0.41	452.12
350	Ground	8.43	0.66	102.30
350	1st excited	17.95	0.44	476.54

Table 5.2 – Parameters used to fit the modal gain vs current density curves in Figure 5.13.

At 300K the dot ground state rises sharply to saturation with increasing current density. The first excited state gain becomes dominant at the higher range of the current densities tested. At 350K the ground state requires approximately 23% more current to reach saturation and saturates at a gain 27% lower than at 300K. At 250K the gain does not saturate within the range of current densities tested however the fitted line suggests it will saturate at 50% of the peak modal absorption. The excited state gain does not become dominant.

5.4 Interpretation and Discussion of Results

In this Section I discuss the measured data shown in Section 5.3 and provide explanations for the observed characteristics.

5.41 Edge Photo-voltage Spectroscopy Measurements

The polarisation sensitive EPVS [76] measurements were shown in Figure 5.3. We observed two inhomogeneously broadened QD states along with a small feature which I attribute to the QD second excited state, however its absorption peak is shifted and masked by the closely spaced injector well.

It should be noted that the energy separation between the QD and injector well states observed in the absorption measurements, is related to the transition energy of the various states through the conduction band offsets.

The two sharp absorption features are attributed to the light hole and heavy hole transitions in the injector well. Their energy separation (27meV) is similar to that found using a simplistic model of the injector well (33meV) shown in Section 5.2. It was assumed that neither of these transitions originate from the wetting layer states because this thin layer would lead to a broader absorption feature than those observed.

5.42 Laser Threshold and Temperature Stability

In Figure 5.4 I showed the variation of threshold current density between 180K and 360K for lasers of length 0.66, 0.9, 1.5 and 1.8mm. For the 1.5mm and 1.8mm long lasers the threshold current density does not change significantly over the operating range of 290K to 350K, for example the variation for the 1.8mm long laser over this temperature range is 255±70mA. This agrees with the results found by Mi et al. (2005) [74] when this material was tested in Michigan.

For the shorter length lasers however there is a significant variation in threshold current density with temperature. For the 0.66mm long laser, only first excited state lasing could be achieved and only between 210K and 320K.

For the 0.9mm long laser two-state lasing was observed at 300K, at lower temperatures ground state lasing took place and at higher temperatures first excited state lasing took place. The two-state lasing did not however take place at all current injection levels. At low injection ground state lasing took place and at high injection both states appeared to lase simultaneously.

Two-state lasing has previously been observed and modelled by other groups on a variety of QD structures [77-79]. Marcus et al [78] attribute the simultaneous lasing to the finite relaxation time between dot first excited and ground state. It is postulated that at laser threshold the ground state population pins and further carrier injection increases the rate of stimulated emission. Due to the finite relaxation time from the QD first excited to ground state τ_{21}, the excited state population must increase to meet the increased demand for carriers in the QD ground state under lasing conditions. An illustration of the main relaxation rates for a QD with two confined energy states is shown in Figure 5.14 where τ_c is the electron capture rate into the QD first excited state and τ_{rad} is the ground state radiative recombination rate.

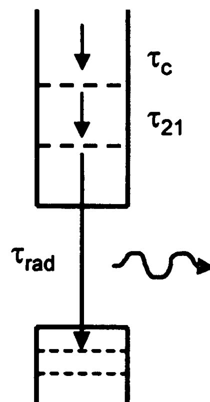

Figure 5.14 – Illustration of the main relaxation rates in a QD containing two confined states.

The increase of carrier population in the first excited state continues until lasing occurs on both states, where the finite relaxation time maintains lasing on both states. This process requires a highly non-thermal distribution in the electron population to be present in the QDs. As will be shown in Chapter six, this is not the case for the tunnel injection samples at 300K. It has also been observed [78] that the

light intensity from the ground state (GS), under lasing conditions, decreases as the level of current injection is raised.

This can be attributed to a thermal distribution among the closely spaced hole states [78], meaning that the GS and excited state (ES) electrons compete for the same hole states under lasing conditions. As the current injection level is raised, the higher degeneracy of the ES leads to carriers within this state recombining more readily, with the finite number of hole states leading to a reduction in intensity from the GS.

To fully understand this feature of the tunnel injection structures under lasing conditions, I explored whether the two-state lasing is simultaneous or if there is a fast switching between the lasing states. This was done using an Oriel 1/4 m monochromator coupled to a Thorlabs DET410 InGaAs detector, where the output voltage was sampled with a digital oscilloscope.

The results are illustrated in Figure 5.14, where the intensities of the lasing pulses have been normalised.

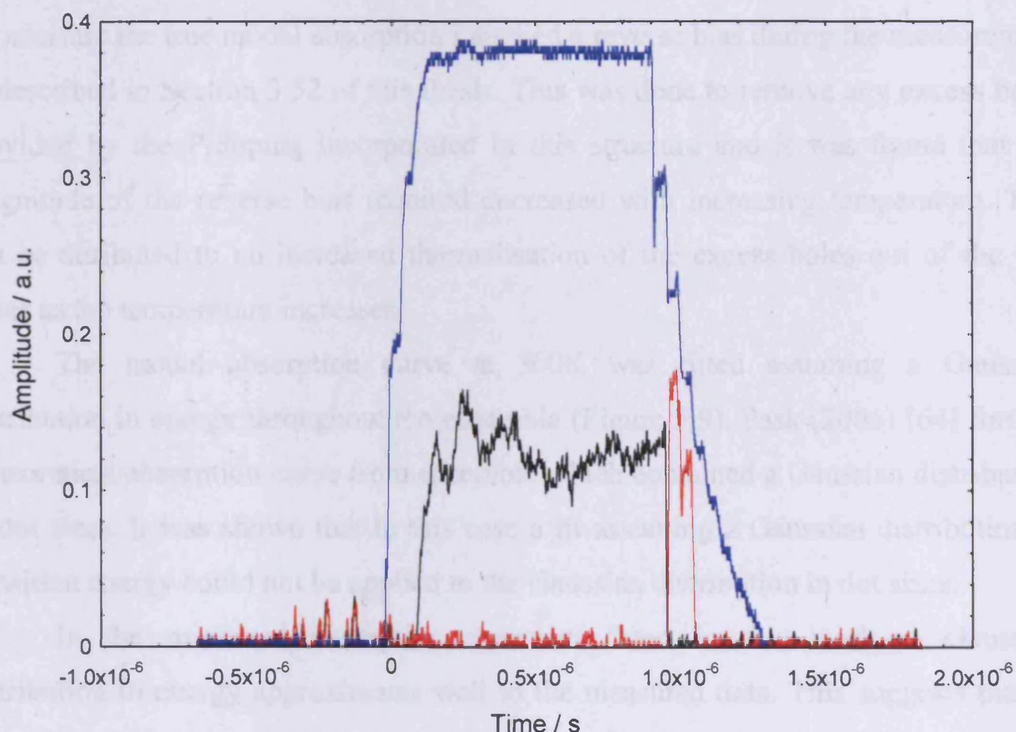

Figure 5.14 – Oscilloscope traces reflecting the amplitudes and duration of the current pulse (blue), QD first excited state (black) and QD ground state (red) during 2 state lasing of a 0.90mm long laser driven at 1250Acm^{-2} with a 0.25% duty cycle at 300K.

The dot first excited state (black) lases over the majority of the current pulse (blue). As the pulse intensity begins to fall the first excited state abruptly switches off and the ground state (red) switches on.

This result shows that for this structure, at this current injection level, the dual state lasing is not simultaneous. At the high current density when the pulse is on, lasing occurs on the ES which could limit the relaxation rate of carriers to the ground state. As the current density falls the ES has insufficient gain to lase and so the carrier supply to the GS is restored, allowing the ground state to lase for the brief period where there are enough carriers supplied by the decaying pulse.

5.43 <u>Modal Absorption Measurements</u>

It was shown in Section 5.33 that the peak modal absorption for the QD ground and first excited states between 250K and 350K was $29\pm2cm^{-1}$ and $56\pm2cm^{-1}$. To measure the true modal absorption I applied a reverse bias during the measurement as described in Section 3.52 of this thesis. This was done to remove any excess holes provided by the P-doping incorporated in this structure and it was found that the magnitude of the reverse bias required decreased with increasing temperature. This can be attributed to an increased thermalisation of the excess holes out of the QD states as the temperature increases.

The modal absorption curve at 300K was fitted assuming a Gaussian distribution in energy throughout the ensemble (Figure 5.9). Pask (2006) [64] formed a theoretical absorption curve from ensemble which contained a Gaussian distribution of dot sizes. It was shown that in this case a fit assuming a Gaussian distribution in transition energy could not be applied to the Gaussian distribution in dot sizes.

In the measured absorption spectrum fitted in this work, a Gaussian distribution in energy approximates well to the measured data. This suggests that in this case the assumption of a Gaussian distribution in energy is appropriate.

The fitting procedure revealed a bimodal dot population within the ensemble and a narrow inhomogeneous broadening, similar to that observed in the high performance QD laser in Chapter four. This similarity makes the high performance QD structure ideal for comparison with the tunnel injection structure as the contribution of both the small inhomogeneous linewidth and the bimodal dot population can be excluded when explaining the properties of the tunnel injection structure in Chapter six.

Using the fitting procedure I estimated the number of QD ground states occupied by P-dopant atoms. I compared the integrated area for the fitted modal absorption curves for the reverse bias and the unbiased data in Table 5.3.

Dot Subset	Bias / Applied	Broadening (meV)	Area ($eVcm^{-1}$)
Small	0V	24 ± 2	463
Small	-1V	24 ± 2	621
Large	0V	13 ± 2	266
Large	-1V	13 ± 2	506

Table 5.3 – Comparison between integrated areas of the ground state transitions for the biased and unbiased absorption curves at 300K TE.

Using the ratio of the areas in Table 5.3 we can see that 53% of the large dot states available and 75% of the small dot states available are occupied by holes supplied from the P-doping. This is over double that found by Sandall et al. [37] during studies of other P-doped QD samples, where the doping was nominally of a similar level to that found in the tunnel injection samples.

5.44 Spontaneous Emission Measurements

The spontaneous emission was measured using the SCM over a range of drive current densities (Figure 5.10). Significant recombination was observed from the inhomogeneously broadened QD ground and first excited states along with a smaller peak at higher energy corresponding to the second excited state. The recombination from the QD ground and first excited states shows the tunnel injection process is working well with fast relaxation between the two states.

The low level of recombination from the QD second excited state suggests that at this temperature excitation of carriers out of the first excited state is not significant although this could be attributed to the device not being electrically pumped enough to observe such recombination. We can compare the spontaneous emission between the tunnel injection structure and the high performance QD structure from Chapter four at 300K.

To ensure the spontaneous emission spectra are driven at equal levels, I plot the spectra at constant quasi-Fermi level separation minus ground state transition energy. The quasi-Fermi level separation was extracted from the transparency point of the measured modal gain spectra shown in Sections 4.33 and 5.35, using the procedure explained in Chapter three, Section 3.51. I have also normalised the integrated area under each curve so that the data measured in arbitrary units can be compared. This is shown in Figure 5.15.

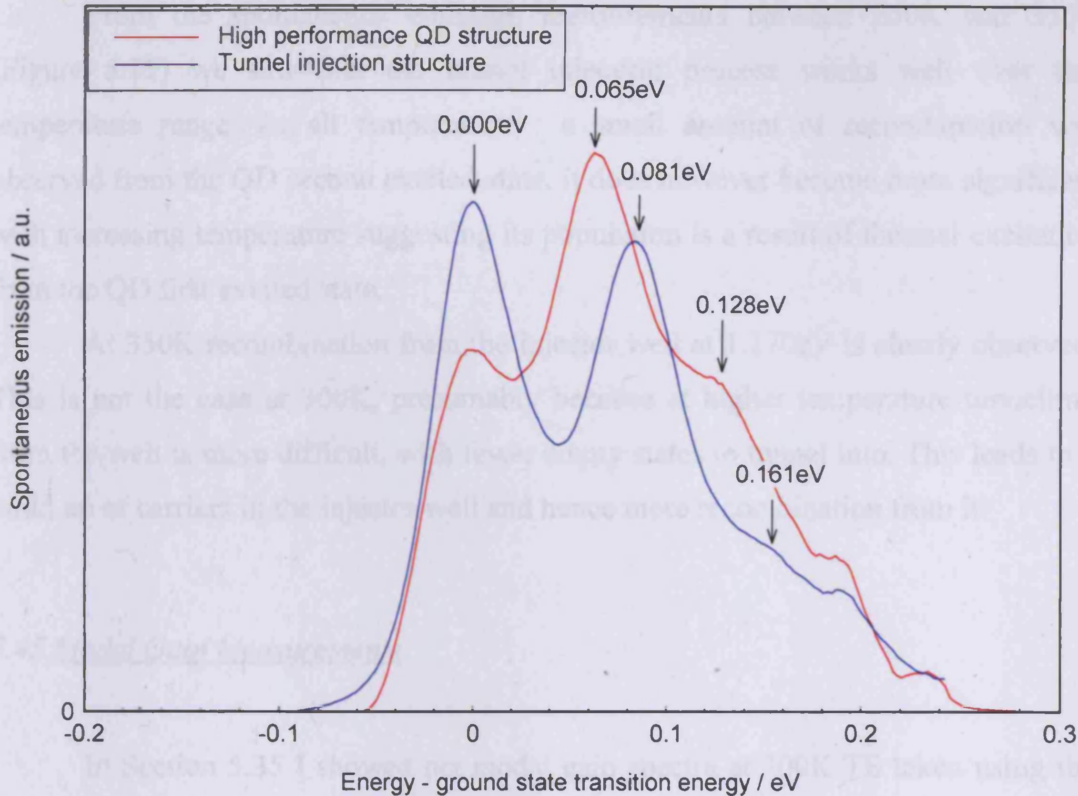

Figure 5.15 – Spontaneous emission spectra at quasi-Fermi level separation – ground state transition energy = 0.088eV, for the tunnel injection structure the standard QD sample at 300K.

The spontaneous emission from the high performance QD structure shows significant recombination from both the dot first (0.065eV) and second (0.128eV) excited states, both greater than that of the ground state (0.000eV). The energies quoted reflect the transition energy after subtraction of the ground state transition energy for the data. We note that in this structure, the carriers relax down through all the higher energy dot states before recombining.

The occupation of the QD states is clearly different for the two structures and can be explained by the differences in their carrier distributions which will be shown in Chapter six.

There was no observed shift in the peak energy of the spontaneous emission with current injection for either structure at 300K and as will be shown in Chapter six, the high performance structure exhibits a thermal distribution at this temperature. This suggests the lack of shift in peak energy in both structures is related to the pumping levels and not the carrier distribution, as explained in Section 4.42.

From the spontaneous emission measurements between 250K and 350K (Figure 5.11) we saw that the tunnel injection process works well over this temperature range. At all temperatures a small amount of recombination was observed from the QD second excited state, it does however become more significant with increasing temperature suggesting its population is a result of thermal excitation from the QD first excited state.

At 350K recombination from the injector well at 1.170eV is clearly observed. This is not the case at 300K, presumably because at higher temperature tunnelling from the well is more difficult, with fewer empty states to tunnel into. This leads to a build up of carriers in the injector well and hence more recombination from it.

5.45 Modal Gain Measurements

In Section 5.35 I showed net modal gain spectra at 300K TE taken using the SCM (Figure 5.11). Modal gain peaks were observed from the QD ground and first excited states but not the QD second excited state over this current range. This is expected from the spontaneous emission measurements discussed in Section 5.44 which revealed this state is relatively under populated due to the injection process.

In Figure 5.13 the modal gain vs injection current density was plotted at 250K, 300K and 350K. This revealed that at 300K the modal gain from the QD ground state saturated at 11.5cm^{-1}. This corresponds to 40% of the peak ground state modal absorption observed in Figure 5.7 suggesting that a large number of QD states are not contributing to the gain at saturation.

This effect increases with temperature, at 250K it appears that saturation will occur at 50% of the peak absorption and at 350K saturation occurs at 27% of the peak absorption. The lower value of saturated gain, at higher temperature, is usually attributed to thermalisation of carriers out of the ground state, however it could also be a result of a non-radiative process present leading to a lower carrier density in the QD states.

At 250K the gain does not saturate within the range of current densities tested and the excited state gain does not become dominant. This behaviour is similar to that seen in the high performance QD structure and can be attributed to less thermalisation of carriers out of the ground state.

I have plotted the ground state modal gain, against the quasi-Fermi level separation minus ground state transition energy for both the tunnel injection structure and the typical QD structure (Figure 5.16).

This plot allows a comparison between the gain of different structures, whose transition energy may differ, while driving each structure to the same level. The standard QD structure is a high performance 5 layer dot in a well (DWELL) structure in which no P-doping has been incorporated; further details of the design and growth can be found in Section 4.2.

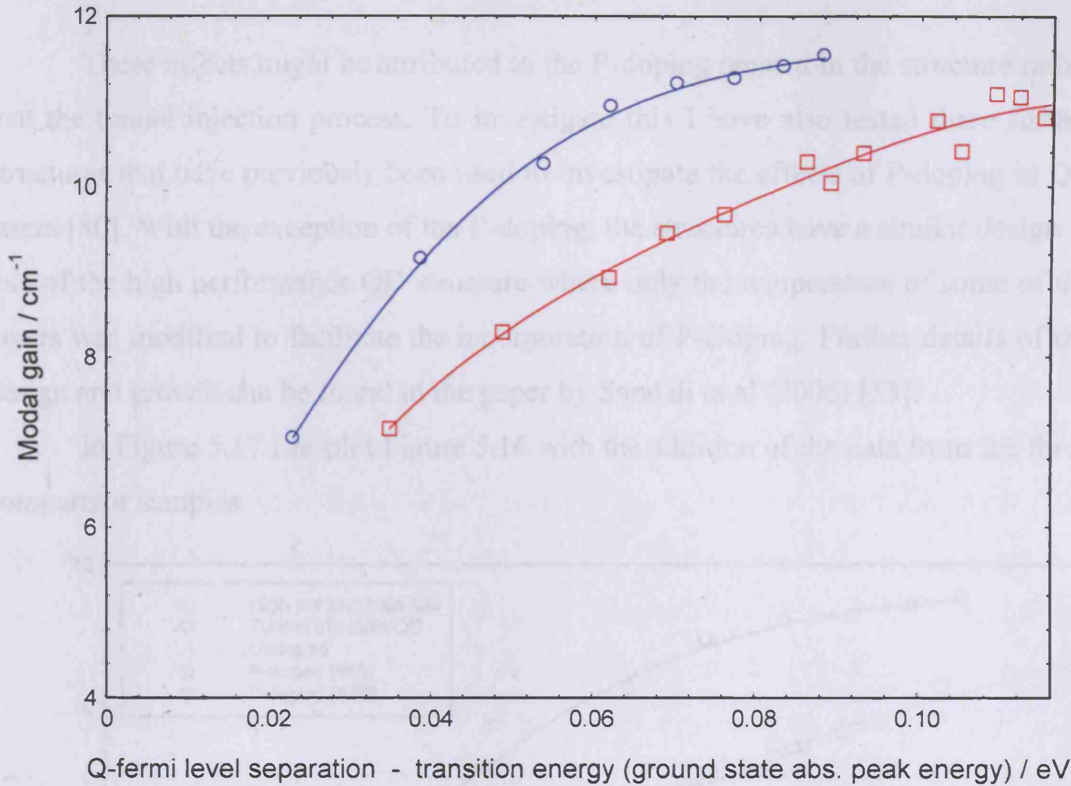

Figure 5.16 – Ground state peak modal gain vs quasi-Fermi level separation minus transition energy for the tunnel injection structure (blue) and the high performance QD structure (red).

This shows that the differential gain is higher for the tunnel injection structure than that of the high performance QD structure. As the carriers in the tunnel injection structure bypass both the wetting layer and higher energy dot states and the carriers in the standard sample do not, this data suggests that the relaxation processes for the carriers through the wetting layer and higher energy QD states, limit the differential gain in typical QD lasers.

The saturated ground state modal gain is also higher for the tunnel injection structure although not substantially. This similarity and the fact that the peak modal gains from both structures reveals they are not fully inverted at saturation, suggests the relaxation from the QD first excited to ground state is the major limiting factor on the performance of both devices.

These effects might be attributed to the P-doping present in the structure rather that the tunnel injection process. To investigate this I have also tested three further structures that have previously been used to investigate the effects of P-doping in QD lasers [80]. With the exception of the P-doping, the structures have a similar design to that of the high performance QD structure where only the temperature of some of the layers was modified to facilitate the incorporation of P-Doping. Further details of the design and growth can be found in the paper by Sandall et al (2006) [53].

In Figure 5.17 I re-plot Figure 5.16 with the addition of the data from the three comparator samples.

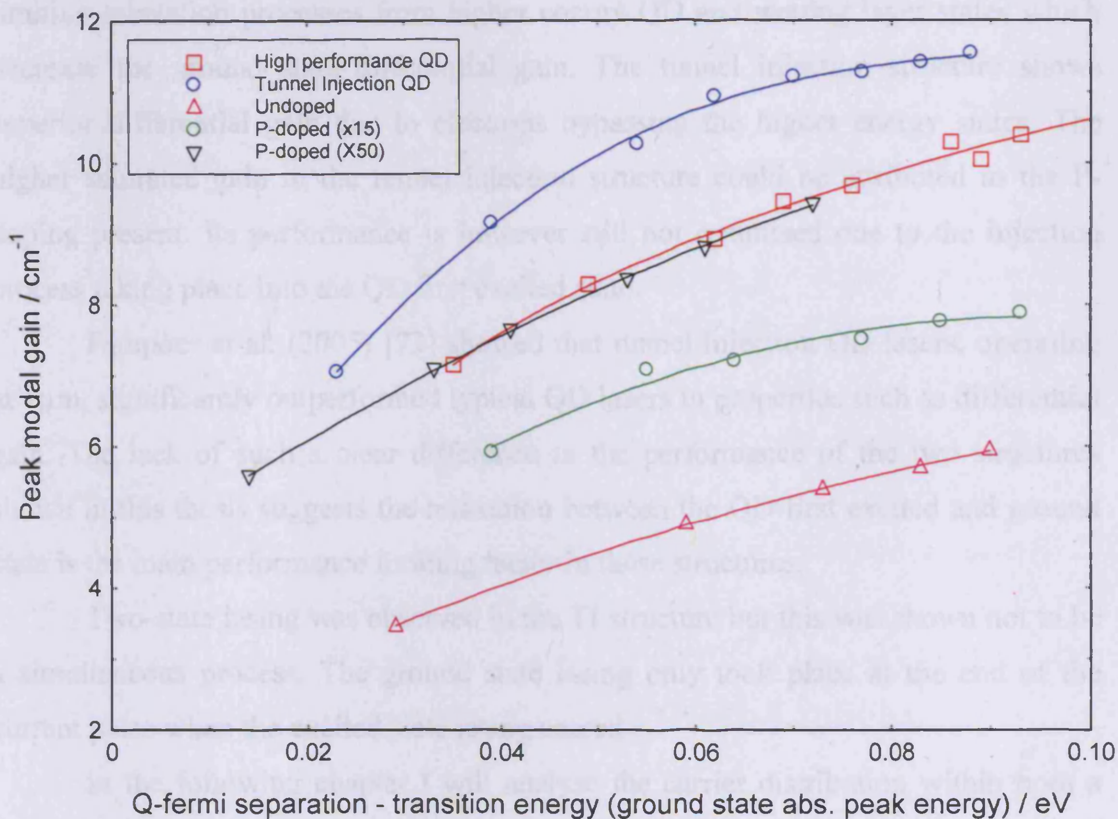

Figure 5.17 – Ground state peak modal gain vs quasi-Fermi level separation minus transition energy at 300K TE for the tunnel injection structure (blue), the high performance QD structure (red), undoped comparator (pink), P-doped (X15) comparator (green) and P-doped (X50) comparator (black).

We can see from this graph that the addition of the P-doping leads to an increase in the saturated modal gain however it has little effect on the differential gain. The peak modal gain from the tunnel injection structure is larger than all the samples used for comparison.

5.5 Conclusion

In this chapter I have characterised the tunnel injection quantum dot laser using a combination of modal absorption, modal gain, spontaneous emission and lasing properties. This has revealed a structure in which electrons are injected into the QD first excited state before recombining from either the QD ground or first excited state.

The comparison between the tunnel injection structure and the typical QD laser from Chapter four has revealed that typical QD structures suffer from rate limiting relaxation processes from higher energy QD and wetting layer states which decrease the ground state differential gain. The tunnel injection structure shows superior differential gain due to electrons bypassing the higher energy states. The higher saturated gain in the tunnel injection structure could be attributed to the P-doping present. Its performance is however still not optimised due to the injection process taking place into the QD first excited state.

Fathpour et al. (2005) [73] showed that tunnel injection QD lasers, operating at 1 μm, significantly outperformed typical QD lasers in properties such as differential gain. The lack of such a clear difference in the performance of the two structures shown in this thesis suggests the relaxation between the QD first excited and ground state is the main performance limiting factor in these structures.

Two-state lasing was observed in the TI structure but this was shown not to be a simultaneous process. The ground state lasing only took place at the end of the current pulse when the excited state lasing ceased

In the following chapter I will analyse the carrier distribution within both a typical QD laser and the tunnel injection structure and use the characterisation performed in this chapter and Chapter four to explain the remarkable features which are observed.

6. Carrier Distributions in Quantum Dot Laser Diodes

6.1 Introduction

In this chapter I analyse the carrier distribution within a high performance (HP) quantum dot (QD) laser and a QD laser which incorporates tunnel injection (TI). Until now there has been a lot of uncertainty about how carriers distribute themselves within QD lasers, particularly those which operate at 1.3μm.

It has been shown that in many cases, at room temperature and above, the carrier distribution of a QD laser can be described by Fermi-Dirac statistics (thermal distribution) [12-14]. There is also evidence to suggest that some dot systems have a thermal distribution between the dot ground states and a separate thermal distribution between the dot excited states [46]. In all cases the dot systems depart from a thermal equilibrium at low temperature.

The results described in this chapter establish how the carriers are distributed amongst the various QD and wetting layer states in the QD structures tested. Where the distribution of carriers is not described by a Fermi-Dirac statistics, I have analysed the relative population of the various dot states, via the degree of inversion as a function of photon energy, to help explain the origin of the observed distribution. This work is important as it can be used as a comparison between what can be considered a typical structure and structures with more complicated distributions, such as QD lasers incorporating tunnel injection. It can also be used to aid the design of future QD structures by providing an understanding of the current device limitations.

To form the inversion factor spectra shown in this section I have used Equation 2.25 from Section 2.44, reproduced below. This shows that the inversion factor (P_f), as a function of photon energy, is proportional to the ratio of the modal gain to the spontaneous emission. The spectral shape of the spontaneous emission and modal gain spectra is determined by the electron distribution in energy throughout the system so from these measured spectra, we can deduce the inversion factor [17].

$$P_f(\hbar\varpi) = \frac{n^2\hbar^2\varpi^2}{3\hbar^3c^2\pi^2}\cdot\frac{1}{w_{\mathrm{mod}}}\cdot\frac{G}{R_{sp}} = \frac{f_c - f_v}{f_c(1-f_v)} \qquad \text{Equation 6.1}$$

w_{mod} is the photon energy dependent effective mode width, f_c and f_v are the occupation probabilities of an electron, in the state which participates in the transition of energy $\hbar\varpi$. The P_f function describes the degree of inversion of a system at particular photon energy. While using Equation 6.1 to produce the P_f we assume no particular distribution of the carriers and so the distribution shown is purely a reflection of the measured data. In the case where all the carriers are distributed according to Fermi-Dirac statistics (thermally distributed) and described by the same quasi-Fermi level separation ΔE_f, then P_f at a particular temperature T can be described by [12]:

$$P_f(E_{h\nu}) = 1 - \exp\left(\frac{E_{h\nu} - \Delta E_f}{kT}\right) \qquad \text{Equation 6.2}$$

In this chapter I have used Equation 6.2 to form theoretical curves which describe systems whose carriers are distributed according to Fermi-Dirac statistics. The theoretical curves are plotted along with measured data to identify deviations from a thermal distribution. To form a thermal distribution curve, the quasi-Fermi level separation (ΔE_f) is set equal to the transparency energy taken from the experimentally measured modal gain spectrum.

6.2 Interpretation of P_f spectra

The experimentally measured spontaneous emission (R_{sp}^{meas}) is related to the true spontaneous emission (R_{sp}) by Equation 6.3 [17].

$$R_{sp}^{meas} = \beta C(1-R)R_{sp} = C' R_{sp} \qquad \text{Equation 6.3}$$

β is the fraction of spontaneous emission coupled into the waveguide, R is the facet reflectivity, C is a light extraction factor and C' is an overall calibration factor accounting for the collection geometry of the measurement system. The measured inversion factor is related to the true inversion factor by Equation 6.4.

$$\frac{G}{R_{sp}^{meas}} \frac{n^2 \hbar^2 \varpi^2}{3\hbar^3 c^2 \pi^2} . \frac{1}{w_{\text{mod}}} . = P_f^{meas} = \frac{1}{C'} P_f \qquad \text{Equation 6.4}$$

In an ideal experiment, where all the spontaneous emission from the electrically pumped section was collected $C' = 1$.

We can see from Equation 6.1 that in the case where $f_v = 1$, $P_f = -\infty$ and where $f_c = 1$ or $f_v = 0$, the measured $P_f = 1$. In this latter case the system is fully inverted at this photon energy, with all the electrons occupying states within the conduction band. P_f tends to unity in measured data at photon energies near the band edge, where complete inversion is most likely to occur. This provides us with a means to determine the factor C', from Equation 6.4. If we can identify a region of a P_f^{meas} spectra where $P_f \rightarrow 1$, we can extract a value for C' because in this region:

$$P_f^{meas} = \frac{1}{C'} \qquad \text{Equation 6.5}$$

An example of a theoretical P_f curve, where the carriers are thermally distributed is shown in Figure 6.1.

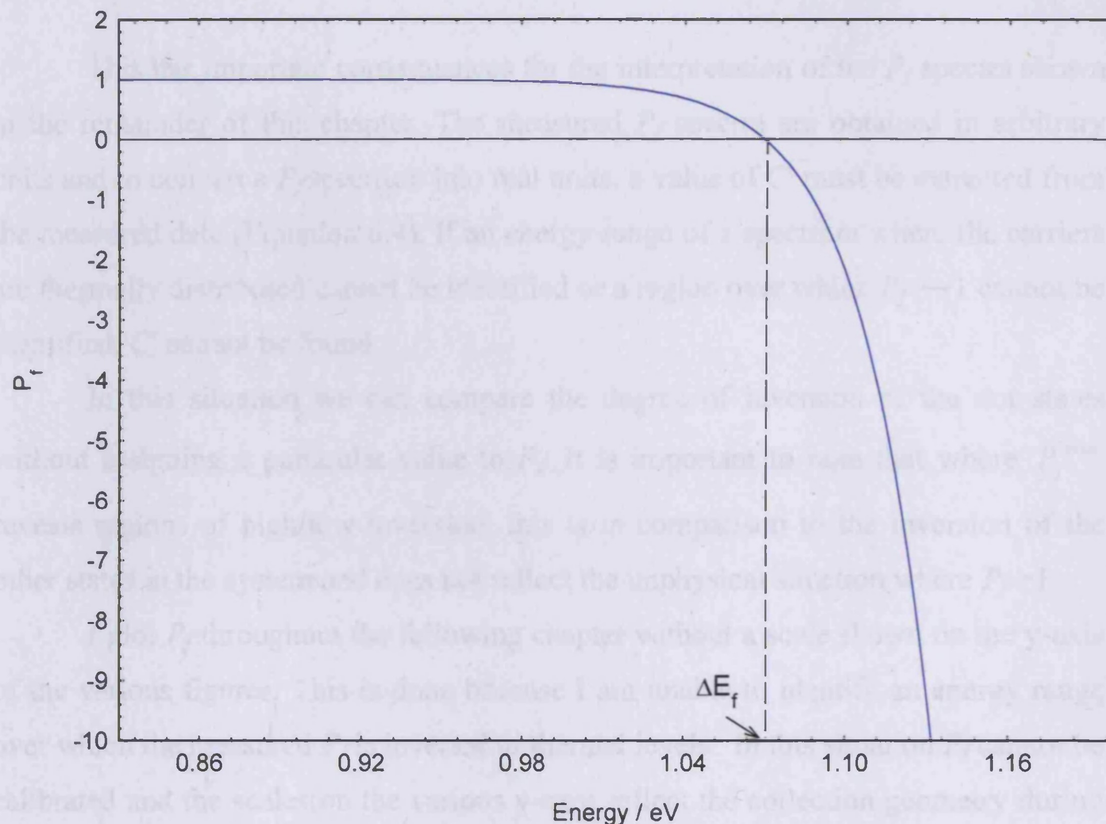

Figure 6.1 – Theoretical P_f spectrum (blue) highlighting the shape of a thermal distribution.

There are cases where a P_f^{meas} may appear to saturate at low energy even though $P_f \neq 1$. The dot states are populated by slow relaxation of electrons from higher energy states. Carriers which occupy the dot states also recombine leading to a reduction in the population of the dot states. With no fast redistribution process present to replace the lost carriers [81] the overall population of the dot states is reduced. Its overall population is determined by the both carrier supply rate and the recombination rate.

This is presumably not the case in QW lasers due to the rapid redistribution of carriers at a rate far greater than that of the recombination rate. The work by Summers et al. [79] considers a QD system where a single confined QD state is coupled to a wetting layer. The QD structures tested in this thesis contain multiple confined energy states and so slow relaxation processes between these states may further reduce the rate of carrier redistribution.

This has important consequences for the interpretation of the P_f spectra shown in the remainder of this chapter. The measured P_f spectra are obtained in arbitrary units and to convert a P_f spectrum into real units, a value of C' must be extracted from the measured data (Equation 6.4). If an energy range of a spectrum where the carriers are thermally distributed cannot be identified or a region over which $P_f \rightarrow 1$ cannot be identified, C' cannot be found.

In this situation we can compare the degree of inversion of the dot states without assigning a particular value to P_f. It is important to note that where P_f^{meas} reveals regions of high/low inversion, this is in comparison to the inversion of the other states in the system and does not reflect the unphysical situation where $P_f > 1$.

I plot P_f throughout the following chapter without a scale shown on the y-axis of the various figures. This is done because I am unable to identify an energy range over which the measured P_f is inverted to thermal levels. In this situation P_f cannot be calibrated and the scales on the various y-axes reflect the collection geometry during the measurement and cannot be compared to data measured at other times. For this reason I discuss the various features of the figures using percentages. These values are not affected by the collection geometry used and so the data in the figures can be compared.

6.3 Carrier Distribution in the HP Structure – Measured Data

The population inversion of the high performance (HP) QD structure has been analysed in the transverse electric (TE) polarisation, over a range of drive current densities and temperatures, to reveal the distribution of electrons within a typical QD laser. The data presented was extracted from the measured spontaneous emission and modal gain data shown in Chapter four. The P_f spectra at 300K are shown in Figure 6.2.

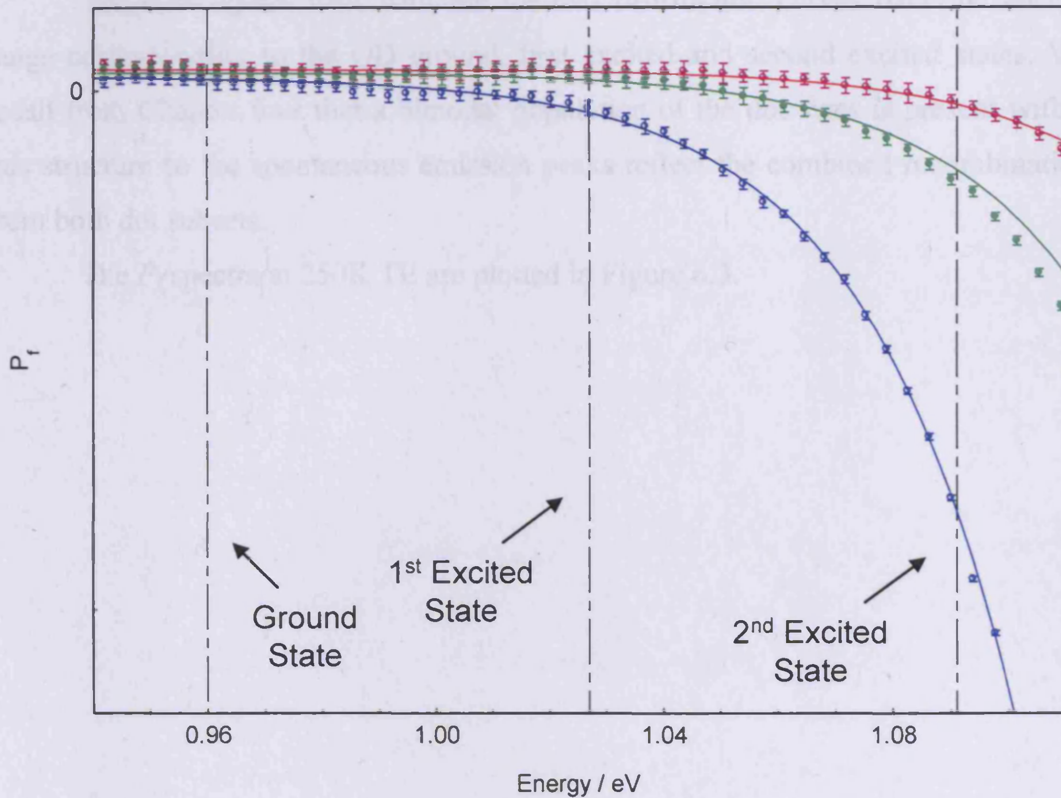

Figure 6.2 – Carrier distribution spectra at 300K TE (data points) and theoretical thermal distribution curves (solid lines) at 267Acm^{-2}(blue), 533 Acm^{-2} (green) and 889 Acm^{-2}(purple). The dashed lines indicate the peak energy of the spontaneous emission for the QD ground, 1st and 2nd excited states. The scale on the y-axis varies between 0.8x10^{26} and -6.0x10^{26}.

Along with the measured data (points), there are dashed lines which correspond to the peak energies of the QD ground, first excited and second excited states, extracted from the measured spontaneous emission data.

The solid lines on the graphs represent P_f for a thermal distribution, formed using Equation 6.2 and the data is fitted to this using the quasi-Fermi level separation obtained from the transparency energy of the measured modal gain. For comparison between the measured data and P_f for a thermal distribution I have used Equation 6.4 in Section 6.2 to convert P_f to P_f^{meas}. The calibration factor (C') was obtained by varying the thermal distribution function to fit the measured data. The error bars shown on this figure, and on subsequent figures in this chapter, were formed using the procedure described in Section 3.6.

The data agrees well with the thermal distribution curves over the energy range corresponding to the QD ground, first excited and second excited states. We recall from Chapter four that a bimodal population of the dot sizes is present within this structure so the spontaneous emission peaks reflect the combined recombination from both dot subsets.

The P_f spectra at 250K TE are plotted in Figure 6.3.

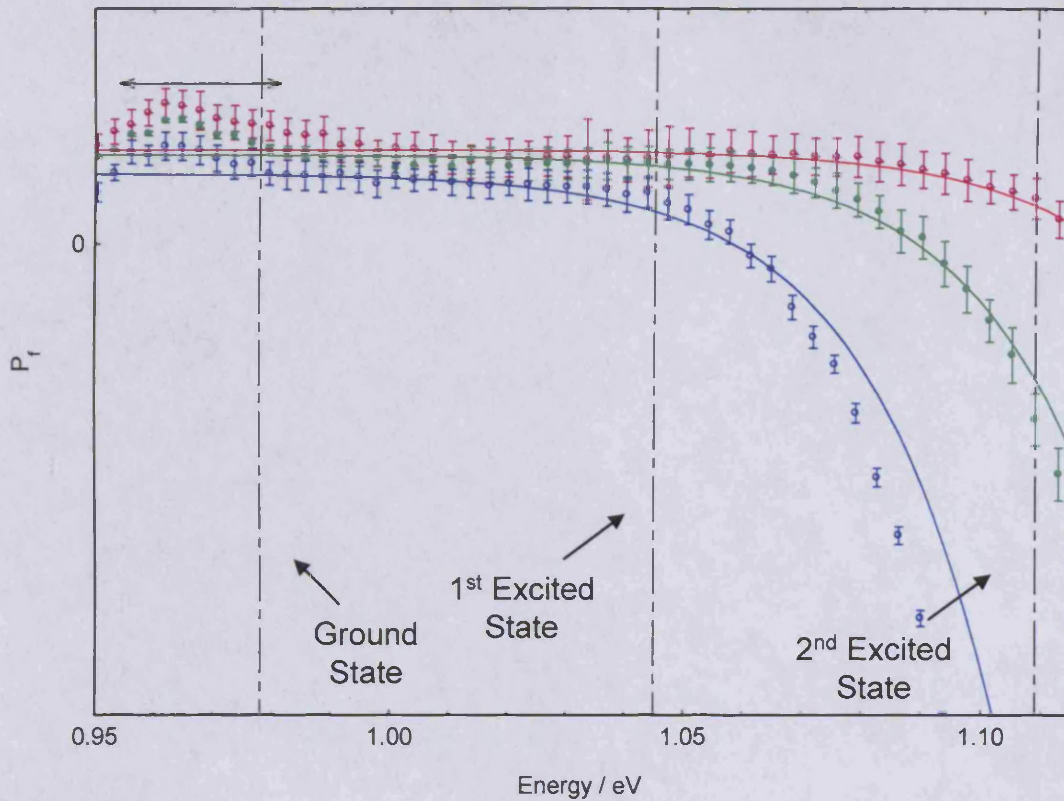

Figure 6.3 – Carrier distribution spectra at 250K TE (data points) and theoretical thermal distribution curves (solid lines) at 267Acm^{-2}(blue), 533 Acm^{-2} (green) and 889 Acm^{-2}(purple). The dashed lines indicate the peak energy of the spontaneous emission for the QD ground, 1st and 2nd excited states. The scale on the y-axis varies between 0.8x10^{26} and -6.0x10^{26}.

The high current density data at 250K agree well with the thermal distribution curves over the energy range corresponding to the dot first and second excited states. At low current density the QD second excited state appears to be at lower inversion than the thermal fit.

At this temperature however a subset of the QD ground states is more inverted than the higher energy dot states and so a common quasi-Fermi level separation cannot be used to describe this system. The region of high inversion occurs to the low energy side of the spontaneous emission peak energy.

When the temperature is lowered further to 200K (Figure 6.4), higher inversion of a subset of the dot ground state is again observed, this time over a larger energy range.

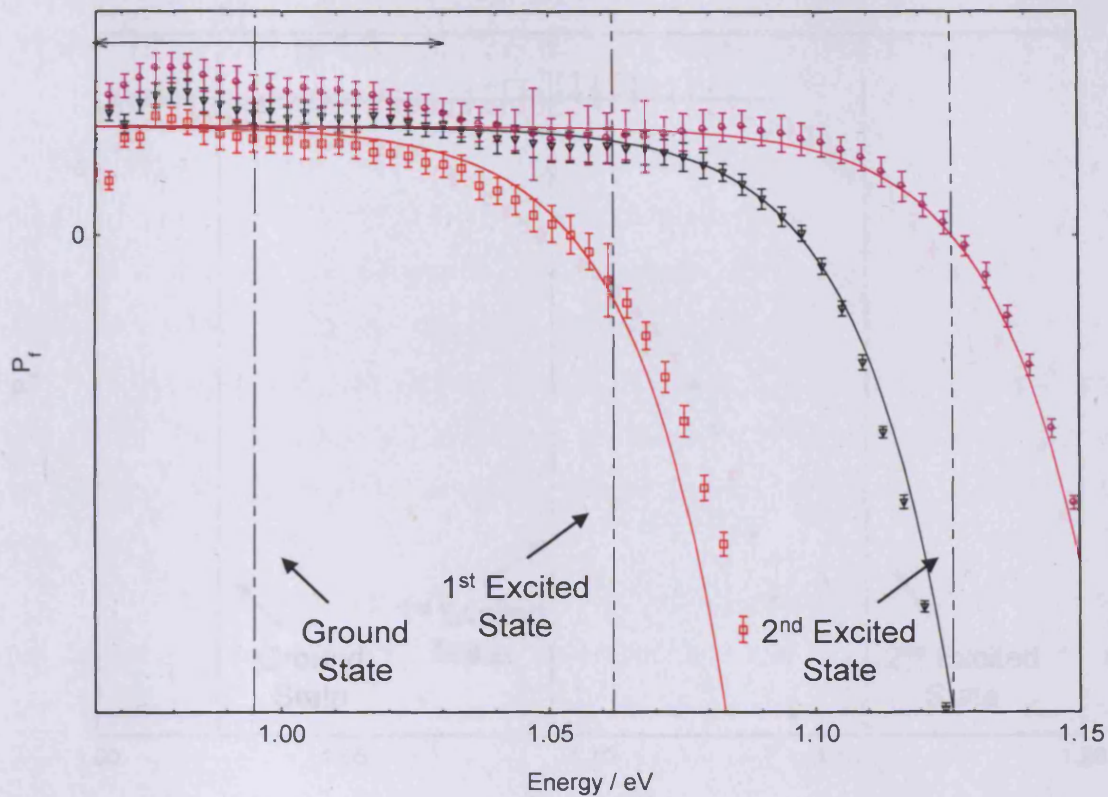

Figure 6.4 – Carrier distribution spectra at 200K TE (data points) and theoretical thermal distribution curves (solid lines) at 178Acm^{-2}(red), 444 Acm^{-2} (black) and 889 Acm^{-2}(purple). The dashed lines indicate the peak energy of the spontaneous emission for the QD ground, 1st and 2nd excited states. The scale on the y-axis varies between 0.9x10^{26} and -2.0x10^{26}.

At 889Acm^{-2} two peaks at 0.979eV and 1.011eV can be resolved within the region of high inversion near the ground state transition. These peaks are separated in energy by approximately 32meV.

Upon lowering the temperature still further to 100K the system becomes completely non-thermal and attempts to fit using Fermi-Dirac statistics do not agree with the experimentally determined data over any energy range (Figure 6.5). We note that the P_f at 711Acm^{-2} has a similar degree of inversion over the whole QD ground and first excited states.

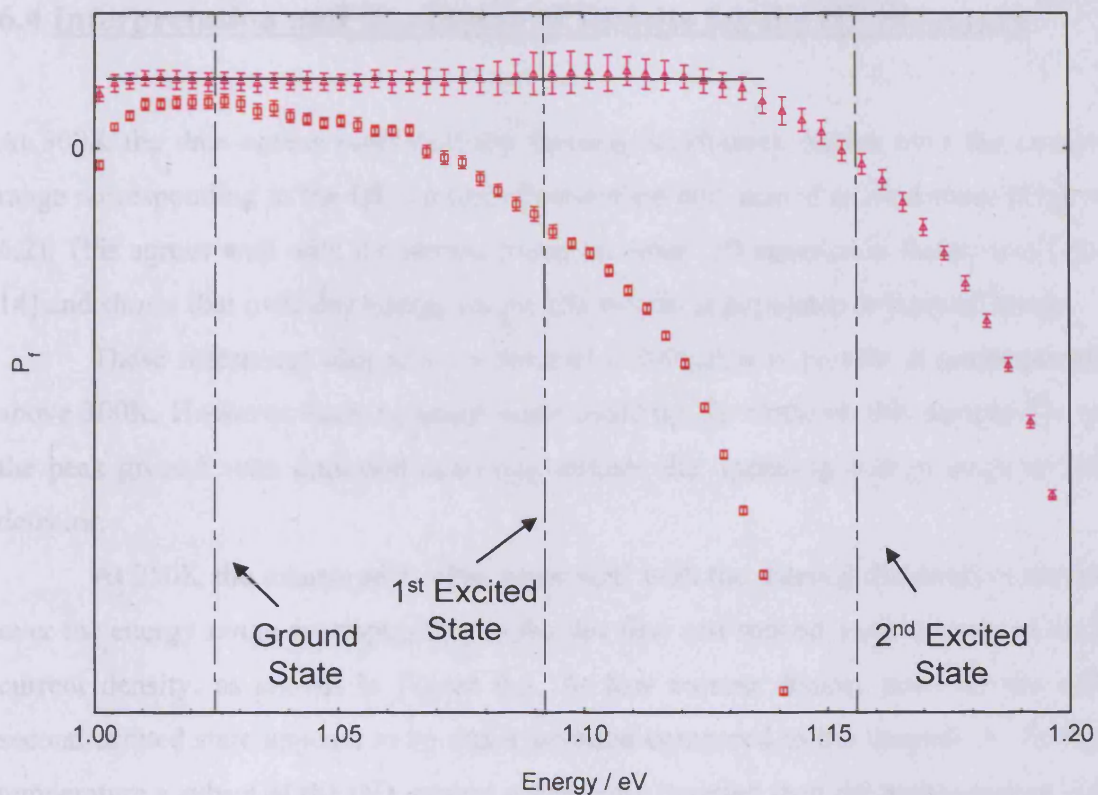

Figure 6.5 – Carrier distribution spectra at 100K TE (data points) at 178Acm^{-2}(red) and 711 Acm^{-2}(pink). The dashed lines indicate the peak energy of the spontaneous emission for the QD ground, first and second excited states. The scale on the y-axis varies between 1.0×10^{26} and -5.0×10^{26}.

6.4 Interpretation and Discussion of Results for the HP Structure

At 300K the data agrees well with the thermal distribution curves over the energy range corresponding to the QD ground, first excited and second excited states (Figure 6.2). This agrees well with the results found on other QD samples in References [12-14] and shows that over this energy range, the system is populated to thermal levels.

These references also show a thermal distribution is present at temperatures above 300K. However these measurements could not be made on this sample due to the peak ground state emission occurring outside the operating energy range of the detector.

At 250K the measured P_f also agree well with the thermal distribution curves over the energy range corresponding to the dot first and second excited states at high current density, as shown in Figure 6.3. At low current density however the QD second excited state appears to be under inverted compared to the thermal fit. At this temperature a subset of the QD ground states more inverted than the higher energy dot states and so a common quasi-Fermi level separation cannot be used to describe this system. The P_f function near the ground state transition is up to 51% more inverted at 889Acm^{-2} than it would be if it were in thermal equilibrium with the higher energy dot states.

Characterisation of this structure in Chapter four revealed a bimodal population in the dot size distribution and so the spontaneous emission transition peaks illustrated in Figure 6.3 contain a contribution from both QD size subsets. The region of higher inversion occurs on the lower energy side of the spontaneous emission peak and could correspond to the large QD subset. The energy range over which the relative over-population exists increases with increasing drive current density from 26meV at 267meV, to 32meV at 889Acm^{-2}.

By comparison with the fitted modal absorption data for this sample (Figure 4.4, Section 4.31), the FWHM of the ground state emission from the large dots (28 ± 4 meV) compares well with the overpopulation peak of 26 to 32meV observed in Figure 6.3. Table 6.1 illustrates the data taken from fitting the modal absorption curve, where the full width half maximum (FWHM) corresponds to 2.35σ, where σ is the magnitude of the inhomogeneous broadening used to fit the measured data.

Dot Subset	Ground State FWHM (meV)	First Excited State FWHM (meV)
Large	28 ± 4	30 ± 4
Small	52 ± 4	44 ± 4

Table 6.1 – Data extracted from fitting the modal absorption curve Figure 4.4, Section 4.3 for comparison with shape changes in carrier distribution spectra.

When the temperature is lowered further to 200K (Figure 6.4), higher inversion of a subset of the dot ground state is again observed, this time over a larger energy range. The P_f near the spontaneous emission ground state transition is up to 56% higher than it would be if they were in thermal equilibrium with the higher energy dot states at this temperature.

At 889Acm^{-2} the energy range over which the overpopulation exists is 74meV. The energy range over which this over population occurs is comparable with the FWHM from the ground state emission, of both QD subsets combined. The tabulated data of Table 6.1 shows the ground state of the small dot size has a FWHM of 52 ± 4 meV, combining this with the ground state emission of the larger dots corresponds to an effective emission energy range of approximately 80meV. We also observe two peaks in this region of high inversion separated in energy by approximately 32meV. This corresponds to the 31meV separation between the ground state transitions from the two dot subsets used to fit the modal absorption curve in Figure 4.4, Section 4.31.

Upon lowering the temperature still further to 100K the system becomes completely non-thermal and attempts to fit using Fermi-Dirac statistics do not agree with the experimentally determined data over any energy range (Figure 6.5). At 711Acm^{-2} the P_f is inverted to the same level for the whole of the QD ground and first excited states. This suggests that at this temperature, the region of high P_f observed at 250K and 200K has extended to include the QD first excited state transitions.

This analysis has shown that at 300K the population of the QD states within a typical QD structure can be described by Fermi-Dirac statistics. As the temperature is lowered the lower energy dot states become more inverted than the higher energy states and eventually this over population extends to encompass the whole of the QD ground and first excited states. The higher inversion can be attributed to a reduced population of wetting layer states and as the temperature is lowered it becomes less likely for carriers to excite out of the dot states and thermally redistribute throughout the ensemble.

6.5 Carrier Distribution within the TI Structure

In this section I present data from the analysis of the carrier distribution within a QD structure which incorporates tunnel injection. In this novel structure, electrons are introduced into the lower energy dot states by phonon-assisted tunnelling from an adjacent injector QW. This design bypasses the higher energy states, in the dots and wetting layer, and the performance limitations associated with them. For such an approach to be beneficial the carriers must recombine before they are able to re-equilibrate throughout the dot ensemble and it is unclear *a priori* to what extent this is true, particularly at high temperature. A schematic illustration of the various states present in the structure is shown in Figure 6.6.

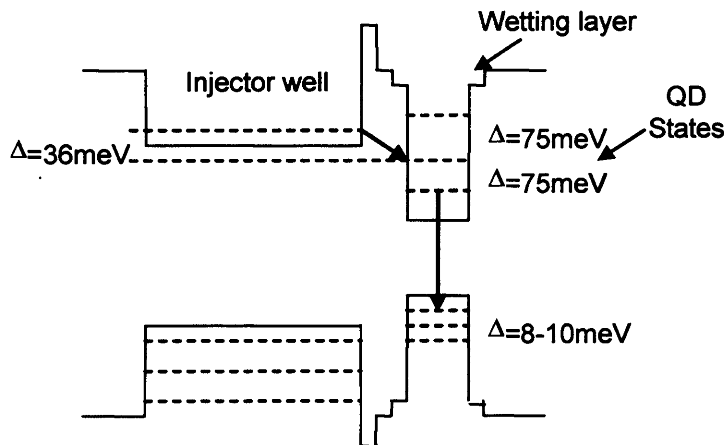

Figure 6.6 – Schematic illustration of the states present in the Ti structure.

It will be shown that in contrast to typical quantum dot lasers, the electron distribution within the dot states cannot be considered thermal, even at room temperature and above. Furthermore, detailed analysis of this distribution reveals features suggesting a selective population of certain size dots within the inhomogeneously broadened quantum dot ensemble. If a thermal distribution were present it would imply that carriers are able to thermalise out of the dot states and redistribute amongst the ensemble i.e. the injection process would not be beneficial.

6.6 Carrier Distribution within the TI Structure – Measured Data

I start by considering the P_f over the whole energy range of the QD and injector well system at 300K (Figure 6.7 (a)) followed by a closer inspection of the P_f over the energy range corresponding to the QD ground and first excited states (Figure 6.7 (b)). The data presented was extracted from the measured spontaneous emission and modal gain data shown in Chapter five. The peak energies of the QD states along with that of the injector well extracted from the spontaneous emission (Figure 5.11(a), Section 5.34) are illustrated by dashed lines and thermal fits are included as solid lines.

The thermal fits were generated using Equations 6.2 and 6.3. Where the fits do not agree with the measured data over the entire system, I conclude it is not in thermal equilibrium. In this case I vary the quasi-Fermi level separation and calibration factor until good agreement is shown over the QD first excited state. The fitting is performed over the QD first excited state due to the wide energy range of data present for this state with a relatively high signal to noise ratio, as compared to the other QD states. This allows comparison between the degree of inversion of this state and the other states within the structure.

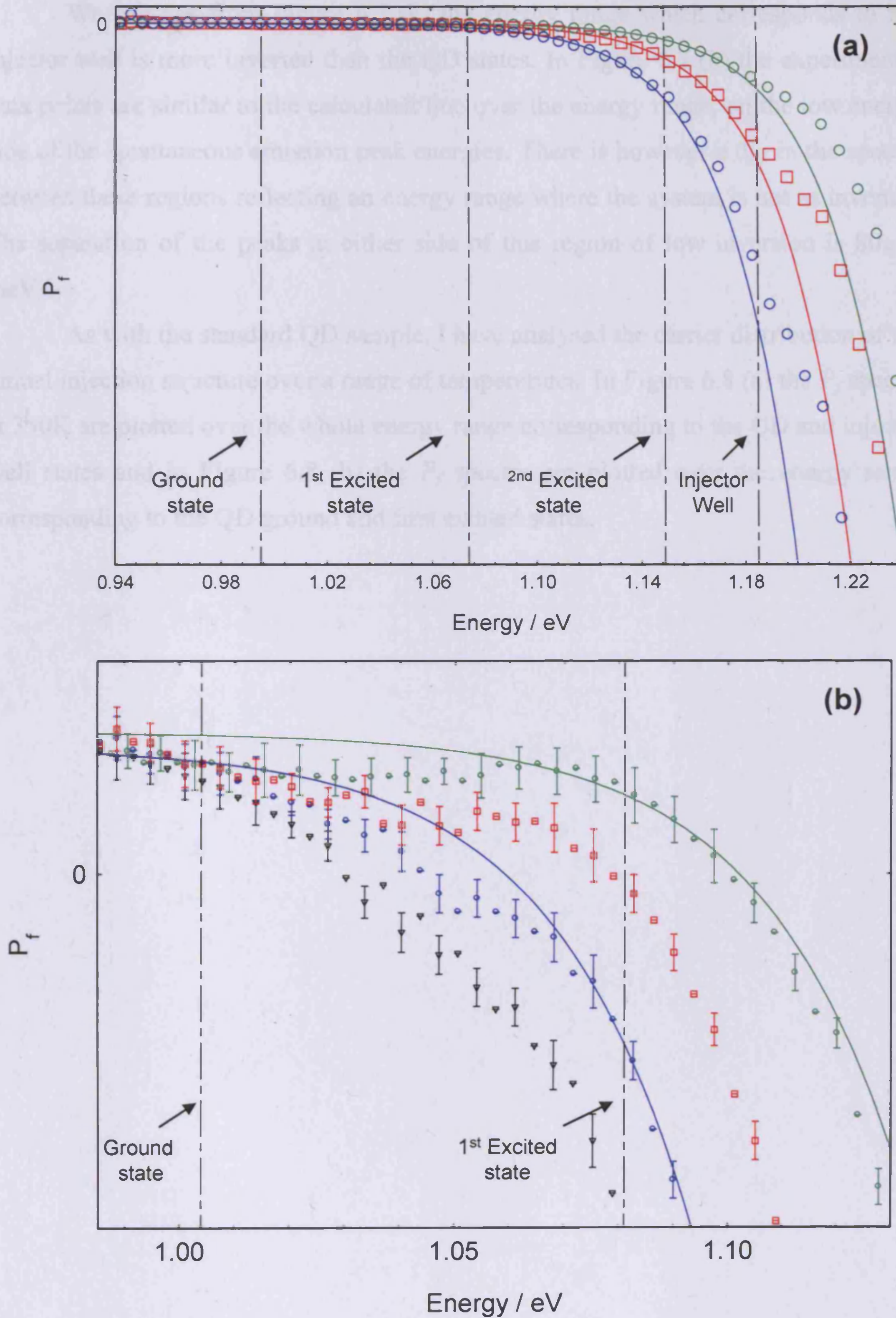

Figure 6.7 – Carrier distribution spectra for the tunnel injection structure at 300K TE for injection current densities 444Acm^{-2} to 1111Acm^{-2} (points), thermal distribution fits (solid lines) and peak energies of the ground and first excited states (dashed lines). (a) Plotted over entire energy range of the QD and injector well system (b) Plotted over the QD ground and first excited state transitions. The scale on the y-axis in (a) varies between 2.0x10^{26} and -6.0x10^{27} and in (b) varies between 3.0x10^{25} and -5.0x10^{25}.

We can see from Figure 6.7 (a) the energy range which corresponds to the injector well is more inverted than the QD states. In Figure 6.7 (b) the experimental data points are similar to the calculated line over the energy range, on the low energy side of the spontaneous emission peak energies. There is however a dip in the spectra between these regions reflecting an energy range where the system is not as inverted. The separation of the peaks at either side of this region of low inversion is 80±10 meV.

As with the standard QD sample, I have analysed the carrier distribution of the tunnel injection structure over a range of temperatures. In Figure 6.8 (a) the P_f spectra at 350K are plotted over the whole energy range corresponding to the QD and injector well states and in Figure 6.8 (b) the P_f spectra are plotted over the energy range corresponding to the QD ground and first excited states.

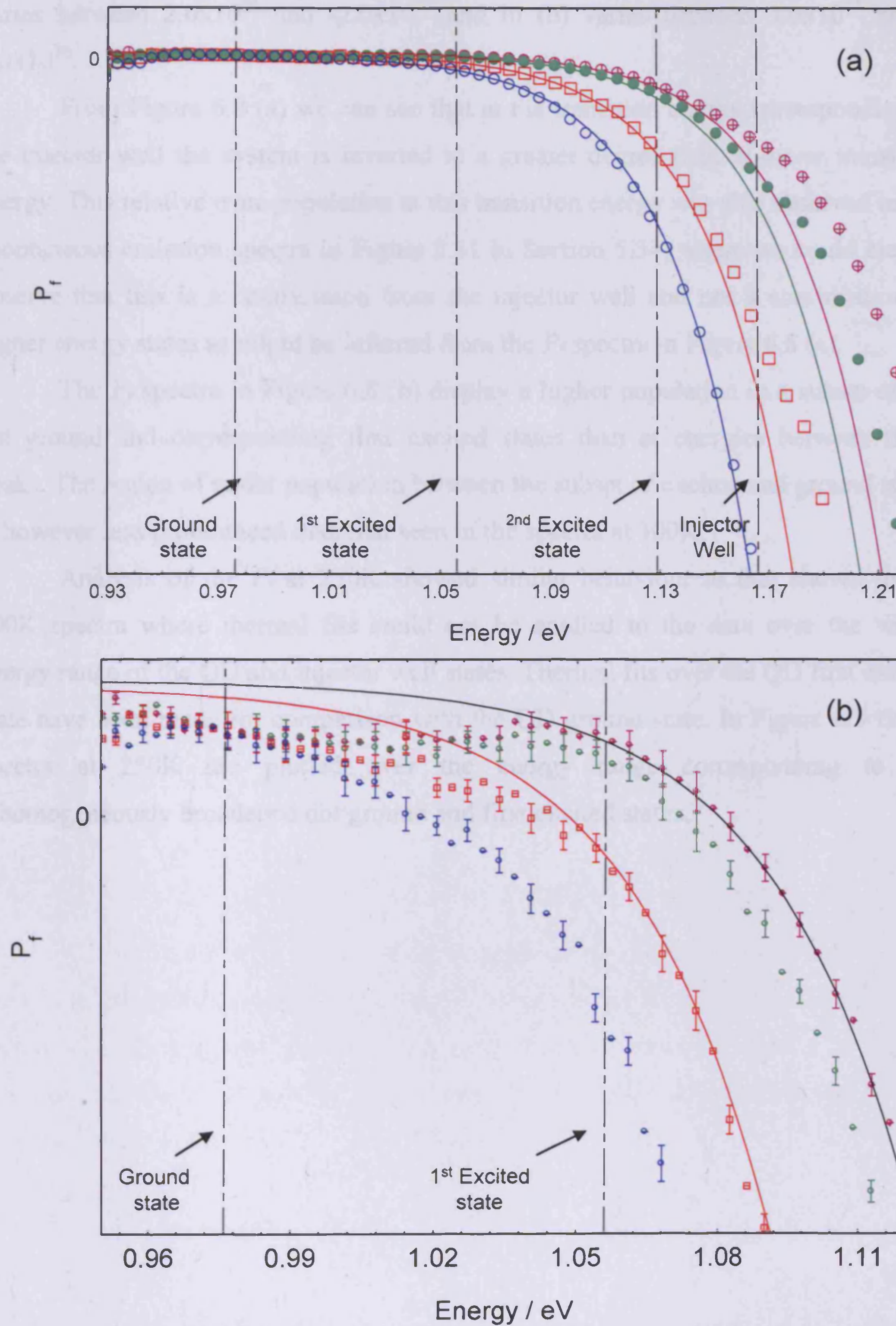

Figure 6.8 – Carrier distribution spectra for the tunnel injection structure at 350K TE for injection current densities 444Acm^{-2} to 1333Acm^{-2} (points), thermal distribution fits (solid lines) and peak energies of the ground and first excited states (dashed lines). (a) Plotted over entire energy range of the QD and injector well system (b) Plotted

over the QD ground and first excited state transitions. The scale on the y-axis in (a) varies between 2.0×10^{26} and -2.0×10^{27} and in (b) varies between 3.0×10^{25} and -8.0×10^{26}.

From Figure 6.8 (a) we can see that at the transition energy corresponding to the injector well the system is inverted to a greater degree than at lower transition energy. This relative over-population at this transition energy was also observed in the spontaneous emission spectra in Figure 5.11 in Section 5.34, where we could clearly observe that this is a contribution from the injector well and not a combination of higher energy states as might be inferred from the P_f spectra in Figure 6.8 (a).

The P_f spectra in Figure 6.8 (b) display a higher population in a subset of the dot ground and corresponding first excited states than at energies between these peaks. The region of under population between the subset of excited and ground states is however less pronounced than that seen in the spectra at 300K.

Analysis of the P_f at 250K showed similar behaviour to that shown in the 300K spectra where thermal fits could not be applied to the data over the whole energy range of the QD and injector well states. Thermal fits over the QD first excited state have been made for comparison with the QD ground state. In Figure 6.9 the P_f spectra at 250K are plotted over the energy range corresponding to the inhomogeneously broadened dot ground and first excited states.

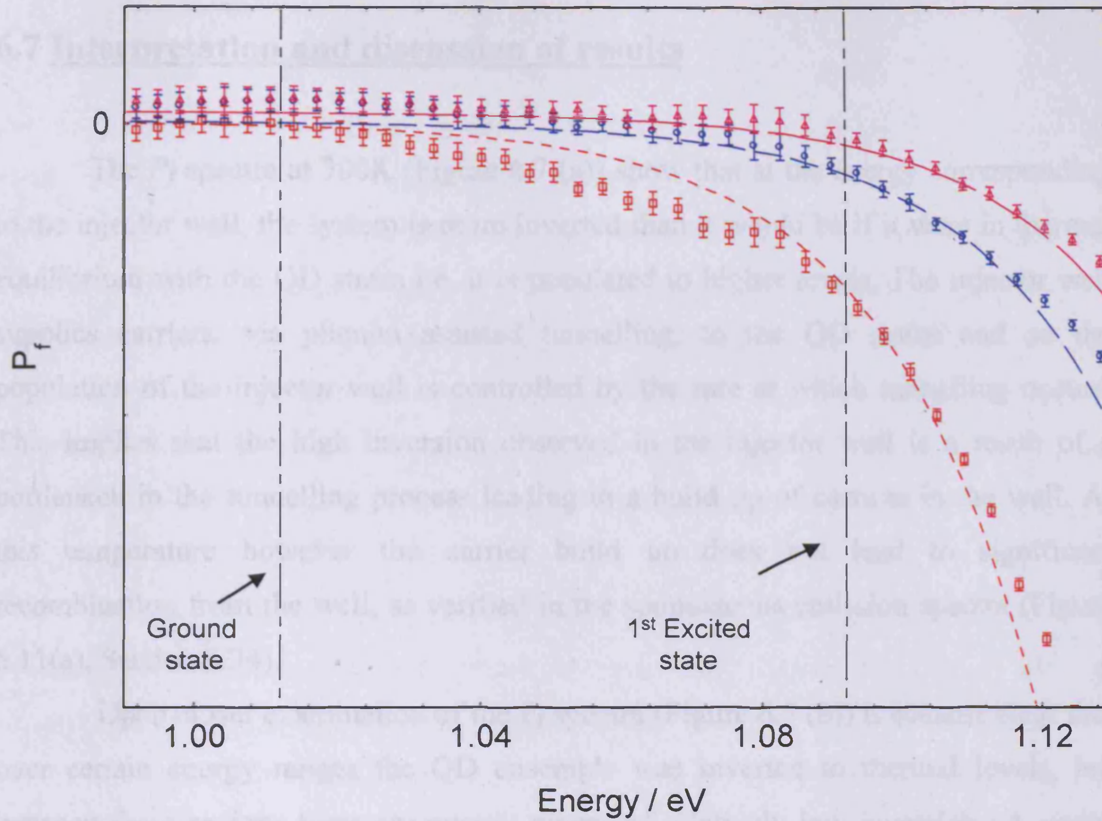

Figure 6.9 – Carrier distribution spectra for the tunnel injection structure ate 250K TE for injection current densities $333Acm^{-2}$ to $889Acm^{-2}$ (points), thermal distribution fits (solid lines) and peak energies of the ground and first excited states (dashed lines). The scale on the y-axis varies between $1.0x10^{26}$ and $-5.0x10^{26}$.

At low injection levels the peak energies of the dot ground and first excited states are inverted to similar levels. As with the data at 300K and 350K there is a region of low inversion between these peak energies. At higher levels of current injection the whole of the QD ground and first excited states appears inverted to thermal levels.

6.7 Interpretation and discussion of results

The P_f spectra at 300K (Figure 6.7 (a)) show that at the energy corresponding to the injector well, the system is more inverted than it would be if it were in thermal equilibrium with the QD states i.e. it is populated to higher levels. The injector well supplies carriers, via phonon assisted tunnelling, to the QD states and so the population of the injector well is controlled by the rate at which tunnelling occurs. This implies that the high inversion observed in the injector well is a result of a bottleneck in the tunnelling process leading to a build up of carriers in the well. At this temperature however the carrier build up does not lead to significant recombination from the well, as verified in the spontaneous emission spectra (Figure 5.11(a), Section 5.34).

Upon closer examination of the P_f spectra (Figure 6.7 (b)) it became clear that over certain energy ranges the QD ensemble was inverted to thermal levels, but between these regions there are energy ranges of relatively low inversion i.e. under population. The energy separation between the regions of high P_f is (80 ± 10) meV and corresponds to the separation between the ground and excited states as deduced from the measured spontaneous emission data shown in Figure 5.11, Section 5.34. The amplitude of the dip increases as the level of carrier injection is increased. I believe this suggests that the injection process couples carriers into a subset of dots of a specific size and that carriers are able to move between excited and ground states of individual dots in this subset, but that dots with a different size are under populated.

This supports predictions by Asryan et al. (2001) [15], "tunnel injection inherently leads to an effective narrowing of the inhomogeneous linewidth by selective injection into the QDs of the 'right' size. This theoretical model of a tunnel injection structure also predicts that such a structure will show almost temperature independent threshold current density, which is in agreement with the results produced in Chapter five of this thesis.

The region of low inversion at 300K would also be present between the inhomogeneously broadened QD first excited and second excited states. Upon closer examination of the spectra this effect is not observed although this could be a result of the relative under population of the whole second excited state as a result of the tunnelling process.

We observe in the spontaneous emission spectra (Figure 5.11, Section 5.34) that the spectral shape indicates the presence of the QD second excited state however, recombination from it is not significant.

The P_f spectra at 350K (Figure 6.8 (a)) show a region of higher inversion over the energy range corresponding to the injector well. This is similar to that seen at 300K however at this temperature it is far more significant. This agrees well with the increased radiative recombination from the injector well observed in the spontaneous emission spectra (Figure 5.11(c), Section 5.34) at 350K. This is attributed to an increased electron population in the QD first excited state blocking the transfer of carriers from the injector well.

Considering the energy range corresponding to the inhomogeneously broadened dot ground and first excited states in more detail (Figure 6.8 (b)), we observe similar characteristics to that seen at 300K. There is a region of low inversion between the subset of excited and ground states. This is however less pronounced than that seen in the spectra at 300K. This is presumably because at 350K the thermal redistribution process is more efficient. The ground state subset is also slightly under inverted compared to the excited state which could be a result of increase thermal excitation at this temperature.

At 250K the injector well was populated to similar levels to that seen at 350K. Upon close examination of the QD ground and first excited states (Figure 6.9) we observe at low injection, the same region of low inversion between the similarly inverted subset of ground and first excited states as that seen in the 300K Data. At higher levels of current injection the whole of the QD ground and first excited states appears populated to thermal levels.

Comparison with the data obtained for the high performance QD laser shows us at lower temperatures, the QD ground state is overpopulated. At 250K in the TI structure the observed thermal population could be attributed to carriers injected into the under-populated dots all occupying the ground state transition masking the selective population of the dot ensemble seen in the lower current density data.

The analysis of the P_f spectra for the tunnel injection structure has revealed a selective population process in which dots of a particular size are preferentially populated. This can be attributed to the resonant tunnelling process as analysis of the typical QD structure revealed no such features. The high inversion of a subset of the QD ground states at low temperature seen in the typical structure was also not observed in the tunnel injection structure. This suggests it is a result of reduced interaction between the wetting layer and the lower energy dot states at this temperature.

6.8 Summary

I have analysed the carrier distribution in both a typical HP quantum dot laser and a laser which utilises TI, over a range of temperatures. The carrier distribution for a typical HP QD laser shows that it is populated to thermal levels at 300K but as the temperature is lowered, the ground state becomes over populated compared to the other dot states. The degree of over population increases both with drive current density and with decreasing temperature.

At 250K the carrier distribution spectra reveal an over population of the ground state, over the energy range corresponding to emission from the larger dot subset within the ensemble. When the temperature is lowered to 200K the over population of the QD ground states extends to include both dot subsets within the ensemble. Finally at 100K the system becomes completely non-thermal at low injection levels. As the current injection level is raised it becomes clear that the ground and first excited states of both dot subsets are inverted to similar levels. This suggests the over population has extended to include the whole of the QD ensemble ground and first excited states.

I have shown that the TI structure injects electrons into a subset of the lower energy dot states where the injector well controls the operation of the device. At 300K the carrier distribution function is populated to thermal levels over an energy range corresponding to a subset of the quantum dot ground and first excited states. Between this there is a region of under populated states suggesting dots of a particular size within the ensemble are preferentially populated leading to a reduced spectral broadening of the emission.

At 350K the selective population is still present however it is less pronounced. This is attributed to more efficient thermal distribution of electrons at this temperature. The injector well is also more highly populated at this temperature which can be attributed to the increased number of carriers in the QD first excited state making the tunnelling process less efficient. At 250K the selective population can still be observed in the carrier distribution spectra at low levels of current injection. At higher injection the over population of the ground state which is observed in the spectra masks the selection process.

7. Summary Conclusions and Further Work

7.1 Summary and Conclusions

In this thesis I have produced results to show how carriers populate electronic states of InAs quantum dot (QD) laser diodes which operate near 1.3μm, especially those which incorporate tunnel injection (TI). I have also used a variety of techniques to characterise a high performance (HP) QD structure and a tunnel injection structure.

The vast majority of the results presented in this thesis were taken using the segmented contact method. I used this technique to produce modal absorption, modal gain and spontaneous emission spectra as a function of photon energy. These in turn were used to produce population inversion spectra, which are related to the carrier occupation of the various states within the systems tested.

The characterisation of the high performance QD laser revealed a bimodal dot population with narrow inhomogeneous linewidths of 12±2meV and 22±2meV, for the large and small dot subsets respectively. This showed the structure was a good comparator to the TI QD structure which showed similar characteristics.

The spontaneous emission peak transition energy of both structures did not change with increasing current injection. It remains unclear whether this is a result of the level of pumping or the carrier distribution present in the two structures. When comparing the spontaneous emission for the two structures at equal quasi-Fermi level separation, the carrier population of the HP QD structure was more significant in the higher energy dot states. This, along with the relatively small amount of recombination observed from the QD second excited state in the tunnel injection structure, showed that tunnelling process was working well and that thermalisation out of the lower energy dot states was not significant for temperatures up to 300K.

Comparisons between the modal gain of the two structures revealed they both suffer from gain saturation effects which reduced at lower temperature. This suggested the saturation was a result of thermalisation out of the QD states. The high performance QD modal gain did however saturate at a lower value when the temperature was lowered from 200K to 100K. This was explained by considering that, within this QD structure, a bimodal dot size distribution exists.

The wetting layer and dot states are decoupled at 100K and carriers captured by the dots can no longer redistribute themselves to more favourable states via the wetting layer. In this situation, only dots which contain both an electron and a hole will contribute to the modal gain leading to an overall reduction in the saturated value.

I showed that the TI laser has higher differential and saturated ground state gain. As the carriers in the tunnel injection structure bypass both the wetting layer and higher energy dot states and the carriers in the standard sample do not, the higher differential gain provided that the relaxation processes for the carriers through the wetting layer and higher energy QD states, limit the differential gain in HP QD lasers. As the TI structure only shows a small improvement in these characteristics this suggests the relaxation from the QD first excited to ground state is the main limiting factor on the performance of both devices.

In my analysis of the carrier distribution within the HP QD structure I found that at 300K the QD states can be described by Fermi-Dirac statistics (thermally distributed). This suggests that at this temperature, carriers are able to redistribute amongst the spatially isolated QDs at a faster rate than they can recombine.

As the temperature is lowered the electron distribution becomes clearly non-thermal, as seen at 250K where a subset of the QD ground states is more inverted than the other QD states. At 200K the range of high inversion extended to encompass the whole of the QD ground states within the ensemble and at 100K the whole of the QD ground and first excited states is highly inverted. The higher inversion can be attributed to a reduced population of wetting layer states and as the temperature is lowered it becomes less likely for carriers to excite out of the dot states and thermally redistribute throughout the ensemble.

The TI structure was shown to exhibit unique features in its carrier distribution as compared to the HP structure. At 300K the carrier distribution function is only populated to thermal levels over an energy range corresponding to a subset of the QD ground and first excited states. Between this there is a region of under populated states shown by a region of low inversion. This suggests dots of a particular size within the ensemble are preferentially populated by the resonant tunnelling process. This results in a reduced spectral broadening of the emission from the QD ensemble.

At 350K the selective population can still be observed, however it is less pronounced. This is attributed to more efficient thermal distribution of electrons at this temperature. The injector well is also more highly populated which can be attributed to the increased number of carriers in the QD first excited state making the tunnelling process less efficient. At 250K the selective population can still be observed in the carrier distribution spectra at low levels of current injection. At higher injection the over population of the ground state which is observed in the spectra masks the selection process.

7.2 Further Work

In this thesis I have analysed the carrier distribution within long wavelength QD laser diodes including a structure which incorporates TI. I believe the tunnel injection QD lasers have the potential to overcome many of the drawbacks currently associated with conventional QD lasers and so I focus my discussion on this type of structure.

I have used a HP QD laser with similar levels of inhomogeneous broadening to reveal the benefits of the tunnel injection process. This sample was chosen due to the lack of a suitable comparator sample.

In future growths of a similar structure a true comparator could be grown and all the performance enhancements and weaknesses of the tunnelling process would be revealed. The work in this thesis suggests the performance of the TI structure is limited by the tunnelling into the QD first excited state. If a structure could be designed where electrons tunnel into the lasing state, the lasers at 1.3μm might show similar improvements to that shown for lasers operating at 1.0μm by Fathpour et al. (2005) [72].

An interesting addition to the work shown in this thesis would be to perform time-resolved measurements [34, 82] on the tunnel injection samples to provide insight into the relaxation rates throughout the structure. The structure tested also incorporated P-doping and it is unclear whether the level of doping has been optimised.

The optical fibres currently being developed for the telecommunications industry require laser sources up to 1.7μm [83] so it would be interesting to see if the tunnel injection structure could be modified to emit at even longer wavelengths.

7.3 References

1. Ledentstov N N, "Long-wavelength quantum-dot lasers on GaAs substrates: from media to device concepts", *IEEE Journal of Selected Topics in Quantum Electronics*, 8, 5, P1015-1024 (2002).
2. Mikhrin S S, Kovsh A R, Krestnikov I L, Kozhukhov A V , Livshits D A , Ledentsov N N, Shernyakov Y M , Novikov I I, Maximov M V, Ustinov V M and Alferov Z I, "High power temperature-insensitive 1.3 µm InAs/InGaAs/GaAs quantum dot lasers", *Semiconductor Science and Technology*, 20, 5, P340-342 (2005).
3. Shchekin O B, Deppe D G, "1.3µm InAs quantum dot laser with T_o = 161K from 0 to 80°C", *Applied Physics Letters*, 80, 18, P3277-3279 (2002).
4. Mi Z, Bhattacharya P, and Fathpour S, "High-speed 1.3µm tunnel injection quantum-dot lasers", *Applied Physics Letters*, **86**, 153109 (2005).
5. Lott J A, Ledentsov N N, Ustinov V M, Maleev N A, Zhukov A E, Kovsh A R, Maximov M V, Volovik B V, Alferov Z I and Bimberg D, "InAs-InGaAs quantum dot VCSELs on GaAs substrates emitting at 1.3µm", *IEE Electronics Letters*, 36, 16, P1384-1385 (2000).
6. Yamamoto N, Akahane K, Gozu S, Ohtani N, "Over 1.3 /spl mu/m CW laser emission from InGaSb quantum-dot vertical-cavity surface-emitting laser on GaAs substrate", *IEEE Electronics Letters*, 40, 18, P1120-1121 (2004).
7. Asada M, Miyamoto Y and Suematsu Y, "Gain and the threshold of three-dimensional quantum-box lasers", *IEEE Journal of Quantum Electronics*, 22, 9, P1915-1921 (1986).
8. Arakawa Y and Sakaki H, "Multi dimensional quantum well laser and temperature dependence of its threshold current" *Applied physics letters*, 40, P939-941(1982).
9. Asryan L V and Suris R A, "Inhomogeneous line broadening and the threshold current density of a semiconductor quantum dot laser", *Semiconductor Science and Technology*, 11, P554-567 (1996).
10. Deppe D G, Huang H and Shchekin O B, "Modulation characteristics of quantum-dot lasers: the influence of p-type doping and the electronic density of states on obtaining high speed", *IEEE Journal of Quantum Electronics*, 38, 12, P1587-1593 (2002)

11. Matthews D R, Summers H D, Smowton P M, Hopkinson M, "Experimental investigation of the effect of wetting-layer states on the gain–current characteristic of quantum-dot lasers", *Applied Physics Letters*, 81, 26, P4904-4906 (2002).
12. Summers HD, Thomson J, Smowton PM, Blood P, and Hopkinson M, "Thermodynamic balance in quantum dot lasers", *Semiconductor Science and Technology,* 16, 140-143 (2001).
13. Zhang Y C, Huang C J, Liu F Q, Xu B, Wu J, Chen Y H, Ding D, Jiang W H, Ye X L, and Wang Z G, "Thermal redistribution of photocarriers between bimodal quantum dots", *Journal of Applied Physics*, 90, 4, P1973-1976 (2001).
14. Smowton P M, Sandall I C, Mowbray D J, Liu H Y and Hopkinson M, "Maximising the gain: optimising the carrier distribution in InGaAs quantum dot lasers", *Proceedings of SPIE: Physics and Simulation of Optoelectronic Devices XV*, 6468, 646817 (2007).
15. Asryan LV and Luryi S, "Tunnelling-injection quantum-dot laser: Ultrahigh temperature stability", *IEEE Journal of Quantum Electronics* 37, 7, P905-910 (2001).
16. Fiore A, Markus A, "Differential Gain and Gain Compression in Quantum-Dot Lasers", IEEE Journal of Quantum Electronics, 43, 3, P287-294 (2007).
17. Blood, P, Lewis G M, Smowton P M, Summers H, Thomson J and Lutti J, "Characterization of Semiconductor Laser Gain Media by the Segmented Contact Method", *IEEE Journal of Selected Topics in Quantum Electronics,* **9,** 5 P1275-1282 (2003).
18. Dingle R and Henry C H, "Quantum effects in heterostructure lasers" US patent No. 3982207 (1976).
19. Goldstein L, Glas F, Marzin J Y, Charasse N and Le Roux G, "Growth by molecular beam epitaxy and characterisation of InAs/GaAs strained-layer superlattices", *Applied Physics Letters*, 47, 10, P1099-1101 (1985).
20. Ustinov V M, Zhukov A E, Egorov A Y, Maleev N A, "Quantum dot lasers", *Oxford University Press*, ISBN: 0198526792 (2003).
21. Bimberg D, Grundmann M, Ledentsov N N, "Quantum dot heterostructures", *Wiley Publications*, ISBN: 0471973882 (1999).

22. Leonard D, Krishnamurthy M, Reaves C M, Denbaars S P and Petroff P M, "Direct formation of quantum-sized dots from uniform coherent islands of InGaAs on GaAs surfaces", *Applied Physics letters*, 63, 23, P3203-3205 (1993).

23. Kirstaedter N, Ledentsov N N, Grundmann M, Bimberg D, Ustinov V M, Ruvimov S S, Maximov M V, Kop'ev P S, Alferov Z, Richter U, Werner P, Gdsele U and Heydenreich J, "Low threshold, large T_0 injection laser emission from (InGa)As quantum dots", *IEE Electronics Letters*, 30, 17, P1416-1417 (1994).

24. Hatami F, Masselink W T, and Schrottke L, "Radiative recombination from InP quantum dots on (100) GaP", *Applied Physics Letters*, 78, 15, P2163-2165 (2001).

25. Fu H and Zunger A, "InP quantum dots: Electronic structure, surface effects, and the red shifted emission", *Physical Review B*, 56, 3, P1496-1508 (1997).

26. Sopanen M, Xin H P, and Tu C W, "Self-assembled GaInNAs quantum dots for 1.3 and 1.55 μm emission on GaAs", *Applied Physics Letters*, 76, 8, P994-996 (2000).

27. Liu C Y, Yoon S F, Sun Z Z, and Yew K C, "High-temperature operation of self-assembled GaInNAs/GaAsN quantum-dot lasers grown by solid-source molecular-beam epitaxy", *Applied Physics Letters*, 88, 081105 (2006).

28. Stangl J, Holy V, Bauer G, "Structural properties of self-organised nanostructures", *Reviews of Modern Physics*, 76, P725-783 (2004).

29. Fox M, "Optical properties of solids", *Oxford University Press*, ISBN: 0198506139 (2001).

30. Vurgaftman I, Meyer J R and Ram-Mohan L R, "Band parameters for III-V semiconductors and their alloys", *Journal of Applied Physics: Applied Physics Review*, 89, 11, P5815-5875 (2001).

31. Mowbray D J, Skolnick M S, "New physics and devices based on self-assembled semiconductor quantum dots", *Journal of Physics D: Applied Physics*, 38, P2059-2076 (2005).

32. Cho A Y, "Growth of periodic structures by the molecular beam method", *Applied Physics Letters*, 19, 11, P467-468 (1971).

33. Siegman A E, "Lasers", *University Science Books*, ISBN: 0935702-11-33 (1986).

34. Borri P, Langbein W, Schneider S, Woggon U, Sellin R L, Ouyang D, and Bimberg D, "Ultralong Dephasing Time in InGaAs Quantum Dots", *Physical Review Letters*, 87, 15, 157401 (2001).

35. Kovsh A R, Zhukov A E, Egorov A Y, Ustinov V M, Shernyakov Y M, Maximov M V, Volovik V V, Tsatsul'nikov A F, Musikhin Y V, Ledentsov N N, Kop'ev P S, Bimberg D, Alferov Z I, "Molecular beam epitaxy (MBE) growth of composite (In,Al)As/(In,Ga)As vertically coupled quantum dots and their application in injection lasers", *Journal of Crystal Growth*, 201-202, P1117-1120 (1999).

36. Mikhrin S S, Zhukov A E, Kovsh A R, Maleev N A, Ustinov V M, Shernyakov Y M, Soshnikov I P, Livshits D A, Tarasov I S, Bedarev D A, Volovik B V, Maximov M V, Tsatsulnikov A F, Ledentsov N N, Kop'ev P S, Bimberg D and Alferov Z I, "0.94 μm diode lasers based on Stranski-Krastanow and sub-monolayer quantum dots", *Semiconductor Science and Technology*, 15, 11, P1061-1064 (2000).

37. Sandall I C, "The characterisation of In(Ga)As quantum dot lasers", Thesis (Ph.D.) - Cardiff University, 2006.

38. Einstein A, "On the Quantum theory of radiation", *Physikalische Zeitschrift*, 18, 121 (1917). Translated in: Haar D T, "The old quantum theory", *Pergamon Press*, (1967).

39. Coldren LA, Corzine SW, "Diode lasers and photonic integrated circuits", *Wiliey-Interscience Publications*, 10th edition, ISBN 0471118753 (1995).

40. Chuang S L, "Physics of optoelectronic devices", *Wiley-Interscience Publications*, ISBN: 0471109398 (1995).

41. Beiser A, "Concepts of modern physics", McGraw-Hill Publishers, Sixth Edition, ISBN:0072448482 (2003).

42. Thomson J D, "Optical gain studies in quantum confined structures", *Thesis*, Cardiff University (2000).

43. Blood P, "On the dimensionality of optical absorption, gain and recombination in quantum-confined structures", *IEEE Journal of Quantum Electronics*, 36, 3, P354-362 (2000).

44. Tessler N and Eisenstein G, "On Carrier Injection and Gain Dynamics in Quantum Well Lasers", *IEEE Journal of Quantum Electronics*, 29, 6, P1586-1595 (1993).

45. Grundmann M, Bimberg D, "Theory of random population for quantum dots", *Physical Review B*, 55, P9740-9745 (1997).

46. Osborne S, Blood P, Smowton P, Lutti J, Xin YC, Stintz A, Huffaker D, and Lester LF, "State filling in InAs quantum dot laser structures", *IEEE Journal of Quantum Electronics*, 40, P1639-1645 (2004).

47. Markus A, Chen J X, Gauthier-Lafaye O, Provost J G, Paranthoën C, and Fiore A, "Impact of Intraband Relaxation on the Performance of a Quantum-Dot Laser", *IEEE Journal of Quantum Electronics*, 9, 5, P1308-1314 (2003).

48. Zhukov A E, Kovsh A R, Egorov A Yu, Maleev N A, Ustinov V M, Volovik B V, Maksimov M V, Tsatsul'nikov A F, Ledentsov N N, Shernyakov Yu M , Lunev A V, Musikhin Yu G, Bert N A, Kop'ev P S and Alferov Zh I, "Photo-and electroluminescence in the 1.3-μm wavelength range from quantum-dot structures grown on GaAs substrates", *Semiconductors*, 33, 2, P153-156 (1999).

49. Thomson J D, Summers H D, Hulyer P J, Smowton P M, Blood P, "Determination of single-pass optical gain and internal loss using a multi-section device", 75(17), P2527-2529, (1999).

50. Hakki B W and Paoli T L, "CW degradation at 300K of GaAs double heterostructure junction lasers—II: Electronic gain", *Journal of applied Physics,* 44, 9, P4113–4119 (1973).

51. Oster A, Erbert G, Wenzel H, "Gain spectra measurements by a variable stripe length method with current injection", *IEE Electronics letters*, 33, 10, P864-866 (1997).

52. Lee J R, Lu C R; Lee W I, Lee S C, "Investigation of populated InAs/GaAs quantum dots by photoluminescence and photoreflectance", *Physica E*, 25, 4, P562-568 (2005).

53. Blood P, Post graduate lecture notes, Cardiff University, (2005).

54. Wood S A, Molloy C H, Smowton P M, Blood P, and Button C C, "Minority Carrier Effects in GaInP Laser Diodes", *IEEE Journal of Quantum Electronics*, 36, 6, P742-750 (2000).

55. Sandall I C, Smowton P M, Walker C L, Badcock T, Mowbray D J, Liu H J and Hopkinson M, "The effect of P doping in InAs quantum dot lasers", *Applied physics letters*, 88, 111113 (2006).

56. Bimberg, D and Ledenstov, N, "Quantum dots: lasers and amplifiers", *Journal of Physics: Condensed Matter*, 15, P1063-1076 (2003).

57. Walker CL, Sandall IC, Smowton PM, Sellers IR, Mowbray DJ, Liu HY, Hopkinson M, "The role of high growth temperature GaAs spacer layers in 1.3μm In(Ga)As quantum-dot lasers", *IEEE Photonics Technology Letters*, Vol 17, 10, P2011-2013 (2005).

58. Salhi A, Martiradonna L, Visimberga G, Tasco V, Fortunato L, Todaro M T, Cingolani R, Passaseo A De Vittorio M, "High-modal gain 1300nm In(Ga)As-GaAs quantum dot lasers", *IEEE Photonics Technology Letters*, Vol 18, 16, P1735-1737 (2006).

59. Salhi A, Fortunato L, Martiradonna L, Todaro M T, Cingolani R, Passaseo A, De Vittorio M, "High efficiency and high modal gain InAs/InGaAs/GaAs quantum dot lasers emitting at 1300nm", *Semiconductor Science and Technology*, 22, P396-398 (2007).

60. Harris JR, "GaInNAs long-wavelength lasers: progress and challenges", *Semiconductor Science and Technology*, 17, 8, P880-891 (2002).

61. Park G , Shchekin O B, Huffaker D L, and Deppe D G, "Lasing from InGaAs/GaAs quantum dots with extended wavelength and well-defined harmonic-oscillator energy levels" *Applied Physics Letters*, 73, 23, P3351-3353 (1998).

62. Huffaker H, Park G, Zou Z, Shchekin O B, Deppe DG, "1.3μm room-temperature GaAs-based quantum-dot laser", *Applied Physics Letters*, 73, 18, P2564-2566 (1988).

63. Mukai K, Nakata Y, Otsubo K, Sugawara M, Yokoyama N, and Ishikawa H, "1.3-μm CW lasing of InGaAs-GaAs quantum dots at room temperature with a threshold current of 8mA", *IEEE Photonics Technology Letters*, 11, 10, P1205-1207 (1999)

64. Pask H, "Model for localised recombination in quantum dots", PhD thesis, Cardiff University (2006).

65. Liu H Y, Sellers I R, Gutierrez M, Groom K M, Soong W M, Hopkinson M, David J P R, Beanland R, Badcock T J, Mowbray D J, "Influences of the spacer layer growth temperature on multilayer InAs/GaAs quantum dot structures", *Journal of Applied Physics*, Vol. 96, 4, P1988-1992 (2004).

66. Anders S, Kim C S, Klein B, Keller M W, Mirin R P and Norman A G, "Bimodal size distribution of self-assembled $In_xGa_{1-x}As$ quantum dots", *APS Physical Review B*, 66, 125309 (2002).

67. Yang T, Tsukamoto S, Tatebayashi J, Nishioka M and Arakawa Y, "Improvement of the uniformity of self-assembled InAs quantum dots grown on InGaAs/GaAs by low-pressure metalorganic chemical vapor deposition", *Applied Physics Letters*, 85, 14, P2753-2755 (2004).

68. Walker C L, Sandall I C, Smowton P M, Mowbray D J and Liu H Y and Hopkinson M, "Improved performance of 1.3um In(Ga)As quantum-dot lasers by modifying the temperature profile of the GaAs spacer layers", IEEE Photonics Technology Letters, 18, 14, P1557-1559. (2006).

69. Wang X D, Wang S M, Wei Y Q, Sadeghi M and Larsson A, "High-quality 1.3μm GaInNAs single quantum well lasers grown by MBE", *IEEE Electronics Letters*, 40, 21, 20046557 (2004).

70. Sugawara M, Mukai K, Nakata Y, and Ishikawa H, "Effect of homogeneous broadening of optical gain on lasing spectra in self-assembled $In_xGa_{1-x}As/GaAs$ quantum dot lasers", *Physical Review B*, 61, 11, P7595-7603 (2000).

71. Smowton P M, Pearce E J, Lutti J, Matthews D R, Summers H D, Lewis G M, Blood P, Hopkinson M and Krysa A, "Carrier distribution and gain in self assembled quantum dot lasers", *Proceedings of SPIE: Novel In-Plane Semiconductor Lasers III*, 5365 (2004).

72. Bhattacharya P, Singh J, Yoon H, Zhang X K, Gutierrez-Aitken A, and Lam Y L, "Tunneling injection lasers: a new class of lasers with reduced hot carrier effects", *IEEE Journal of Quantum Electronics*, **32**, P1620-1629 (1996).

73. Fathpour S, Mi Z, and Bhattacharya P, "High-speed quantum dot lasers", Journal of Physics D: Applied Physics, 38, 2103-2111 (2005).

74. Mi Z, Bhattacharya P, and Fathpour S, "High-speed 1.3μm tunnel injection quantum-dot lasers", *Applied Physics Letters*, **86**, 153109 (2005).

75. Blood P, "Nanostructure Optoelectronics Lectures", *Undergraduate Lecture Series*, Cardiff University (2005).

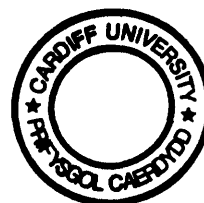

76. Smowton P M, Blood P, Mogensen P C, and Bour D P, "Role of sublinear gain-current relationship in compressive and tensile strained 630 nm GaInP lasers", *International Journal of Optoelectronics* **10**, 383-392 (1996).

77. Asryan L V, Grundmann M, Ledentsov NN, Stier O, Suris R A, Bimberg D, "Effect of excited-state transitions on the threshold characteristics of a quantum dot laser", IEEE Journal of Quantum Electronics, 37, 3, P418-425 (2001).

78. Markus A, Chen J X, Paranthoen C, Fiore A, "Simultaneous two-state lasing in quantum dot lasers", Applied Physics Letters 82, P1818-1820 (2003).

79. Viktorov E A, Mandel P, Tanguy Y, Houlihan J, Huyet G, "Electron-hole asymmetry and two-state lasing in quantum dot lasers", Applied Physics Letters 87, 053113 (2005).

80. Sandall I C, Walker C L, Smowton P M, Mowbray D J, Liu H Y and Hopkinson M, "Measurement of modal absorption, gain and recombination in p-doped and intrinsic quantum dot structures", IEE Proceedings-Optoelectronics, 153, 6, P316-320 (2006).

81. Summers H D, Rees P, "Derivation of a modified Fermi-Dirac distribution for quantum dot ensembles under non-thermal conditions", *Journal of Applied Physics*, 101, 073106 (2007).

82. Matthews D R, Summers H D, Smowton P M, Blood P, Rees P and Hopkinson M, "Dynamics of the Wetting-Layer–Quantum-Dot Interaction in InGaAs Self-Assembled Systems", *IEEE Journal of Quantum Electronics*, 41, 3, P344-350 (2005).

83. Tomizawa M, Hirano A, Ishibashi S, and Sakamoto T, "International Standardization Activities on Optical Interfaces", *Global Standardization Activities*, 1, 3, P85-89 (2003).